Engineered Transition Metal Chalcogenides for Photovoltaic, Thermoelectric, and Magnetic Applications

By

Nicholas Anton Moroz

A dissertation submitted in partial fulfillment
of the requirements for the degree of
Doctor of Philosophy
(Materials Science and Engineering)
in the University of Michigan
2017

Doctoral Committee:

Associate Professor Pierre Ferdinand Poudeu-Poudeu, Chair
Associate Professor Bart Bartlett
Assistant Professor Emmanouil Kioupakis
Professor Katsuyo Thornton

DEDICATION

To my family, big and small.

ACKNOWLEDGEMENTS

I would like to thank, first and foremost, my advisor, Prof. Ferdinand Poudeu, for his outstanding guidance, insight, and collaboration that has been undoubtedly necessary in the completion of my doctoral studies. Academically and technically Prof. Poudeu has enabled and encouraged me to delve deeply into important research, and done so with exceptional patience and understanding. My path to achieving a doctorate has been meandering, and there was a time at which I felt lost without research goals and ambitions that would lead to culmination in a thesis. It was during this time that Prof. Poudeu warmly accepted me into his group and helped me conduct fulfilling, and thematic research that would offer important contributions to the scientific community. For that, I am eternally grateful.

My sincere thanks also to Prof. Bart Bartlett, Prof. Emmanouil Kioupakis, and Prof. Katsuyo Thornton for their support, shared knowledge, and mentorship in completing my studies as my doctoral committee. Further, I thank them and their research groups for many important contributions to this work, particularly Adam Crowe, Dr. Kayla Piper, Sam Esarey, James Brancho, Charles Lhermitte, and Aaron Proctor of the Bartlett group for their help in the production of $Cu_{2-x}Se$ nanoplatelets and optical studies, and Logan Williams of the Kioupakis group for density functional theory simulation contributions. I would also like to thank Prof. Jennifer Aitken and her research group at Duquesne University for help with optical studies of materials. I also thank my original graduate studies advisor, Prof. Jyoti Mazumder, for his help in navigating this challenging course.

I am also extremely thankful for the support, camaraderie, and friendship of my lab mates within the Poudeu group, Alan Olvera, Brandon Buchanan, Chris Bauer, Joseph Casamento, Erica Chen, Gabriella Willis, Juan Lopez, and Ruiming Lu. Without your help, and ingenious contributions, this work would never have been as impactful or complete. I would also like to thank previous members of the Poudeu group who have worked with and supported me over my doctoral studies and fostered my interest in developing new materials, Prof. Honore Djieutedjeu, Dr. Pranati Sahoo, and Dr. Yuanfeng Liu.

Special thanks the Prof. Ctirad Uher and his group, specifically Alex Page, Pan Ren, and Trevor Bailey, for their outstanding collaboration on nearly every project presented in this thesis.

Special thanks also to Dr. Kai Sun and Dr. Haiping Sun of the University of Michigan Center for Materials Characterization $(MC)^2$ for training and continually helping me on various microscopes and characterization equipment. Thanks also to Justin Scanlon, Tim Chambers and Ying Qi of the Materials Science and Engineering Department at the University of Michigan for their help in characterization of many of the materials presented here as well as Keith McIntyre for his aid in the machine shop.

I've enjoyed great support in completing this milestone from many friends and colleagues outside of academia and the University of Michigan, particularly Nicholas Cucinelli, Pedro Guillen, and Dr. Benaiah Schrag, who have been integral in my success.

I would also like to thank all of my teachers and instructors over my academic career, including my first advisor Prof. David Seely (Albion College, MI). They instilled a scientific curiosity in me that I will forever appreciate.

Finally, I would like to thank my family: my fiancée Leigh, my brothers Harry and Alex, and my mom and dad. Their loving help and cheerful support has been exactly what I needed to complete these studies in a meaningful way.

TABLE OF CONTENTS

LIST OF FIGURES

LIST OF TABLES

LIST OF EQUATIONS

ABSTRACT

This work focuses on the development of ternary and quaternary chalcogenide compounds featuring transition metal cations through careful engineering of the electronic and thermal transport as well as magnetic properties by traditional solid-state doping techniques as well as novel template structure synthesis methods for improvements in thermoelectric performance, diluted magnetic semiconductors, and photovoltaic conversion. This extremely large and diverse family of materials has become centerpieces for the development of solar cells, thermoelectric generators and refrigerators, magnetic memory storage, and other impactful innovations due to their highly flexible chemical composition and defect-sensitive transport properties.

Presented here is an innovative low-temperature batch synthesis process that was developed to create hexagonal nanoplatelets of the interesting thermoelectric CuAgSe. This process utilized a room temperature ion exchange reaction to convert cubic $Cu_{2-x}Se$ hexagonal template nanoplatelets into the ternary composition by replacing a portion of the Cu^{+} ions with Ag^{+} while maintaining the morphology of the nanoplatelet. It was found that both the low temperature pseudotetragonal and the high temperature cubic forms of CuAgSe were created, which suggests that the cubic-to-cubic transformation is energetically preferential. This simple reaction process offers an energy efficient, cost-efficient, and versatile strategy to create interesting materials with lower defect density and superior thermoelectric performance.

Continuing research into copper based ternary chalcogenides for thermoelectric and photovoltaic applications, an investigation of the thermal and electronic transport of $CuAl(S_xSe_{1-}$

$_x)_2$ solid solutions was conducted. While these compounds yielded low thermal conductivity, they also exhibited low electronic conductivity. Doping with transition metals Ag, Hf, and Ti further reduced the thermal conductivity below 1 W/mK; however, most exciting was the determination that the thermal transport of the system could be modified by doping at the Al^{3+} site without affecting the electronic structure of the system, potentially leading to the use of $CuAl(S_xSe_{1-x})_2$ as a heavily doped thermoelectric material.

The effect of local carrier concentration in the high Curie temperature diluted magnetic semiconductor $FeSb_2Se_4$ was studied by isomorphic and isoelectronic substitution of In^{3+} for Sb^{3+}. Using systematic Rietveld refinement of diffraction data of $FeSb_{2-x}In_xSe_4$ solid solutions, it was determined that In^{3+} resides in the semiconducting layer of the structure for concentrations of $x \leq 0.1$, and the magnetic layer of $FeSb_2Se_4$ for $x > 0.1$. The increase in local carrier concentration was shown to have an appreciable effect on the electronic and magnetic properties of the material in a predictable manner based on the concentration of In^{3+} in each layer, which were determined to be antiferromagnetically coupled. Langevin fitting of magnetization curves quantified the relationship between In^{3+} content (increased carrier concentration) and the strength of bound magnetic polarons, an important understanding of this material that can be utilized for spintronic applications.

Lastly, two new perovskite-like selenides were developed using relatively low-pressure synthesis methods, needle-like $SrHfSe_3$ and distorted perovskite $BaHfSe_3$. Though exhibiting poor thermoelectric performance, the optical band gap of $SrHfSe_3$ was experimentally determined to be 1.05 eV, which was increased to 1.15 eV by doping of Sb^{3+} for Sr^{2+}, and 1.6 eV for $BaHfSe_3$, both in the ideal range for visible light absorption. Thus, these new materials are intriguing candidates for thin-film photovoltaic applications.

CHAPTER 1

INTRODUCTION

1.1 Motivation and outline of thesis

The discovery of new materials has always been a central driver to the advancement of global technological goals such as alternative energy sources that are renewable and emit little to no pollution and improved computing power across a spectrum of electronic applications. As a discipline, materials science engineering combines the knowledge base of chemistry and solid-matter physics with a directed, or engineered, manipulation of the structure of material systems through variation in processing to develop both new materials and improvements of known materials. This approach applied to the field of renewable energy sources has led to the advent of polycrystalline silicon solar cells, then further to the famous photovoltaic chalcogenide compounds CdTe[1-3] and Cu(In,Ga)Se_2[4-7] that have boosted thin film conversion efficiency past 20%.[8] Other renewable energy sources, such as the reclamation of waste heat and conversion to electrical power have benefited from the development of Bi_2Te_3 for use as a thermoelectric.[9-12] Similar advancements have been made in the field of magnetic data storage with the innovation of phase change memory,[13-16] and other non-volatile memory devices,[17-22] that utilize the unique physical states of chalcogenide materials such as GeSbTe in order to both improve the life and reduce the cost of the production of flash memory.[23,24] It is clear that the production and study of new materials is both necessary and complicated, and that the path to solutions that impact our daily life is not-obvious, but lies with dedicated and meticulous engineering and understanding of

complex material systems towards incremental improvement. In the spirit of that statement, the purpose of this work is to employ innovative approaches to the synthesis and characterization of complex transition metal based chalcogenide systems to offer significant technological advances in the applications of thermoelectric devices, photovoltaic devices, and spintronics.

Ternary and quaternary transition metal chalcogenide material systems have become focal points for a wide range of interesting advanced material applications in renewable energy and computational fields due to their range of physical property phenomenon and their flexibility in stoichiometry, structure, and morphology. These compounds feature anions of either sulfur, selenium, tellurium, or a mixture thereof, and cations from elemental groups III to XII, offering a large variation in physical properties with relatively straightforward substitutional means for engineering of the electronic, thermal, magnetic, and structural properties of the compound. Often, these compounds feature low-symmetry crystal systems and highly disordered structures that can be exploited for superionic conduction, tunable electronic and optical band structures, and control of phonon-carrier scattering mechanisms. Some notable examples of functional transition metal chalcogenide systems include the creation of chalcopyrite copper-based compounds $CuInSe_2$ and $Cu(In,Ga)Se_2$ that are now some of the most promising materials for low-cost photovoltaic cell production,[25,26] the well-known $Ge_2Sb_2Te_5$ solid solution as a non-volatile phase change memory material that undergoes a thermally induced reversible and rapid amorphous-to-crystalline transition,[27,28] and Na-doped $PbTe_{1-x}Se_x$ alloys which have been shown to exhibit a thermoelectric figure of merit (ZT) of ~1.8 at 850 K that is promising for large scale waste heat conversion to electrical energy.[29-34]

As the materials engineering paradigm has traditionally been schematically defined as a tetrahedral coordination of processing, structure, properties, and performance,[35,36] this thesis will

utilize novel synthesis and material processing to elucidate and analyze relationships between the crystal and morphological structure and desirable material properties necessary to boost performance. Specifically, this work entails the use of ubiquitous synthesis techniques such as solid-state diffusion reactions at high temperature, high-pressure hot pressing for densification and the promotion of metastable phases, but also newly developed techniques such as solvothermal synthesis to produce template nanostructures that can be converted to interesting materials using low-temperature reactions. These synthesis techniques target the control and engineering of the electronic, thermal, and magnetic transport properties of chalcogenide compounds in an effort to increase the performance of materials for three specific applications: bulk thermoelectric devices, ferromagnetic memory, and photovoltaic conversion devices.

To accomplish this task, the research, characterization, and analysis described here will center around four main material systems and their application, namely CuAgSe and $CuAl(S_xSe_{1-x})_2$ where x = 0 – 1 compounds for thermoelectric applications, $FeSb_{2-x}In_xSe_4$ where x = 0 – 0.25 as a magnetic semiconductor tailored for magnetic memory applications, and needlelike $Sr_{1-x}Sb_xHfSe_3$ and distorted perovskite $BaHfSe_3$ as promising photovoltaic absorber materials. We start first with an introductory discussion of the target applications and important material properties that affect performance, second, the experimental techniques employed to synthesize, process, and characterize these materials are presented, this is followed by a discussion of four research projects and some final general conclusions.

1.2 Thermoelectricity and Semiconducting Metal Chalcogenide Systems

Thermoelectricity is the direct conversion of heat to electrical energy, or vice versa, by means of either the Peltier or Seebeck effect. In the Seebeck effect, when a thermal gradient is applied to a thermoelectric material junction a voltage response is produced. For the Peltier effect,

if a voltage is applied to a thermoelectric material junction either cooling or heating is produced. While these are separate physical phenomena, the Seebeck and Peltier effect can be seen as counterparts in a closed thermoelectric circuit.[37] In practice, a thermal gradient is applied to a material, typically a semiconductor, which results in charge migration in one direction, creating a voltage gradient once at steady state. Thus, the Seebeck coefficient, also referred to as the thermopower, can be defined as the negative ratio of the voltage gradient to the temperature gradient across the material, Equation 1-1. The negative sign in the equation is a convention such that if S is positive the portion of the material at higher temperature has lower voltage, and conversely, if S is negative then the cold portion of the material is at higher voltage than the hotter side. It can then be reasoned that if the material is a p-type semiconductor, containing an excess of holes or anti-electrons as a majority of the charge carriers, and placed in a thermal gradient, the holes will migrate to the cold side of the material, whereas the electrons will migrate to the warm side, Figure 1-1. The opposite is true for an n-type semiconductor, of which the majority of charge carriers are electrons. To create a thermoelectric device, a parallel junction of n-type and p-type materials connected in series with respect to current flow, but in parallel with respect to heat follow is attached to a load resistance or source, which can then either be used to produce a thermal effect with an applied current, or a current given a thermal gradient, Figure 1-1.

Equation 1-1: $S = -\frac{\Delta V}{\Delta T}$

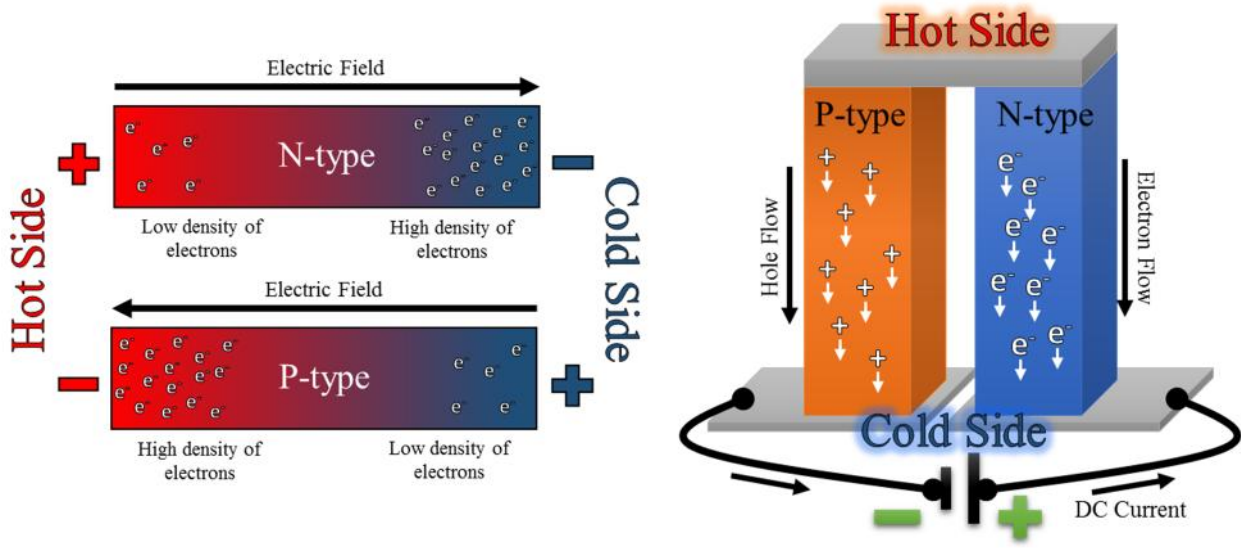

Figure 1-1: Left) Schematic of migration of charge carriers, holes (antielectrons) and electrons, in a material with an applied thermal gradient representing the Seebeck effect for both n-type (electrons as the majority charge carriers) and p-type (holes as the majority charge carriers). Right) Illustration of practice application of Seebeck effect in a thermoelectric device consisting of n-type and p-type legs.[38]

In order to produce a highly efficient thermoelectric device, it then becomes obvious that we wish to minimize the electronic resistance of the system, while maximizing the thermal resistance and the thermopower, which can be considered analogous to the thermoelectric capacitance of the system. Conventionally, we define the dimensionless figure of merit, ZT, as a measure of the thermoelectric efficiency of a material, Equation 1-2, where σ is electronic conductivity, T is the absolute temperature, and κ is the total thermal conductivity.

$$\textit{Equation 1-2: } ZT = \frac{\sigma S^2 T}{\kappa_{total}}$$

Semiconductors, therefore, provide significant advantages over metals and insulators, in that they provide low thermal conductance over wide temperature ranges, relatively high electronic conductance, and offer the ability for engineering of n-type or p-type behavior and carrier concentration through the introduction of defects,[39,40] solid-solution alloying,[41-43] or other means.[44] To further understand the challenges in designing a highly efficient thermoelectric semiconductor,

we must consider the relationships between electronic conductivity and thermopower. The electronic conductivity, the inverse of resistivity, ρ, can be defined as the carrier concentration, n, multiplied by the charge of an electron, e, and the carrier mobility, μ, Equation 1-3. As a simplification, the thermopower can also be defined as Equation 1-4, in which k_B is Boltzmann's constant, h is the Planck constant, m^* is the carrier effective mass, and n is the carrier concentration.[45] These two equations highlight the fact that one cannot simply increase the carrier concentration of a semiconductor in order to boost the thermoelectric performance of the system since the thermopower is inversely proportional to the carrier concentration, Figure 1-2. Hence, through careful means, the target in engineering semiconductors for thermoelectric application combines an optimization of the thermopower and electronic conductivity, through doping,[46-49] energy filtering,[50-55] electronic band structure engineering,[56-60] or increasing the effective mass of carriers,[56] while reducing the thermal conductivity by means of point defects,[61-63] nanostructuring,[50,51,64,65] and mesoscale features.[66,67]

Equation 1-3: $$\sigma = \frac{1}{\rho} = ne\mu$$

Equation 1-4: $$S = \frac{8\pi^2 k_B^2}{3eh^2} m^* T \left(\frac{\pi}{3n}\right)^{2/3}$$

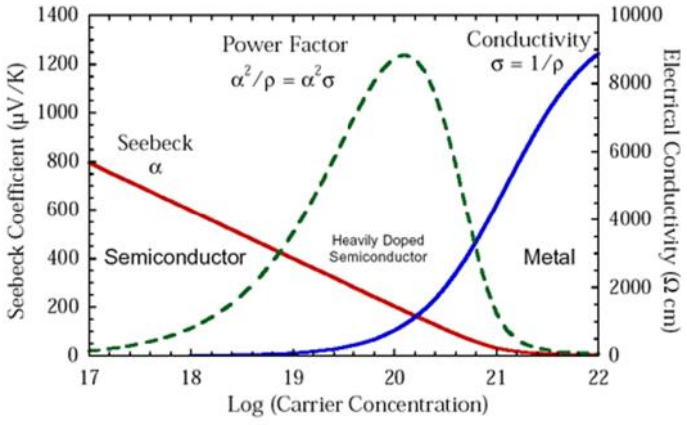

Figure 1-2: Effect of carrier concentration on Seebeck coefficient, electronic conductivity, and power factor for semiconductors, heavily doped semiconductors, and metals.[51] This highlights the strategy of carrier concentration optimization for thermoelectric performance.

Since Maria Telkes's creation of the first thermoelectric power generator based tellurides and selenides,[68] substantial research and development efforts have improved the ZT to 2.6 along the b-axis of single crystal of SnSe, the record to date.[69,70] Other interesting materials such as PbTe have been shown to achieve a ZT of 1.8 at 850 K[71] and Bi_2Se_3 with ZT between 0.8 and 1.0.[72] These binary transition metal chalcogenide systems feature high thermopower and electronic conductivity with relatively low thermal conductivity. While these materials offer significantly high performance for commercial applications, new materials and synthesis methods that are non-toxic (non-lead containing) derived from Earth-abundant elements and that offer improved control of defect concentration, crystal structure, and particle morphology are needed to enable broad adoption of thermoelectric device technology. The work presented here highlights two approaches toward the development and optimization of thermoelectric materials: the nanostructuring of CuAgSe by means of a novel low-temperature synthesis processes that effectively reduces the thermal conductivity of the system at low temperatures to improve ZT, and the development of a series of $CuAl(S_xSe_{1-x})_2$ solid solutions doped with transition metal cations in to reduce thermal conductivity and improve electronic transport.

1.3 Memory, Magnetism and Transition Metal Chalcogenide Systems

Materials that offer multiple interesting properties, such as semiconducting and ferromagnetic nature, have been central to scientific research as they offer a setting to relate these behaviors directly, gaining a better understanding of fundamental forces, which can lead to the exploitation of physical phenomena in a useful manner. Magnetic semiconductors are such materials, first developed in the 1960's in order to feature both electrical transport and magnetism in materials like EuO,[73-75] $CuCrTiS_4$,[76,77] and $CdCr_2Se_4$.[73,78-80] The general importance of these materials is that the electronic carriers in the system are affected by local magnetic moments,

resulting in a magnetic ordering that is in some ways linked to an electronic structure that can be considered a spin-coupling. The consequences of this are such that the electrons in the system can essentially be spin-oriented around magnetic centers, contributing to the ferromagnetic ordering. This interaction was first proposed and modeled by Zener in 1950 to describe the magnetic interactions between two magnetic atoms separated by a non-magnetic atom.[81,82] The Zener model proposes an electron exchange mechanism in which valence electrons are ferromagnetically coupled to a magnetic atom can hop to a nearest neighbor non-magnetic atom orbital and then to a second adjacent magnetic atom orbital, typically maintaining the original spin state, Figure 1-3. While this model was the first to link localized spins and charge carrier motion, it failed to predict ferromagnetism in higher Curie temperature, T_C, materials, and fails to predict spin interactions over long distances. Unfortunately, these early magnetic semiconductors, in some ways based on the Zener model, suffered from low T_C, typically below 100 K, which renders them ill-suited for magnetic memory devices and other spintronic technologies.

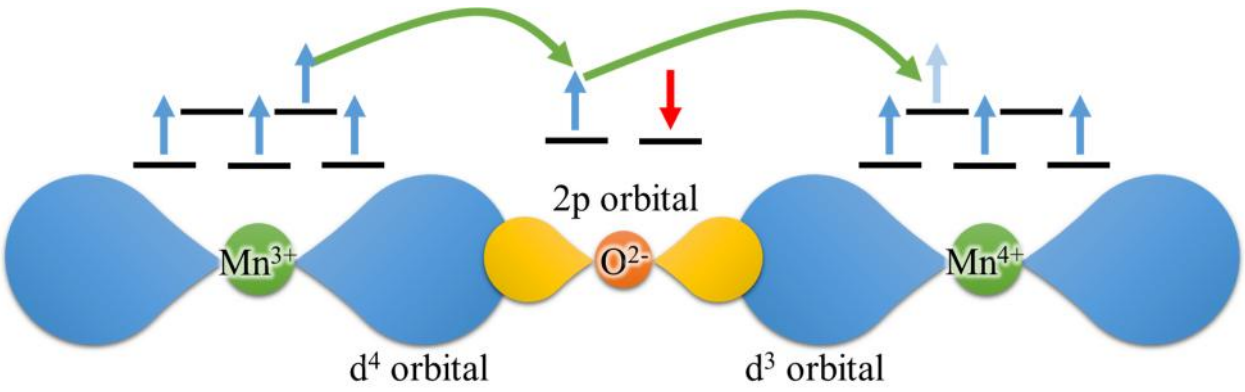

Figure 1-3: Zener's model of spin carrier hopping from magnetic atom to non-magnetic atom to magnetic atom, exemplified in hopping of electron from the d orbital of an Mn^{3+} ion to the 2p orbital of O^{2-} ion then to d orbital of the nearest neighbor Mn^{4+} ion.[83]

Further modeling of ferromagnetism in conductive materials was developed by Ruderman et al. in 1954, known as the RKKY theory (Ruderman-Kittel-Kasuya-Yosida), which describes an indirect exchange coupling between magnetic moment separated by long distances.[84] This

interaction successfully predicted the phenomenon of giant magnetoresistance (GMR)[85,86] that has led to some of the most prolific commercial applications of magnetic semiconductors such as hard disk drives and microelectromechanical systems (MEMS).[87] While the Zener model was accurate for metals, given the short interaction distance, the RKKY model can be combined with the Zener model to effectively model magnetism in semiconductors, which feature both long and short order interactions.

More recently, the development of dilute magnetic semiconductors has reignited a flurry of research into materials that couple charge carrier spin and ferromagnetism.[22,88,89] These materials are based on fundamental semiconducting materials such as ZnO,[90,91] Si,[92] and GaAs,[93,94] which are then implanted with magnetic atoms that act as magnetic centers in the overall structure. The tailoring of charge carrier concentration led to the discovery by Story et al. that the T_C of Mn-doped $Pb_{1-x}Sn_xTe$ could actually be tuned with respect to the carrier concentration.[95] These advancements coincide with one of the most recent modeling developments describing ferromagnetism, a modified Zener model created by Dietl et al., which explains ferromagnetism ins III-V and II-VI magnetic semiconductors.[96] Taking into account that ferromagnetism in semiconductors is mediated by charge carriers, Dietl et al. proposed that a high concentration of holes in a p-type dilute magnetic semiconductor could produce a material with T_C as high as 200 K, or possibly even approach room temperature.[96]

While this understanding of the interaction of charge carriers, magnetic atoms, and non-magnetic atoms, as well as quantum oscillations, could effectively model the ferromagnetism exhibited by delocalized carriers in conductive materials, it does not accurately describe magnetism due to localized carriers in insulating materials. Thus, the existence of bound magnetic polarons (BMPs) must be considered in order to fully detail magnetism in important dilute

magnetic semiconductors.[97,98] BMPs are created when charge carriers, either electrons or holes, are "localized" through spin interactions with magnetic centers, creating a high density of charge carriers that mediate the local ferromagnetism. The coupling of the charge carrier to the magnetic ion creates a quasiparticle known as a polaron. These BMPs can then ferromagnetically, and, or antiferromagnetically interact with one another, combining to form a bulk magnetic moment. It is important to note that the size, or effective radius, of the BMP is proportional to the density of polarons that are localized, such that the magnetic properties of the material system can be greatly affected by the local carrier concentration.

Ternary and quaternary transition metal chalcogenide compounds offer an intriguing pathway towards a greater understanding of magnetic interactions within dilute magnetic semiconductors, and may hold the key to the development of room temperature ferromagnetism. The highest T_C achieved to date in a dilute magnetic semiconductor is ~200 K from Mn-doped GaAs that exhibits ferromagnetism rather than paramagnetism. Still, more complex, lower crystal symmetry systems, such as $FeSb_2Se_4$,[99-101] can offer interesting environments to probe distinct interactions between charge carriers and BMPs, long distance spin coupling, and other important magnetic phenomena that could lead room temperature ferromagnetism in dilute magnetic semiconductors. There are many variants on magnetic memory commercially available today, all of which store information in magnetic domains on semiconducting materials by writing using either a strong magnet or voltage. An example of how dilute magnetic semiconductors based on chalcogenide systems can be used in spin memory is shown in Figure 1-4. The potential of room temperature ferromagnetism lies in the realization of persistent spin memory, which is a true integration of the microprocessor with read/write storage, offering new file storage architectures and vastly improved efficiency. To contribute to the understanding of interactions between

exchange coupling and BMPs in magnetic semiconductors, Chapter 4 presents a study of In-doped magnetic semiconductor $FeSb_2Se_4$ in which it is determined that In^{3+} substitution for Sb^{3+} increases local carrier concentration to strongly affect the magnetic properties of the material. This allows for tailoring of the electronic/magnetic behavior distinct from the structure of the material, useful for spintronic devices.

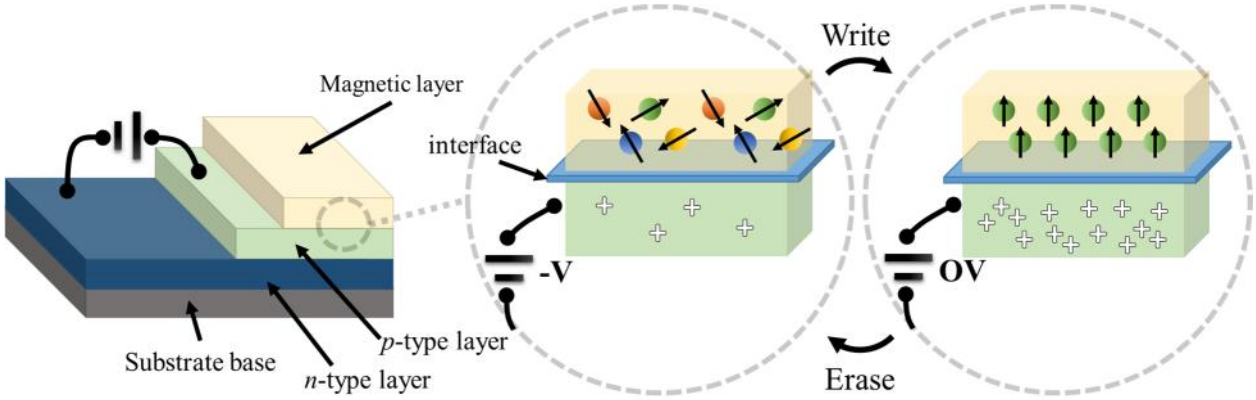

Figure 1-4: Schematic of spintronic based magnetic memory storage device using dilute magnetic semiconductors. The stack, shown on the left, consists of a p-n *junction with a magnetic layer on top. If negative voltage is applied to the junction the spins in the magnetic layer become disoriented. If the voltage is removed, the spins of the holes in the* p-*type layer magnetize the magnetic layer, which can be considered a bit. Image adapted from IEEE Spectrum.*[102]

1.4 Photovoltaic Applications of Transition Metal Chalcogenide Systems

Perhaps the most well-known application of transition metal chalcogenide compounds is as a functional material for solar cells.[103-106] Solar energy, the conversion of sunlight to electricity, now accounts for 27% of the total global energy production, and is predicted to become the world's largest source of electricity by 2050.[107] Solar energy through the use of photovoltaic materials for conversion represents 16% of the current global electricity production.[107] The need for new photovoltaic materials that are low-cost, non-toxic, and high efficiency has never been greater.

Photovoltaic solar cells combine a series of solar absorbing materials, typically in stacked thin-film form, creating junctions of layers that convert light of varying wavelengths into electrical

currents, Figure 1-5. Light passes through a transparent anode and is then absorbed by an n-type doped semiconducting layer. Electrons are excited from the carrier rich valence band by the absorbed light to the conduction band and are then funneled to the anode, while holes are excited within the p-type layer, which migrate to the cathode, creating an electrical current, Figure 1-6.

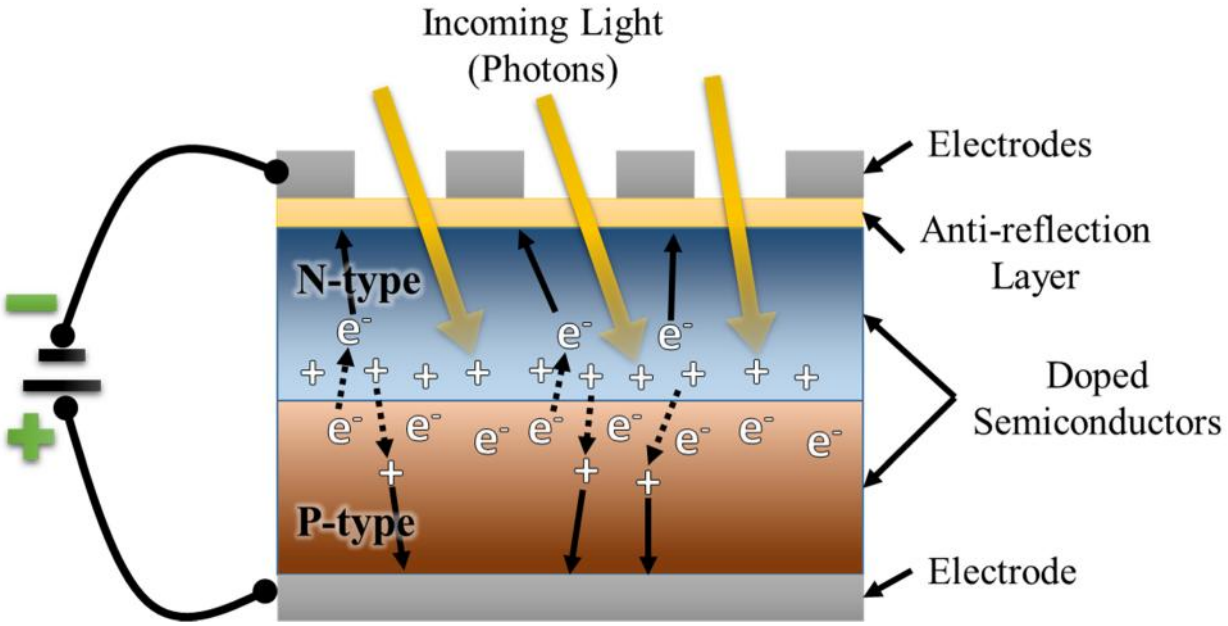

Figure 1-5: Schematic of photovoltaic solar cell.

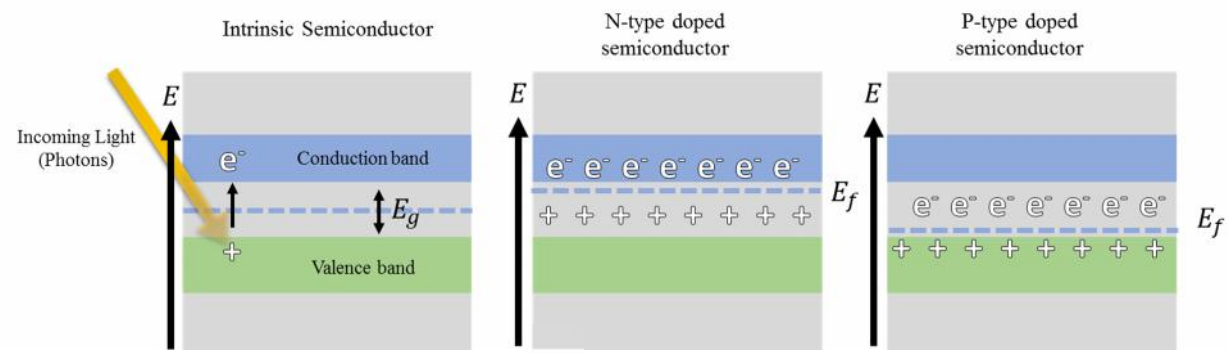

Figure 1-6: As light is absorbed by the photovoltaic materials, electrons, or holes, are excited from the valence band to the conduction band creating an electrical current in the cell. N- and p-type doping move the fermi level, E_f, towards and away from the conduction band.

Copper-based transition metal ternary chalcogenide compounds, famously $CuInSe_2$ (CISe) and $Cu(In,Ga)Se_2$ (CIGSe), were first developed for photovoltaic cells by thin-film co-deposition at Bell Labs in 1975. Since then, a series of developments in the deposition, including deposition

onto sodium containing glass and Cu-lean compositions, of CISe and CIGSe has led to an increase in direct band gap photovoltaic cell efficiency to 20%.[5] To date, this is the highest photovoltaic conversion efficiency reached by any significant commercial material. Chapter 6 discusses the development of a series of novel transition metal chalcogenides based on the ABX_3 structure, including needlelike $SrHfSe_3$ and distorted perovskite $BaHfSe_3$, which exhibit band gaps efficient at absorbing light in the visible spectrum with predicted high absorption coefficients.

1.5 Interesting Properties of Transition Metal Chalcogenide Materials

Transition metal chalcogenide compounds, comprised of cations from the d-block of the periodic table and anions such as S, Se, or Te, have been important electronic and photovoltaic compounds since the 1970s when chalcogenide glasses were developed for photocopying and switching applications.[108,109] As polycrystalline structures featuring a variety of symmetries and configurations, these materials have become centrally important semiconductors for the study of structure-property relationships leading to the design of optimized materials. Typically featuring a primarily-covalently bonded zinc blende or wurtzite structure for monochalcogenide systems, and a layered structure for dichalcogenide systems, these materials famously offer a large contrast between thermal, electronic, optical, and magnetic properties due to defect or stoichiometric sensitivity, leading to interesting unique physical properties such as extremely high ionic mobility, modulated electronic and magnetic response, an intrinsically high-defect density that provides natural doping of the materials. Each of these properties offers significant advantages when designing thermoelectric materials, dilute magnetic semiconductors, and photovoltaics.

Recently, a $Cu_{2-x}Se$ has emerged as a high-performance thermoelectric material due in part to superionic conduction of Cu^+ ions. At ~400 K $Cu_{2-x}Se$ undergoes a phase transition from tetragonal to cubic symmetry that provides a large amount of defects which actually stabilize the

compound in copper-lean stoichiometry. At high temperatures the Cu^{+} ion mobility increases dramatically, showing nearly-liquid behavior that reduces the specific heat near to the theoretical limit, Figure 1-7. Kim et al. used density functional theory simulations to show that $Cu_{2-x}Se$ features two glass-transition temperatures due to this rapid Cu^{+} motion, which further scatters phonons, but that the Se^{2-} lattice remains in place, exhibiting the "phonon-glass electron-crystal" effect that is ideal for thermoelectric performance. This effect has also been exhibited in CuAgSe.

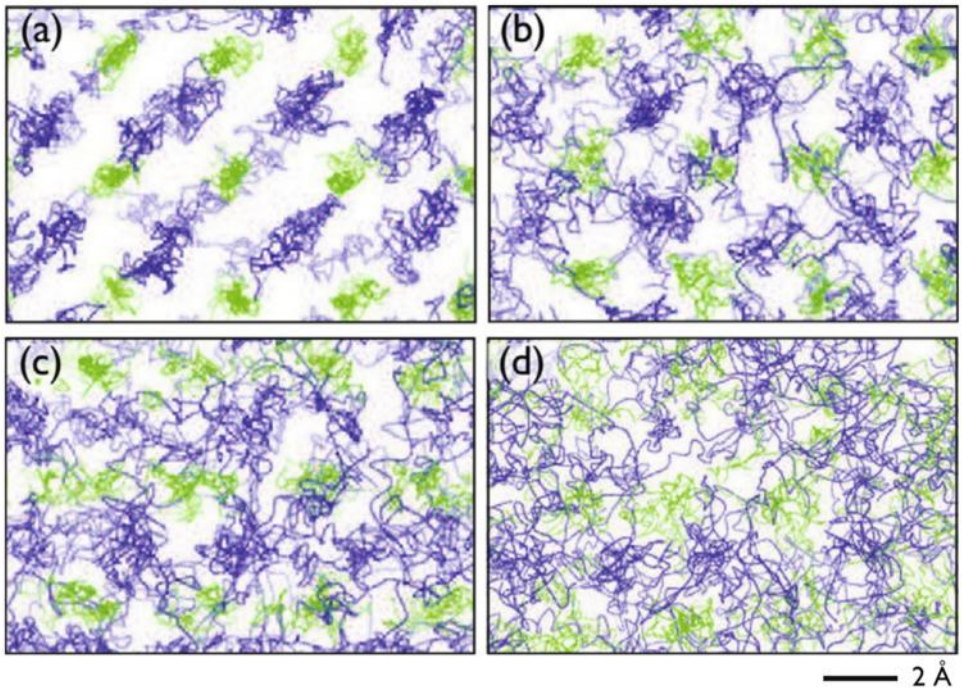

Figure 1-7: DFT simulation atomistic trajectories of Cu^{+} (blue) and Se2- ions at a) 500 K, b) 700 K, c) 900 K, and d) 1100 K showing that the motion of Cu^{+} into interstitial sites causes the "phonon-glass electron-crystal" effect. This results in a low thermal conductivity and relatively high conductivity at high temperatures.[110]

The layered structure of transition metal dichalcogenide compounds has offered the unique ability to affect the magnetic properties of dilute magnetic semiconductors by tuning the carrier concentration of the system. III-V-based materials are used ubiquitously in optoelectronics and microelectronics, such that dilute magnetic semiconductors of these materials are inherently integratable. This has led to the development of "spintronics", in which the spin of electrons are

manipulated via magnetic fields and vice versa. Some notable spintronic innovations include the spin-based magnetic-tunnel transistor, antiferromagnetic media storage, ferromagnetic tunneling diodes, and spin valves, Figure 1-8.

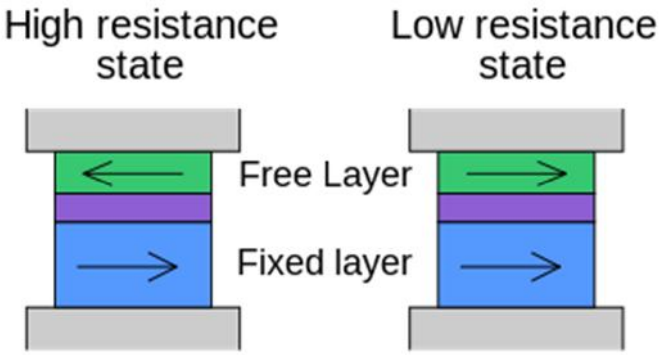

Figure 1-8: Schematic of dilute magnetic semiconductor based spin valve.[111]

The property of high intrinsic defect density of transition metal chalcogenide compounds, specifically $CuInSe_2$ and $CuGaSe_2$, has been extremely beneficial to photovoltaic applications, Figure 1-9. The absorption of photons is governed by the concentration of holes in the active material, which accept electrons. The inherent Cu-deficiency of $CuInSe_2$, $CuGaSe_2$, and other copper-based chalcogenides provide some of the highest absorption coefficients of any known materials, and thus have become centerpieces of high-efficiency polycrystalline solar cells. This high defect density is also integral in the doping of these materials to create heterojunctions that boost the solar cell efficiency.

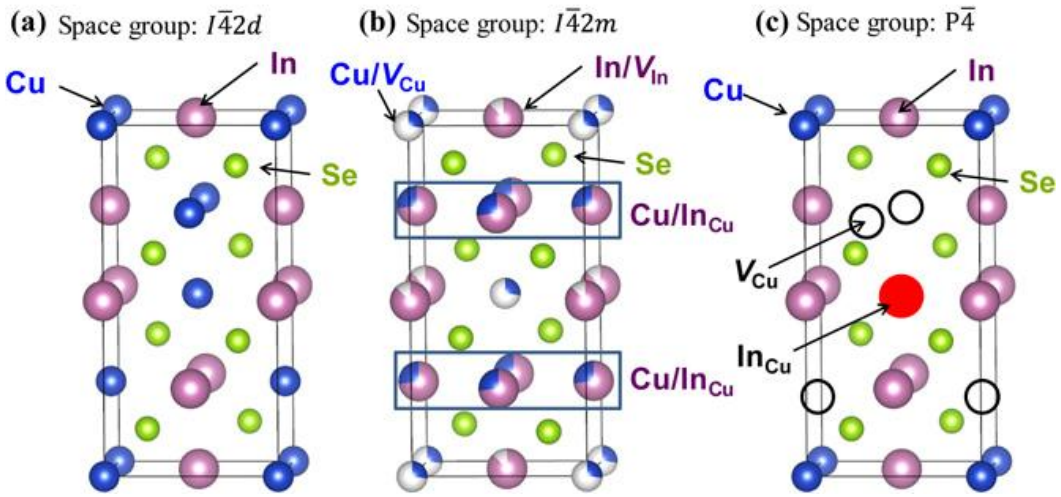

Figure 1-9: a) Perfect chalcopyrite crystal $CuInSe_2$ and Cu-lean b) $CuIn_3Se_5$ and c) $CuIn_5Se_8$ structures showing possible defects. [112]

CHAPTER 2

EXPERIMENTAL TECHNIQUES

2.1 Synthesis

A variety of synthesis techniques were used to produce a wide range of transition metal chalcogenide compounds with variations in stoichiometry, chemical dopants, particle morphology, and crystal structure.

2.1.1 Subcritical solvothermal synthesis

In this synthesis technique, used in this work to produce a series of $Cu_{2-x}Se$ nanoplatelets, chemical reactants, such as salts or reducing agents and water, are weighed or measured and placed into a Teflon liner with a Teflon lid, Figure 2-1. The liner is then secured in a stainless steel bomb with a threaded lid. The bomb is then placed into a furnace and ramped to a desired temperature, held for a prescribed period of time, then cooled to room temperature. The contents are then carefully removed from the Teflon liner and centrifuged. The liquid is then carefully removed, leaving the solid products in the centrifuge tube, which are washed with solvents such as ethanol and centrifuged further to remove all unreacted materials before drying in an oven.

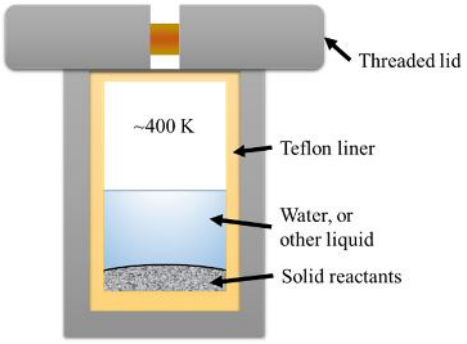

Figure 2-1: Schematic of solvothermal synthesis technique.

2.1.2 Ion Exchange Reaction

Ion exchange reactions, in which ions are exchanged between an electrolyte solution and a solid compound, were used to convert nanoplatelets of binary chalcogenide compounds into ternary compounds. Salt reactants, such as nitrates and acetates, were weighed and added to a beaker of ethanol and placed in an ultrasonic bath until dissolving completely. Solid reactants that were to exchange cations with the solute are then added to the beaker and sonicated for 1 hr. The contents were then centrifuged and washed.

2.1.3 Mechanical alloying (ball-milling)

High-energy mechanical alloying (high-energy ball milling) was used to produce fine powders of chalcogenide compounds starting from elemental powders, chunk, or granules. This process has often been used to reduce the particle size of compounds, effectively increasing the grain boundary density to reduce the thermal conductivity of systems for thermoelectric applications. This synthesis method also produces a high local pressure as the ball-bearing slam into one another at high force, which can simulate a local high-pressure synthesis necessary for the production of some high symmetry materials such as distorted perovskites. Stoichiometric amounts of constituent elements were added to hardened stainless steel jars with hardened stainless

steel ball bearings within a glovebox in an argon atmosphere. The weight ratio of balls to reactants was 10:2.5. The jars were then sealed in the glove box and transferred to a SPEX 8000D ball-mill. The jars were then shaken for the prescribed period of time. Once finished, the products of the reaction would be removed from the steel jars within the glovebox.

2.1.4 Solid state synthesis

Solid state synthesis of bulk powders of chalcogenide compounds were produced by annealing reactants in an evacuated fused quartz silica tube at high temperatures. Elemental powders, chunk, or granules were weighed out in stoichiometric amounts and added to either a bare, or carbon coated silica tube or a graphite crucible, which was then added to the tube in a glove box under an argon atmosphere. The tubes were evacuated and sealed with residual atmosphere of less than 10^{-3} Torr. The tubes were then placed in mullite sheaths with insulating ends and placed in a high temperature furnace. The reactants were then heated with a programmed heating profile and when finished, removed from the silica tube within the glove box. The contents were then dissected or ground with mortar and pestle into fine powders.

2.1.5 Single crystal growth by chemical vapor mass transport

In order to characterize with a high degree of certainty the structure and stoichiometry of new materials, single crystals were grown in fused silica tubes by annealing the synthesized powders at high temperatures for extended period of time. Approximately 0.25 g of sample material, either as a fine powder or cold pressed pellet, was added to a silica tube with dimensions 4 cm diameter and 20 cm long, and then sealed with residual atmosphere of 10^{-4} torr. The tube was then placed in a mullite insulating sheath with insulating ends and installed in a high temperature furnace at ~30° inclination with the material at the low end. The tube was then heated to high

temperature and annealed near the melting point for up to 10 days, then cooled to room temperature. The products were then gently harvested from the tube, including the tube walls. Single crystals of the desired compounds were then harvested on glass needles and characterized using single crystal X-ray diffraction techniques.

2.2 Densification

Densification of the synthesized materials was used to create high density (target >92% of theoretical density of material) pellets, which could then be polished with metallographic paper and utilized for measurement transport properties (thermal conductivity or electrical conductivity).

2.2.1 High-pressure hot pressing

Consolidation of fine powders of the synthesized materials through simultaneous application of moderate pressure and temperature was performed throughout this research in order to produce highly dense and homogenous samples for transport measurements, but also to complete reactions that require high temperature and pressure. Approximately 1.25 – 1.5 g of finely ground powder reactants were added to a graphite die with inner diameter of 10 mm. Graphite anvils were installed in the die and then the die was placed inside an Astro Industries HP4560-20 hot press. The chamber was then sealed and evacuated to ~10^{-2} torr, and then filled with flowing argon at ~20 ml/min. Pressure of up to 100 MPa was then uniaxially applied to the graphite anvils while the chamber was heated to a prescribed temperature using a cylindrical graphite heating element in close proximity to the graphite die. Once complete, the die was cooled to room temperature, removed from the hot press, and the processed pellet of material was extracted from the graphite die.

2.2.2 Spark plasma sintering

As a variant of hot pressing under moderate temperature, spark plasma sintering process involve application of mechanical pressure and high temperature by means of a pulsed high DC current to rapidly create dense pellets of material. While the uniaxial hot pressing typically requires hours of processing at high temperature, spark plasma sintering can be completed in a matter of minutes due to the speed at which the graphite elements can achieve high temperature, in excess of 1300 K. Similarly to hot pressing, approximately 1.25 – 1.5 g of finely ground powder reactants were added to graphite dies with inner diameters of 12.5 mm. Graphite anvils were installed and the die was placed between the platens in a FCT Systeme GmbH H-HP D 25-FL. The chamber was then evacuated to 10^{-3} torr, and uniaxial pressure of 55 MPa was applied to the anvils. The graphite die was then quickly heated to a target temperature, dwelled, and then cooled to room temperature in a controlled manner. The dense pellet of the material is then carefully extracted from the graphite die.

2.2.3 Determination of pellet density

Two methods were used to determine the experimental density of the pelletized materials. First, the geometric density, ρ_{geo}, was calculated by dividing the mass of the pellet by the volume of the pellet by measuring the thickness and diameter using digital calipers. The second method utilized pycnometry to measure the volume of the pellet using a He gas Quantachrome Micro Ultrapyc 1200e pycnometer. Using this volume and the mass of the pellet, the density, ρ_{pyc}, was calculated. These densities were then used to determine the percent of the calculated theoretical density following Equation 2-1.

$$\textit{Equation 2-1: } \%\ of\ theoretical\ density = \frac{\left(\frac{\rho_{geo}+\rho_{pyc}}{2} - \rho_{theo}\right)}{\rho_{theo}} \times 100$$

2.3 Characterization

2.3.1 Powder X-ray diffraction

Powder X-ray diffraction (PXRD) techniques were extensively used to characterize phase identification and fraction, the presence of impurity phases, crystal structure, atomic distribution, and other important features of the synthesized materials. PXRD diffractograms of each synthesized product were produced by mounting either powder or densified samples on aluminum or glass slides and then installed into an X-ray diffractometer. PXRD data were collected in atmosphere using a graphite monochromated Cu-Kα (λ = 1.54056 Å) on a Rigaku Miniflex 600 operating at 40 kV and 15 mA and a Rigaku Ultima with rotating arm anode operating at 40 kV and 100 mA.

2.3.2 Rietveld refinement

Rietveld refinement is a technique utilized to elucidate important structural, chemical, and crystallographic information from powder diffraction patterns. This technique relies on the creation of a simulated diffraction pattern, and then proceeds to minimize, or refine, the difference in intensity, peak location, and general profile between the simulated pattern and the experimentally generated pattern. Rietveld refinement was performed on the diffraction patterns from the pellet samples using FullProf software package[113] in order to determine the lattice constants, unit cell volume and the distribution of atoms in the structure.

2.3.3 Single crystal X-ray diffraction

Single crystals of targeted materials were harvested from annealed samples and examined by X-ray diffraction using a STOE IPDS-2T di ractometer using graphite-monochromated Mo

Kα radiation (λ = 0.71073 Å) at 50 kV and 40 mA. The crystal structure was then refined by full-matrix least-squares techniques using the SHELLX package.[114]

2.3.4 Wavelength-Dispersive X-ray fluorescence

Wavelength-dispersive X-ray fluorescence (WDXRF) is a characterization technique used to create an elemental analysis of sample by the emission of characteristic "secondary" X-rays that are excited from a material through the bombardment by X-ray radiation. Powder or pelletized samples were loaded into plastic boats with Prolene film bottoms. Samples were characterized with a Rigaku Supermini using radiation from a Pd source at 50 kV and 4 mA to determine the concentration of each constituent element and the overall chemical composition.

2.3.5 Differential scanning calorimetry

Differential scanning calorimetry (DSC) was performed using a Netzsch DSC404 F1, by placing approximately 30 mg of powder material in a quartz tube sealed under a residual pressure of 10^{-4} Torr. A sealed empty quartz tube was used as a reference. Both tubes were placed in the DSC, and the measurement was performed under flowing nitrogen gas from room temperature to temperatures up to 1523 K in order to determine phase purity and to identify thermal events associated with phase changes such as melting and crystallization of the compounds.

2.3.6 X-ray photoelectron spectroscopy

X-ray photoelectron spectroscopy (XPS) was used to assess the oxidation states and bonding of various atoms in samples. Powder, pelletized, or cold pressed 3mm pellets of samples of each composition. XPS spectra were collected for each sample using a Kratos Axis Ultra XPS equipped with a monochromatic Al source (15 kV, 10 mA). Wide scans (surveys) were acquired

using analyzer pass energy of 160 at 1 eV steps. Selected regions were then scanned using a pass energy of 20 at 0.02 eV steps for high resolution determination of bonding and oxidation state. Specimens were loaded into the transfer chamber and allowed to evacuate for a 12 hr. period reaching less than 5×10^{-7} Torr. The analysis chamber was kept at approximately 10^{-9} Torr during measurement. Post processing analysis was performed using Casa XPS.

2.3.7 Thermal transport measurements

Thermal diffusivity and heat capacity (C_p) data for each pelletized sample was measured using the laserflash method in a Linseis LFA 1000. This technique indirectly calculates thermal conductivity of each sample by direct measurements of the thermal diffusivity of the material. A laser pulse of energy heats the sample from one side as a thermal detector placed on the other side of the pellet records the thermal response. The thermal diffusivity can then be approximated using the one-dimensional adiabatic formulation shown in Equation 2-2, where d is the thickness of the sample, $t_{1/2}$ is the time to the half maximum of the thermal response, and α is the thermal diffusivity. The total thermal conductivity, κ, can then be calculated as the diffusivity multiplied by the density and heat capacity of the sample, Equation 2-3.

$$\textit{Equation 2-2: } \alpha = 0.1388 \times \frac{d^2}{t_{1/2}}$$

$$\textit{Equation 2-3: } \kappa = \alpha \rho C_p$$

Pellets were first cleaned of all graphite from hot pressing or spark plasma sintering by polishing with metallographic paper in the following order: 250 grit, 400 grit, 600 grit, 800 grit, 1000 grit, and finally 1200 grit. Pellets were cleaned with acetone and lightly coated with graphite spray, then thermal diffusivity was measured from 300 K to 723 K under flowing N_2 gas (>30

mL/min). The data collected was compared with a reference Pyroceram 9606 sample, and the accuracy of the data was determined to be within 2%, with machine precision of ±4%.

2.3.8 Electronic Transport Measurements

A series of instruments were used to determine the electronic transport properties of synthesized and densified samples.

Room-temperature to high temperature measurements of the thermopower and electrical resistivity of samples were characterized in an ULVAC-RIKO ZEM-3. Prismatic bars of each composition were polished to a mirror finish and mounted between the 4-point probe arms of the ZEM-3. The thermopower and electrical resistivity of each sample was measured simultaneously from room temperature to high temperature under a low pressure of He. The instrument precision on the electrical resistivity and Seebeck coefficient data is ±4%.

Low-temperature transport property measurements were carried out over the temperature range of 90–300 K. The thermopower and electrical conductivity were measured on samples of dimensions 2 x 3 x 6 mm under pressures below 10^{-6} torr in a custom built cryostat. The thermopower was measured using a longitudinal steady-state technique. Hot and cold side temperatures were measured with copper-constant (Type-T) thermocouples.

Hall-effect measurements of densified samples utilized and AC 4-probe setup in a Quantum Design Physical Properties Measurement System (PPMS) under a magnetic field of +/- 1 Tesla and using an excitation current of 0.1 mA in attempts to characterize the samples.

2.3.9 Magnetic properties measurements

Magnetic data were collected using a Quantum Design MPMS-CL SQUID magnetometer. DC magnetic susceptibility under field cooled (FC) and zero field cooled (ZFC) conditions were measured from a powder sample of selected $FeSb_{2-x}In_xSe_4$ compositions over a temperature range of 2 K – 300 K with an applied field of 100 Oe. Isothermal magnetization characteristics of each sample were measured at temperatures from 2 K – 300 K in DC magnetic fields from 0 – 20 kOe.

2.3.10 Scanning electron Microscopy

Samples were characterized with in a Phillips XL-30 scanning electron microscope (SEM) equipped with electron dispersive spectroscopy (EDS) analysis equipment (EDAX). Powder or densified samples were cleaned with acetone and mounted on carbon tape on an aluminum sample holder then mounted in the SEM. Microstructural and elemental analysis was conducted.

2.3.11 Transmission electron and scanning transmission electron microscopy

Transmission electron microscopy (TEM) and scanning transmission electron microscopy (STEM) equipped with EDS were used to characterize and analyze the structure and chemical distribution of constituent elements of materials at the micron scale and smaller.

CHAPTER 3

RAPID DIRECT CONVERSION OF $Cu_{2-X}Se$ TO CuAgSe NANOPLATELETS VIA ION EXCHANGE REACTIONS AT ROOM TEMPERATURE

3.1 Introduction

Binary and multinary metal selenides have become important semiconductors for thermoelectric and photovoltaic applications. Much attention has been directed towards copper selenide compounds due to the large variety of copper selenide polymorphs that exists either naturally or synthetically.[115-122] In particular, the cubic phases of copper-lean, $CuSe_2$, and copper-rich, $Cu_{2-x}Se$, are of interest for use as template lattice structures for the formation of desirable ternary and quaternary compounds. Utilizing the room temperature metastable cubic structures of these phases as template structure can reduce the energy necessary to form compounds with complex chemical compositions while maintaining the high crystal symmetry and low defect densities, critical for photovoltaic and thermoelectric applications. Further, the stability of the selenium anionic sublattice can enables the creation of new materials that cannot be synthesized by conventional high temperature solid-state reactions.

CuAgSe was first synthesized by Miyatani et al. in 1973 and was shown to exist in two polymorphs: a low temperature β-phase that features a pseudotetragonal, or orthorhombic, structure (space group *P4/nmm*, #129), and a high temperature superionic α-phase that exhibits a

cubic structure (space group $Fm\bar{3}m$, #225).[119] The pseudotetragonal CuAgSe phase consists of alternating layers of Ag and CuSe. This structure favors high mobility of Ag^+ ions. Transition to the high temperature α-phase occurs at 523 K, and forms a very similar structure to superionic cubic Cu_2Se. The cubic phase consists of Ag^+ and Cu^+ cations randomly distributed at tetrahedral sites of the face centered cubic (FCC) unit cell of Se atoms. The transformation to this superionic phase of CuAgSe results in a dramatic drop in thermal conductivity, which is due to an increased disorder from random occupation of either Ag^+ or Cu^+ cations at atomic positions in the tetragonal structure.[123,124] The thermoelectric properties of CuAgSe have not been extensively studied; however, the superionic nature of the α-phase coupled with the semimetal nature of the compound yields a great deal of interest due to low thermal conductivity and low electrical resistivity at higher temperatures. Nanostructuring of this material should dramatically increase the figure of merit at high temperatures through increased phonon scattering, and quantum confinement of carriers.

In this work, we exploit the metastability at room temperature of the cubic $Cu_{2-x}Se$ lattice to progressively replace the highly mobile Cu^+ cations by Ag^+ ions to form the ternary CuAgSe phase while maintaining the cubic structure as well as the nanoplatelet morphology. Two-dimensional (2D) morphology has been shown to increase the performance of thermoelectric materials by increasing the Seebeck coefficient through quantum confinement, as well as decreasing the thermal conductivity of the layered structure through phonon scattering at platelet boundaries.[125,126] A two-step batch process consisting of the solvothermal synthesis of the $Cu_{2-x}Se$ template material and a subsequent transformation by an ion exchange reaction appears to be an efficient and economic means to create nanoplatelets (NPs) of copper selenide-based ternary and quaternary compounds.

3.2 Production of $Cu_{2-x}Se$ nanoplatelets and the conversion to CuAgSe nanoplatelets

Nanoplatelets of copper selenide, $Cu_{2-x}Se$, were formed using a solvothermal method first described by D. Chen et al.[127] Copper acetate (98%, Sigma Aldrich) and sodium selenite (99%, Sigma Aldrich) were added to 0.2 g of sodium hydroxide (≥97%, Sigma Aldrich), 10 ml of ethylene glycol (Sigma Aldrich), and 20 ml of distilled water in Teflon liners. Stoichiometric ratios of copper acetate to sodium selenite reflecting the Cu_2Se and $CuSe_2$ products were used in the mixture: 0.18 g of copper acetate and 0.35 g of sodium selenite for Cu_2Se, and 0.09 g of copper acetate and 0.035 g of sodium selenite for $CuSe_2$. The mixture was stirred in the Teflon liners for 30 minutes and filled to 75% of the volume of each liner. 2 ml of hydrazine hydrate (80%) (Sigma Aldrich) was added to the mixture and stirred for an additional 15 minutes, turning the mixture black and precipitating the solids. The Teflon liners were then placed in stainless steel bombs and heated in a furnace at 413 K for 12 hours with a ramp up rate of 10 K/min. The bombs were then cooled at an approximate rate of 25 K/hr. The contents of the Teflon liners were then centrifuged at 3,000 RPM for 5 minutes and washed with ethanol. The contents were washed a minimum of three repetitions and then dried in a dying oven at 333 K.

CuAgSe nanoplatelets were formed by partial replacement of copper cations in $Cu_{2-x}Se$ nanoplatelets through an ion exchange reaction similar to the technique utilized by C. Nethravathi et al.[128] Silver nitrate (Sigma Aldrich) were added to ethanol in a glass vial and sonicated for up to 1 hour for complete dissolution. Dried copper selenide nanoplatelets were then added to the $AgNO_3$ solution and sonicated for 1 hour at room temperature. The blue solution containing Cu^+ was decanted and the remaining nanoparticles were washed several times using ethanol. The

product is then dried in a drying oven at 333 K until all of the ethanol has evaporated. The converted CuAgSe nanoplatelets were then collected in glass vials for further characterization.

Dense pellets of the mixed-polymorph CuAgSe material were produced by placing ~1 g of material in a graphite die with a diameter of 10 mm. The die was then placed in a GT Advanced Technologies vacuum uniaxial hot press. Pellets were pressed at 100 MPa under vacuum at three temperature histories: 1) at 423 K for 1 hour with a ramp up and down rate of 348 K/min, 2) at 723 K for 1 hour with a ramp up and down rate of 225 K/min, and 3) at 723 K for 2 hour with a ramp up and down rate of 225 K/min. The nanoplatelets for the third pellet were annealed at 723 K for 1 hour prior to pressing.

Differential scanning calorimetry (DSC) was performed to determine phase purity and to identify thermal events that indicate phase changes. Scanning electron microscopy (SEM) using a Phillips XL-30 field emission gun was utilized to determine nanoplatelet morphology. Samples of nanoplatelets in ethanol were drop cast onto carbon tape for SEM characterization. Transmission electron microscopy (TEM, JEOL 2010F and JEOL 3100) and scanning transmission electron microscopy (STEM, JEOL 2100) were used to determine platelet lattice orientation and sub-micron features of materials. Both SEM, STEM, and TEM were equipped with EDAX electron dispersive spectroscopy (EDS) systems that were used for elemental mapping on the micron and nanometer scales. The Seebeck coefficient was measured from room temperature to 773 K under a low pressure He atmosphere using a commercial ZEM-3 system from ULVAC-RIKO. The thermal conductivity was calculated from the thermal diffusivity data measured by the laser flash method (LINSEIS LFA 1000) from 300 K to 773 K under flowing N_2 gas (>30 mL/min).

3.3 Results and Discussion

In an attempt to produce copper selenide NPs of both $CuSe_2$ and Cu_2Se compositions, the copper/selenium ratio in the solvothermal reactants were varied with a 1:2 and 1:1 molar ratio (Figure 3-1).[129] The 1:1 molar ratio yielded a mixture of orthorhombic and cubic $Cu_{2-x}Se_x$, while the selenium rich mixture produced pure cubic phase $Cu_{2-x}Se$. Further attempts to synthesize $CuSe_2$ NPs by using larger excess of Se were unsuccessful under this experimental condition. Possible reaction pathways determined by D. Chen et al. indicate that Cu_3Se_2 decomposes into $Cu_{2-x}Se$ and excess Se, such that there is no further reaction between $Cu_{2-x}Se$ and Se in order to produce either CuSe or $CuSe_2$, Figure 3-2.[127] Rietveld refinement using FullProf software was performed on XRD pattern of the sample with 1:2 Cu/Se ratio (pure cubic phase). The refinement yielded excellent fitting parameters (Rf = 10.44 and χ^2 = 3.52) with a lattice parameter a = 5.6332(2) Å and a stoichiometry of $Cu_{1.8}Se$.

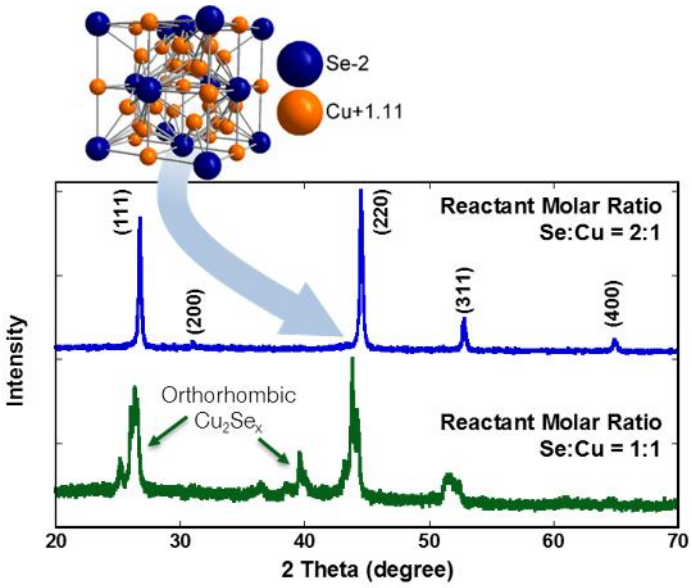

Figure 3-1: XRD patterns $Cu_{2-x}Se$ NPs template obtained from solvothermal reaction. Both a molar ratio of Cu:Se of 1:2 and 1:1 of the reactants yielded $Cu_{2-x}Se$ NPs, with the 1:2 ratio purely of the cubic phase. $Cu_{2-x}Se$ structure shown in inset.

$$Cu^{2+} + 2OH^- \rightarrow CuO + H_2O \quad \text{Step 1}$$

$$4CuO + N_2H_4 \rightarrow 2Cu_2O + N_2 + 2H_2O \quad \text{Step 2}$$

$$SeO_3^{2-} + N_2H_4 \rightarrow Se + N_2 + 2OH^- + H_2O \quad \text{Step 3}$$

$$3Se + 6OH^- \rightarrow 2Se^{2-} + SeO_3^{2-} + 3H_2O \quad \text{Step 4}$$

$$Cu_2O + CuO + 2Se^{2-} + 2H_2O \rightarrow Cu_3Se_2 + 4OH^- \quad \text{Step 5}$$

$$(1-x)Cu_2O + xCuO + Se^{2-} + H_2O \rightarrow Cu_{2-x}Se + 2OH^- \quad \text{Step 6}$$

$$(2-x)Cu_3Se_2 \rightarrow 3Cu_{2-x}Se + (1-2x)Se \quad \text{Step 7}$$

Figure 3-2: Reaction pathways determined by D. Chen et al. for production of $Cu_{2-x}Se$ nanoplatelets.[127]

SEM secondary electron imaging revealed that the template material consists of NPs with widely varying size, from 500 nm to 3 µm in diameter, and from 50 – 91 nm in thickness (Figure 3-3a) with hexagonal shape. Transmission electron microscopy (TEM) studies showed that these platelets are indeed crystalline (Figure 3-3b). Selected area electron diffraction (SAED) revealed the [111] direction normal to the planar surface of a single $Cu_{2-x}Se$ NP. Scanning transmission electron microscopy (STEM) imaging indicated that the surface of the NPs is porous.

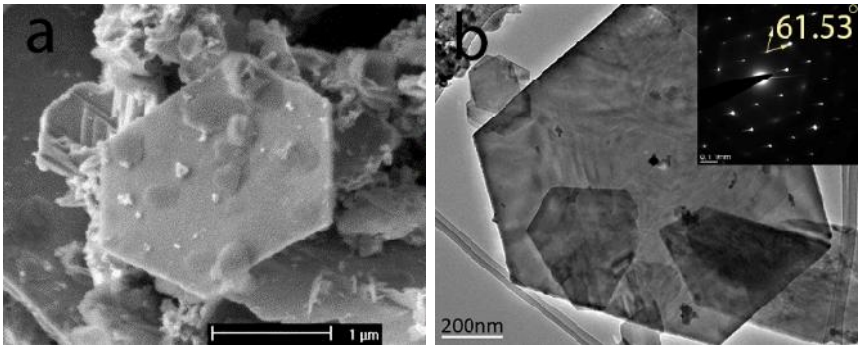

Figure 3-3: a) Secondary emission SEM image of $Cu_{2-x}Se$ NP base material showing hexagonal platelet formation with thickness of 50-91 nm and diameter of 500 nm-3 µm. b) TEM image and SAED indicating [111] orientation of NP surface.

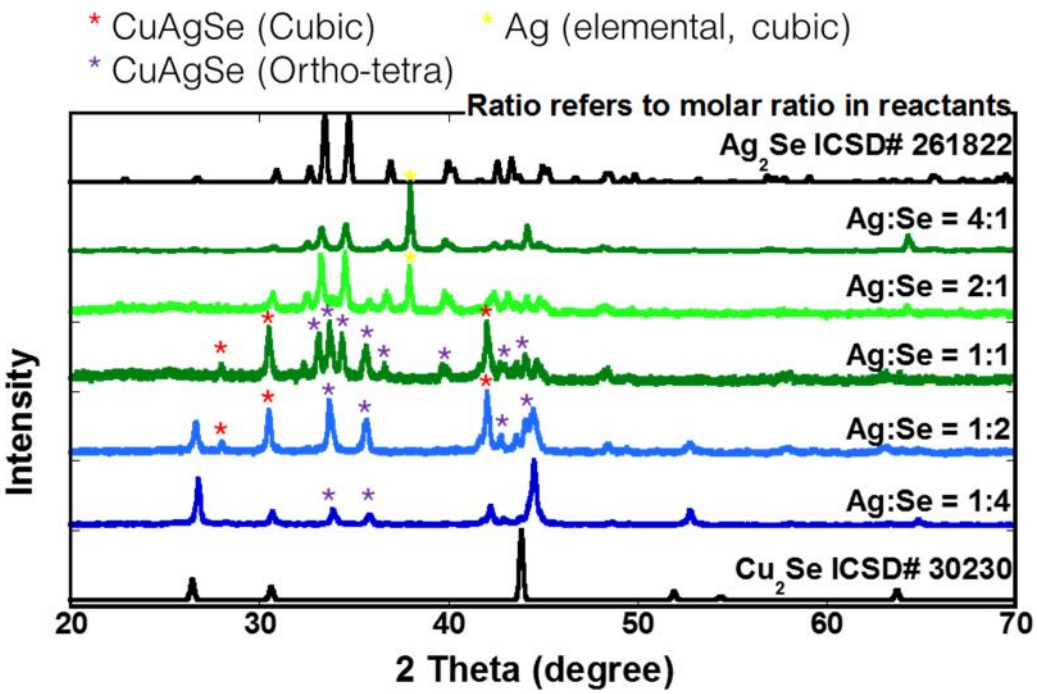

Figure 3-4: XRD patterns of ion exchange reaction products with varying molar ratios of silver to selenium in the reactants.

It is suggested that the porosity of these platelets is due to fast planar growth, which can be controlled by varying the NaOH concentration in the reactants.[130] The hexagonal shape of the nanoplatelets is consistent with the growth normal to the [111] direction of a cubic lattice that is obvious when viewing a supercell of cubic $Cu_{2-x}Se$, Figure 3-5. This means that the shape of the platelet is specific to the cubic crystal lattice.

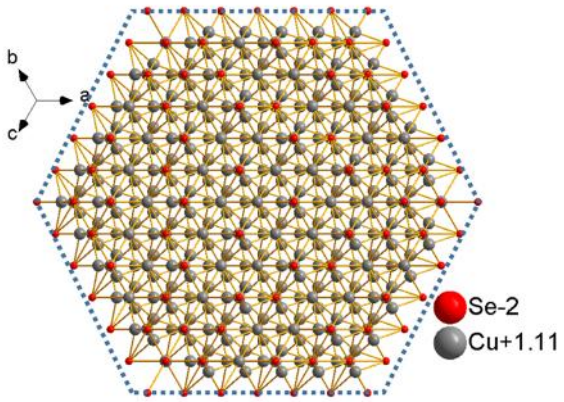

Figure 3-5: Supercell of cubic $Cu_{2-x}Se$ viewed from [111] indicating hexagonal shape for nanoplatelet grown in same orientation.

CuAgSe NPs were created via ion exchange reactions in ethanol at 300 K involving silver cations (Ag^+) and the synthesized $Cu_{2-x}Se$ NPs. The molar ratio of Ag^+ cations to Se^{2-} anions in the starting mixture was systematically varied to achieve a single phase CuAgSe product. The Ag:Se molar ratio was initially varied from 1:4 to 4:1, and the products were analyzed with powder XRD (Figure 3-4). As predicted, increasing silver content in the ion exchange reaction increased the fraction $Cu_{2-x-y}Ag_ySe$ phases formed and the amount of copper cations (Cu^+) that were displaced. This is also indicated by the intensifying blue hue of the ethanol mixture (Figure 3-6). At a ratio of 1:4, the tetragonal and cubic phases of CuAgSe are formed, leaving a substantial portion of the template $Cu_{2-x}Se$ NPs. At a ratio of 1:1, the undesirable tetragonal Ag_2Se phase is present, and at a ratio of 4:1, the entire product is a mixture of Ag_2Se and metallic Ag. It is therefore evident that at a molar ratio of four times the Ag^+ to Se^{2-} content in the reactants, all of the copper is replaced by silver cations. This result is contrary to work conducted by Lesnyak et al., which reports that a much larger excess, 50-100:1, of replacement cations is needed to fully transform the anionic template material.[131]

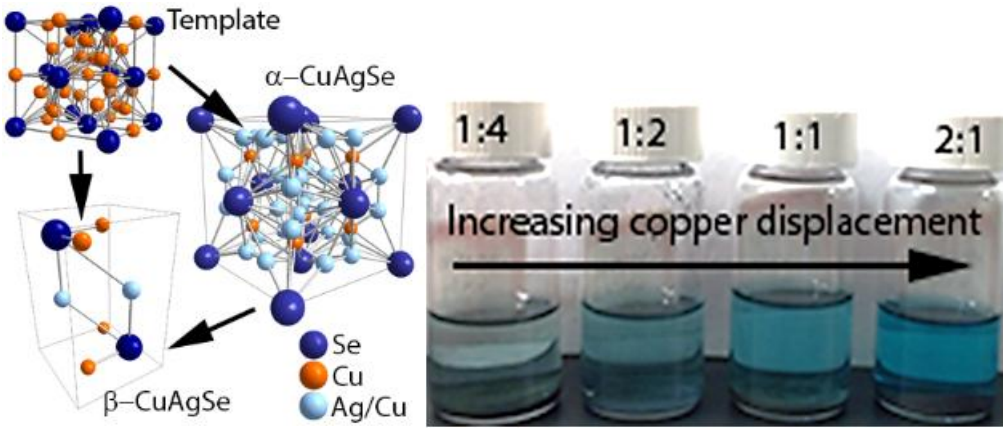

Figure 3-6: Increasing silver content in the ion exchange reaction displaces more copper cations (Cu^+) as indicated by the blue hue of the ethanol mixture. Ag:Se ratio is shown on each vial. The large amount of β-CuAgSe formed is likely due to α-CuAgSe relaxing to the β phase after synthesis.

The ion exchange reaction was then optimized by varying the Ag:Se reactant ratio from 0.58 to 0.83 to achieve a pure CuAgSe product. XRD patterns from these products (Figure 3-7) indicate that a Ag:Se ratio of 0.67 to 0.75 yields a mixture of cubic and tetragonal CuAgSe with virtually no trace of the template material ($Cu_{2-x}Se$) or the undesirable material (Ag_2Se or metallic Ag). DSC measurements of the samples formed with Ag:Se ratios from 0.58 – 0.83 show endothermic events at 473 K and 523 K (Figure 3-8). These peaks are associated with the phase transition from β-CuAgSe (tetragonal) to α-CuAgSe (superionic) cubic phase. However, only the transition at 523 K was reported in bulk CuAgSe sample.[119,132,133] Although, the nanosizing of the CuAgSe platelets can have the effect of reducing the β to α phase transition, the mechanism by which particle size reduction alters solid-solid structural phase transitions is currently not well-understood.[134]

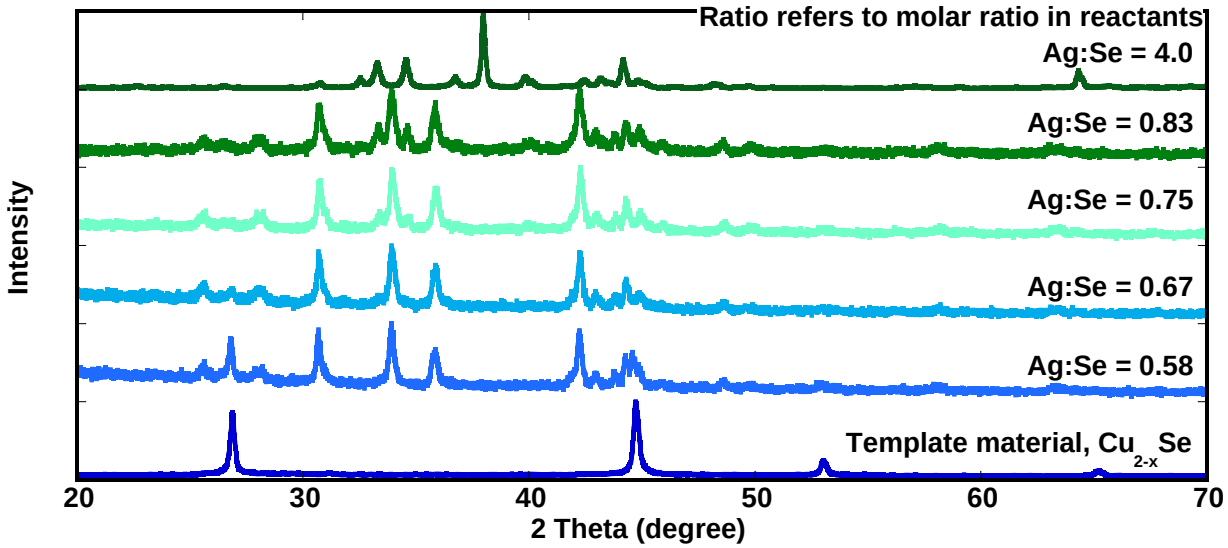

Figure 3-7: XRD patterns of ion exchange reaction products with Ag:Se molar ratio between 1:2 and 1:1 in order to achieve a pure CuAgSe product.

However, we speculate that the phase change near 473 K, results from the high surface energy associated with very small NPs in the β phase. This is due to the fact that in the tetragonal phase, the cubic close packing structure of Se^{2-} ions in the NP is distorted from the energetically

favorable [111] orientation. Therefore, the two phase-transition endothermic events on the DSC plots suggest that the ion exchange reactions result in the formation of CuAgSe NPs with a broad size distribution. This result is consistent with SEM analysis of the starting $Cu_{2-x}Se$ NPs and is also supported by the disappearance of the endothermic event at 473 K from the DSC curve during the second heating run.

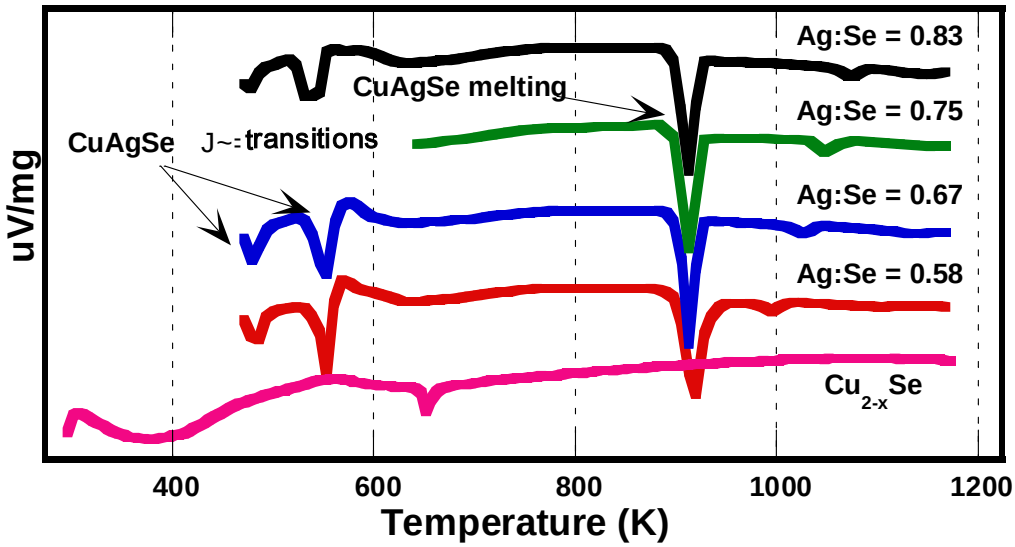

Figure 3-8: DSC data on heating of $Cu_{2-x}Se$ and samples with Ag:Se ratio of 0.58-0.83 showing both β-α CuAgSe transition.

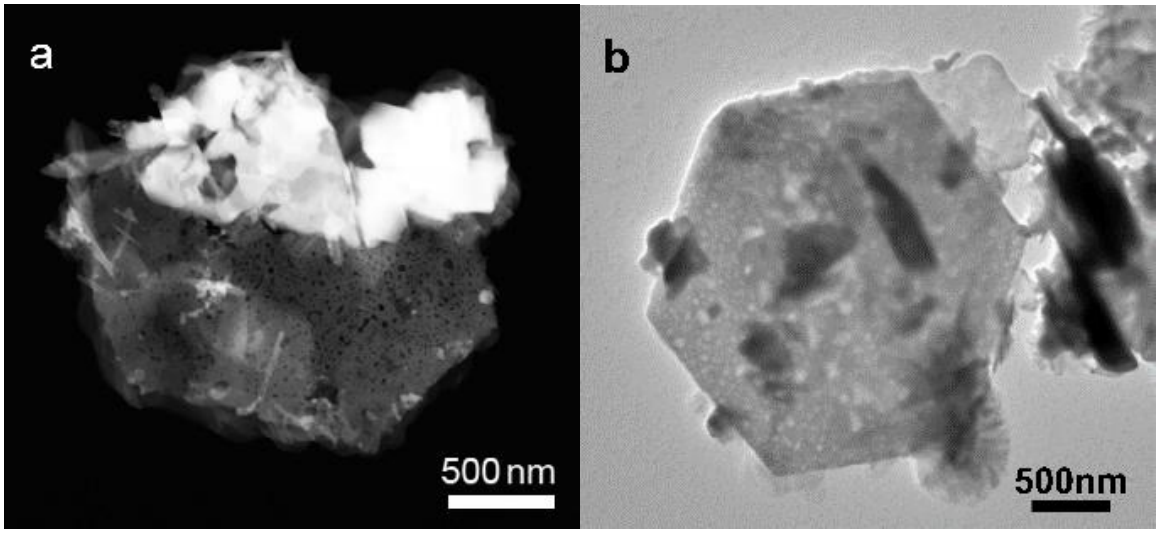

Figure 3-9: a) STEM image of Ag:Se = 1:2 sample showing that the hexagonal morphology of the template NP is maintained during ion exchange reaction. b) HRTEM image of Ag:Se = 1:1.

The DSC data shows that the material is mainly one phase and is stable until the onset of melting at 898 K, which is substantially lower than the reported value of 1053 K for bulk CuAgSe.[119,132] This melting point depression is associated with the reduction in particle size of CuAgSe NPs.[134]

It is particularly interesting to note the stabilization of the cubic phase of CuAgSe through ion exchange reaction at room temperature, which is far below the reported polymorphic transition temperature ($T_{\beta\alpha}$ > 473 K).[132] We believe that the ability to form cubic CuAgSe phase at 298 K through ion exchange reactions is favored by the use of the existing FCC structure of the $Cu_{2-x}Se$ material as a lattice template (Figure 3-6). In addition, the similar of atomic arrangement of Se (FCC) in both cubic $Cu_{2-x}Se$ and α-CuAgSe compounds, the high mobility of the copper cations in the cubic $Cu_{2-x}Se$ superionic phase, and the porosity of the planar surface of the synthesized $Cu_{2-x}Se$ NPs facilitate the ion exchange process between Cu^+ and Ag^+ ions at 300 K leading to the creation of cubic CuAgSe with low input energy.[135] The presence of a larger fraction of tetragonal CuAgSe in the final product indicate that the cubic CuAgSe is metastable under the reaction condition and partially transform to the more stable tetragonal lattice. This ion exchange method can therefore be used as a means to create metastable cubic ternary and quaternary phases of unique materials without the need for high temperature synthesis.

TEM and STEM methods were used to determine if the template morphology had been maintained after the formation of CuAgSe. STEM micrographs (Figure 3-9), showed that the hexagonal shape of the NPs were maintained for Ag:Se ratios of 1:2 and 1:1 with similar size distribution to the template NPs. EDS using TEM showed that silver is distributed throughout the bulk of the NP somewhat uniformly, which indicated that the hexagonal NP consisted mainly of ternary phase material (Figure 3-10 and Figure 3-11).

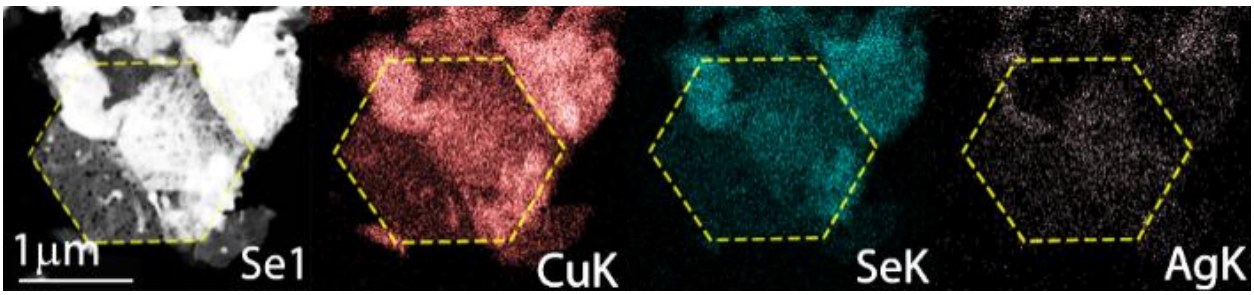

Figure 3-10: EDS mapping of NPs made with Ag:Se ratio of 0.67 showing silver cations distributed within the bulk of the NP, confirming that the $Cu_{2-x}Se$ NP was transformed into CuAgSe phase.

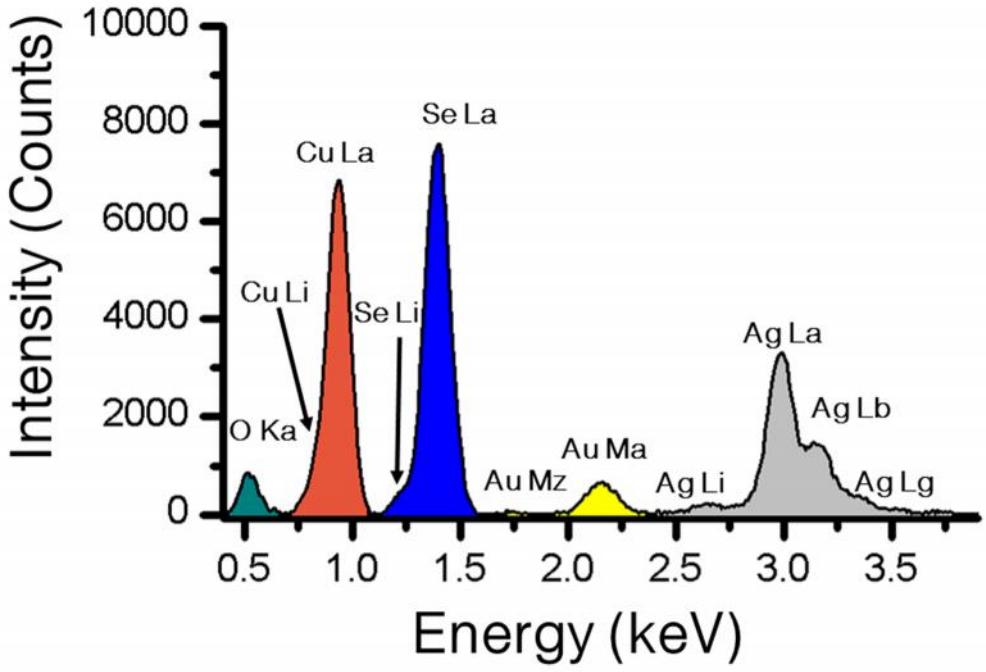

Figure 3-11: EDS spectrum results from NP made with Ag:Se ratio of 0.67 showing Cu, Ag, and Se present. Au presence is due to the TEM grid.

CuAgSe NPs with tetragonal and cubic structures produced using a Ag:Se ratio of 0.71 were consolidated into pellets for thermal and electronic property measurements. A pellet suitable for measurements was pressed at 723 K with a pressure of 100 MPa for 2 hours, yielding a

geometric density of 7.362 g/cm^3 and a true density of 7.2339 g/cm^3, 92% of the theoretical CuAgSe density (7.389 – 7.912 g/cm^3).[136]

Figure 3-12 shows the thermoelectric properties of the synthesized CuAgSe NPs. At 300 K, the total thermal conductivity is 2.7 W/mK and drastically decreases to 0.8 W/mK at the transition from the tetragonal β-CuAgSe to the cubic superionic α-CuAgSe structure. Further increase in the temperature resulted in the drop of the thermal conductivity to 0.4 W/ m K at 775 K (Figure 3-12a). The observed sharp reduction of the thermal conductivity at the phase transition is ascribed to enhance phonon scattering due to the high degree of positional disorder and high mobility of Cu^+ ions in the superionic cubic structure of α-CuAgSe. The total thermal conductivity of CuAgSe NP at various temperatures is comparable to that of bulk CuAgSe prepared by solid-state reaction of the elements.[123]

Temperature dependent thermopower data (Figure 3-12b) revealed negative values at temperatures below the transition from β- to α-CuAgSe, $T_{\beta\alpha}$, indicating electrons as majority charge carriers (n-type). The thermopower of β-CuAgSe gradually decreases with increasing temperatures from -50 μV/K at 300 K to ~-20 μV/K at the vicinity of $T_{\beta\alpha}$ ~ 450 K and surprisingly jumps to a large positive value (+200 μV/K) at a temperature slightly above $T_{\beta\alpha}$. This indicates holes as majority carriers (p-type) in α-CuAgSe. The thermopower continues to increase with temperature reaching a maximum value of +260 μV/K at 675 K. The magnitude of S for the α-CuAgSe NPs is higher than that of bulk CuAgSe obtained by solid-state reaction of the elements.[123] The observed sudden switch of the conduction type from n-type in β-CuAgSe to p-type in α-CuAgSe was also reported in polycrystalline CuAgS and CuAgSe.[123,137] Such change in the conduction type can be associated with the alteration of the electronic structure of CuAgSe due to atomic rearrangement in the β and the α polymorphs.[138] At 300 K the electrical resistivity of

CuAgSe NPs is 5.7 x 10^{-4} Ω cm and increases with temperature to ~1.9 x 10^{-3} Ω cm at a temperature slightly below $T_{\beta\alpha}$. This behavior is consistent with heavily doped semiconducting behavior. The electrical resistivity suddenly increases to 1.5 x 10^{-2} Ω cm slightly above $T_{\beta\alpha}$. This increase in the electrical resistivity is ascribed to a large drop in the overall carrier mobility, due to (1) the change in the majority carrier type from high mobility electrons to low mobility holes and (2) enhanced carrier – impurity scattering arising from the superionic behavior of Cu and Ag ions in Cubic CuAgSe. Above $T_{\beta\alpha}$, the electrical resistivity continues to increase with rising temperature indicating heavily doped p-type semiconducting behavior. The thermoelectric figure of merit, *ZT*, calculated from the above data is shown in Figure 3-12b. At 300 K, the *ZT* value is ~0.05 and remains nearly constant up to the β to α transition, $T_{\beta\alpha}$. Above $T_{\beta\alpha}$, the *ZT* values of the p-type α-CuAgSe phase rapidly increases with temperature reaching ~0.55 at 700 K.

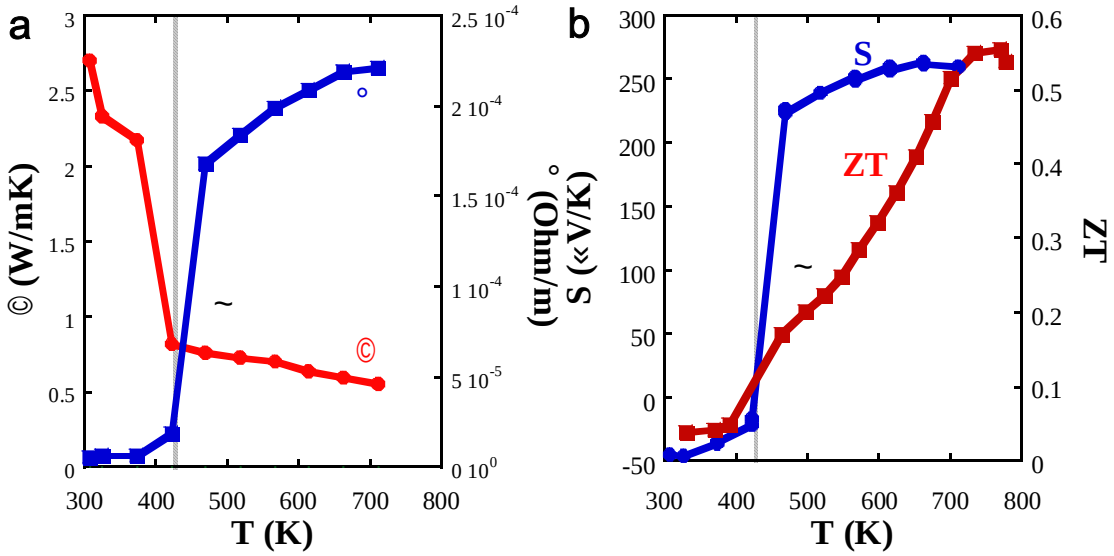

Figure 3-12: a) Temperature dependent thermal conductivity and electrical resistivity of a high-density pellet of CuAgSe NPs showing a sharp drop in the thermal conductivity at the transition from β- to α-CuAgSe. b) Temperature dependence of the Seebeck and ZT, revealing a switching from n-type semiconducting behavior in β-CuAgSe to p-type in α-CuAgSe.

Although this number is slightly lower than the value reported for bulk CuAgSe,[119] it indicates that CuAgSe NPs with promising thermoelectric performance can be fabricated easily at 300 K using a simple and rapid ion exchange reaction between Cu_2Se and Ag^+ salt.

3.4 Conclusions

In conclusion, we report a simple and rapid strategy for the fabrication of both β-CuAgSe (pseudotetragonal) and α-CuAgSe (cubic) NPs at 300 K. Starting from cubic $Cu_{2-x}Se$ NPs template, β-CuAgSe and α-CuAgSe NPs were successfully created at 300 K through partial exchange of Cu^+ ions in $Cu_{2-x}Se$ template by ion Ag^+ ions while maintaining the original morphology of the $Cu_{2-x}Se$ NPs. By varying the ratio of Ag:Se content in the ion exchange reaction we were able to control the composition of the product NPs, and fully transform the $Cu_{2-x}Se$ platelets to Ag_2Se. Electronic and thermal transport properties of CuAgSe NPs consolidated by hot pressing showed low thermal conductivity, high thermopower and moderate electrical resistivity at high temperatures leading to a *ZT* value of 0.55 at 700 K. This work demonstrates that the aforementioned simple two-step batch process could potentially be used for cost-efficient and energy efficient fabrication of NPs of various materials suitable for thermoelectric, photovoltaic, and spintronic applications.

3.4.1 Application of this synthesis technique to other material systems

The novelty of the low-temperature two-step synthesis approach investigated above lies in the potential to create metastable phases of desirable compounds constrained by the morphology of the template nanoplatelet itself. This could lead to the creation and stabilization of cubic forms of other ternary chalcogenide compounds that could be unattainable by other synthesis routes.

In addition to the conversion of $Cu_{2-x}Se$ to CuAgSe nanoplatelets using $AgNo_3$ as a donor reactant, a series of experiments using different donor reactants have been conducted in attempts to create $CuAlSe_2$, Cu_2BaSe_2, $Cu_{2-x}Sr_xSe_2$, $CuInSe_2$, and $Cu_{2-x}Au_xSe$. In place of $AgNo_3$, $AlCl_3$, $BaNO_3$, $SrNO_3$, $In(SO_4)_3$, and AuCl were used as electrolyte salts. In place of ethanol, water was used as a medium to dissolve both AuCl and $AlCl_3$. All other experimental procedures that were used to produce CuAgSe were followed, including varying the molar concentration of reactants. Preliminary data, including XRD patterns, indicates that only $CuAlSe_2$ of this series was produced. With a Al:Se reactant molar ratio of 0.49 the ion exchange reaction produced a multi-phase compound 42.2 wt. % $Cu_{1.8}Se$, 39.5 wt. % CuSe, and 18.3 wt. % $CuAlSe_2$, Figure 3-13. Contrary to the results of $Cu_{2-x}Se$ to CuAgSe conversion, much higher concentrations of Al:Se were necessary to convert significant portions of the nanoplatelets to $CuAlSe_2$. The development of the CuSe, which exhibits a hexagonal structure (space group *P63/mmc*, #194), indicates that this is a necessary intermediate step between the cubic $Cu_{2-x}Se$ and the tetragonal $CuAlSe_2$ structure, Figure 3-14. Hence, it can be reasoned that the conversion of $Cu_{2-x}Se$ nanoplatelets to other systems is driven in large part due to conformity between the template and final lattice. Since $CuAlSe_2$ does not exhibit a cubic structure at moderate or low temperatures, unlike CuAgSe, the formation of the hexagonal CuSe structure could then be seen as a limiting step in the reaction.

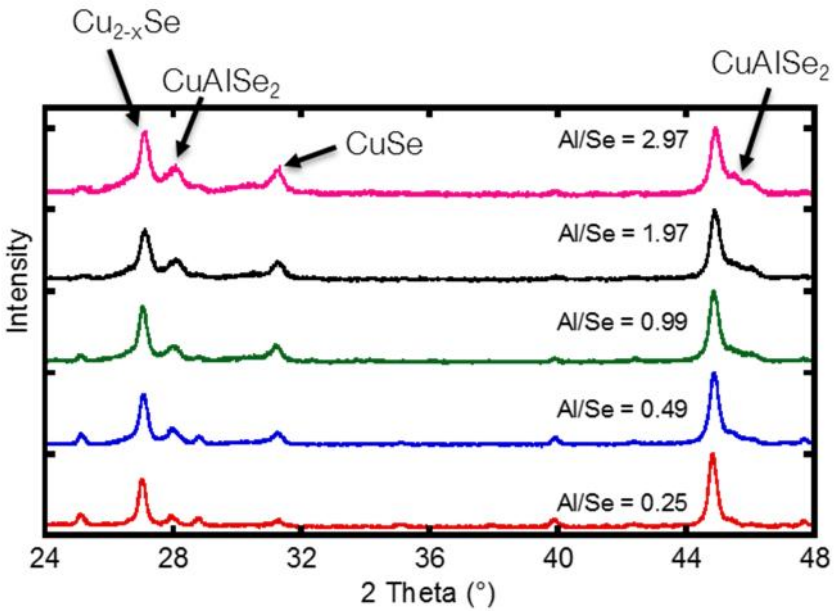

Figure 3-13: XRD results of ion exchange reactions attempting to produce $CuAlSe_2$ from $Cu_{2-x}Se$ nanoplatelets. Molar ratio of reactants is shown on right.

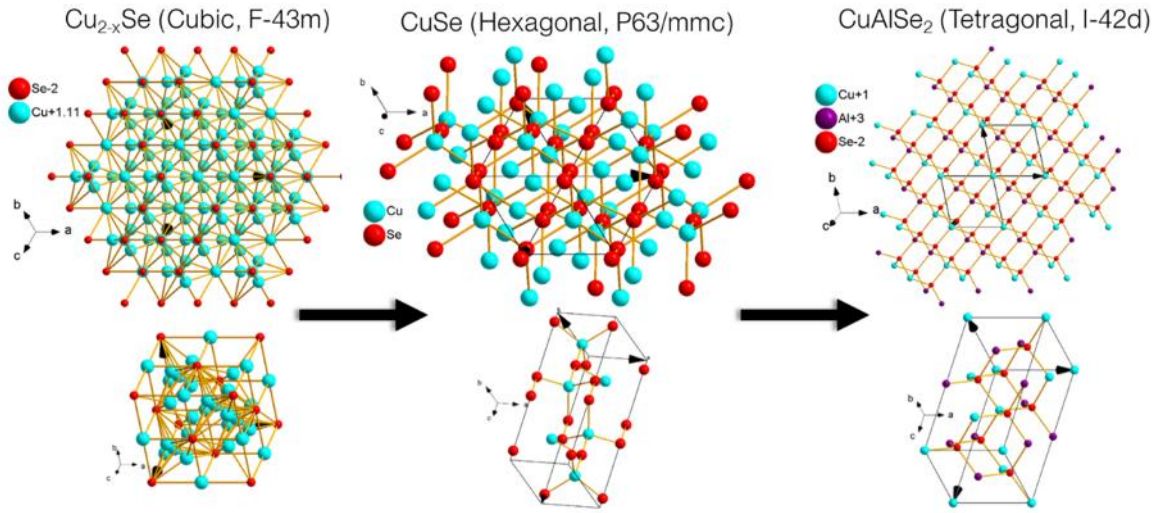

Figure 3-14: Schematic of conversion of $Cu_{2-x}Se$ to CuSe to $CuAlSe_2$ shown from the [111] direction.

These findings indicate that there is potential to use this process to create nanostructures of other interesting compounds, and further, that there is a strong correlation between the lattice of the template structure and the final compound that determines the aggressiveness or completion of the conversion. Further work should investigate the creation of CuSe nanoplatelets in order to convert more easily into $CuAlSe_2$ structures, as well as experimentation with other copper-based

chalcogenide nano-templates that feature a variety of lattice types. This would elucidate the compatibility of future template-converted synthesis processes and broaden the applicability of this interesting batch manufacturing method.

CHAPTER 4

$CuAl(S_xSe_{1-x})_2$ SOLID SOLUTIONS DOPED WITH TRANSITION METALS AS POTENTIAL THERMOELECTRIC MATERIALS

4.1 Introduction

As copper-based chalcogenide compounds such as $Cu_{2-x}Se$ and $CuInSe_2$ have proven to offer significant thermoelectric and photovoltaic performance due to interesting physical properties such as superionicity[123,139-142] and the ability to tune optical band gaps,[143,144] they have renewed interest in the study of the physical properties of similar compounds. Since many of these desirable physical properties are derived from the order-disorder of the structure, permitting high mobility of copper ions within a rigid chalcogen anionic lattice,[145-147] focus has been placed on the replacement or substitution of transition metal cations,[148] but also on the role that solid solutions based on variations of the chalcogen plays.[149-151] This then drives the interest in the study of other copper based chalcogenide systems for potential use as thermoelectric materials, or potentially even multifunctional materials offering high photovoltaic and thermoelectric conversion efficiency. Hence, the focus of this study is the investigation into the thermoelectric properties of well-known photovoltaic $CuAlS_2$, and lesser known $CuAlSe_2$.

$CuAlS_2$ was first developed in the early 1960s as a wide band gap semiconductor for photovoltaic applications, particularly the possibility of blue LEDs,[152] followed by the development of $CuAlSe_2$. The band gap of this material was determined to be the highest of any

of the chalcopyrite compounds studied for light emitting applications at ~3.5 eV, which is substantially higher than the reported values for $CuAlSe_2$, ~2.5 eV.[153] Many studies concerning the alloying of the two chalcopyrite structures,[154-157] as well as significant doping studies have centered on the promise of these two compounds as providing extremely high absorption coefficients in the UV range.[158] Recently published density functional theory studies conducted by Reshak have shown the potential for solid solutions of polycrystalline $CuAl(S_xSe_{1-x})_2$ materials as highly efficient thermoelectric materials, offering significantly high p-type thermopower with reasonable electronic conductivity, and low thermal conductivity, and ultimately figures of merit approaching 0.9 at temperatures as low as 450 K.[157] To date, there have not been experimental validation of the thermoelectric performance of these materials.

In this study a series of $CuAl(S_xSe_{1-x})_2$ samples are produced with various stoichiometry, dopants, and processing approaches in order to evaluate the potential of these materials to offer high thermoelectric performance. Samples with chemical composition $CuAl(S_xSe_{1-x})_2$ where x = 0, 0.25 0.5, 0.75, and 1, are produced by means of both mechanical alloying and solid state synthesis in order to probe the effect of crystallite size on the thermal transport of these materials. Doping by substitution of transition metals, Ag in place of Cu^+, Hf, Ti, and Zr in place of Al^{3+}, is also investigated in an attempt to improve the electronic transport of the system and also reduce the thermal conductivity of the materials. Finally, densification by hot pressing and spark plasma sintering was considered as these materials are significantly affected by defects.

4.2 Experimental

Two synthesis techniques were used to produce transition metal doped and undoped samples of $CuAl(S_xSe_{1-x})_2$, solid state synthesis and mechanical alloying.

4.2.1 Solid state synthesis

Compositions of $CuAl(S_xSe_{1-x})_2$ where x = 0, 0.25, 0.5 0.75, 1, and compositions doped with Ag, Hf, Ti, and Zr, were fabricated by standard solid state reaction of elements at high temperature in fused silica tubes. Stoichiometric amounts of elemental powder Cu (Sigma Aldrich, 99.7%), Al (Sigma Aldrich, 99.5%), S (Sigma Aldrich, 99.5%), Se (99.5%, Sigma Aldrich), Ag (Sigma Aldrich, 99%), Hf (American Elements, 99.5%), Ti (Sigma Aldrich, 99.7%), and Zr (Sigma Aldrich, 99.5%) were weighed and mixed by hand in an agate mortar and pestle in a glovebox under an argon atmosphere. Finely ground powders were then added to silica tubes and flame sealed with residual pressure of 10^{-4} Torr. The tubes were then placed in mullite tubes with insulating ends, and heated to 1073 K in 12 hours, dwelled for 48 hours, then cooled to room temperature in 12 hours. The synthesized materials were then transferred to mortar and pestle and ground into fine powders under and Ar atmosphere in a glovebox. Powders ranged in color from light green gray ($CuAlS_2$) to dark orange brown ($CuAlSe_2$) and did not show evidence of melting.

4.2.2 Mechanical alloying synthesis

Compositions of $CuAl(S_xSe_{1-x})_2$ where x = 0, 0.25, 0.5 0.75, 1, were fabricated by mechanically alloying using high-energy ball-milling. 2.5 g of stoichiometric amounts of powder elements were milled for 6 hours to complete synthesis. The color and consistency of the mechanically alloyed powders closely resemble those produced by solid state reaction.

4.2.3 Densification

Both hot pressing and spark plasma sintering were used to produce pellets of $CuAl(S_xSe_{1-x})_2$ samples. For hot pressing, approximately 1.5 g of synthesized powder was added to a graphite die with graphite anvils and densified at a pressure of 100 MPa at a temperature of 773 K for 2

hours of dwell time with a ramp up and down rate of 225 K/hr in a residual atmosphere of 10^{-2} Torr. Once reaching room temperature, pellets were extracted from the graphite die and polished with metallographic paper. For spark plasma sintering similar steps were followed, and pellets were produced by heating powder to 1073 K for 10 minutes at a pressure of 50 MPa in residual pressure of 10^{-3} Torr with a ramp up and down rate of 50 K/min.

4.3 Results and Discussion

$CuAlS_2$ and $CuAlSe_2$ both exhibit the tetragonal chalcopyrite structure, which is a reduction in symmetry compared to the closely related zinc-blende sphalerite structure, at room temperature, space group $I\bar{4}2d$ (#122), with Cu^{1+} ions positioned in the 4a Wyckoff site, at the vertices of the unit cell, Al^{3+} positioned at the 4b site, and the chalcogen atoms at the 8d site. In this way, tetragonal chalcopyrites can be seen as a superlattice of sphalerite structures.

4.3.1 Structure and determination of solid solution

A comparison of X-ray powder diffraction profiles for solid-state and mechanically alloyed synthesized $CuAl(S_xSe_{1-x})_2$ compounds is shown in Figure 4-1. All samples other than mechanically alloyed x = 0.5 show peaks that can be correlated to either $CuAlS_2$ or $CuAlSe_2$ known diffraction patterns. It is readily apparent from the progression of the (112) peak to lower 2θ angles with increasing Se content that upon substitution of Se for S the unit cell expands. This is consistent with the slightly larger ionic radius of selenium compared to sulfur and the lower electronegativity of Se compared of S, which would indicate a higher bond iconicity and, thus, a shorter bond length between sulfur anion and transition metal cations. The peak at ~43° indicates that $Cu_{2-x}Se$ impurity phases were created. For all other phases, no indication of impurity phase is present by examination of the diffractograms. Rietveld refinement, using FullProf software, was utilized to determine the

lattice parameters of each mechanically alloyed synthesized compound.[159] The results are plotted in Figure 4-2, of which the linear relationship between x and lattice parameter verifies that these compounds follow Vegard's law and are indeed solid solutions of $CuAlS_2$ and $CuAlSe_2$.

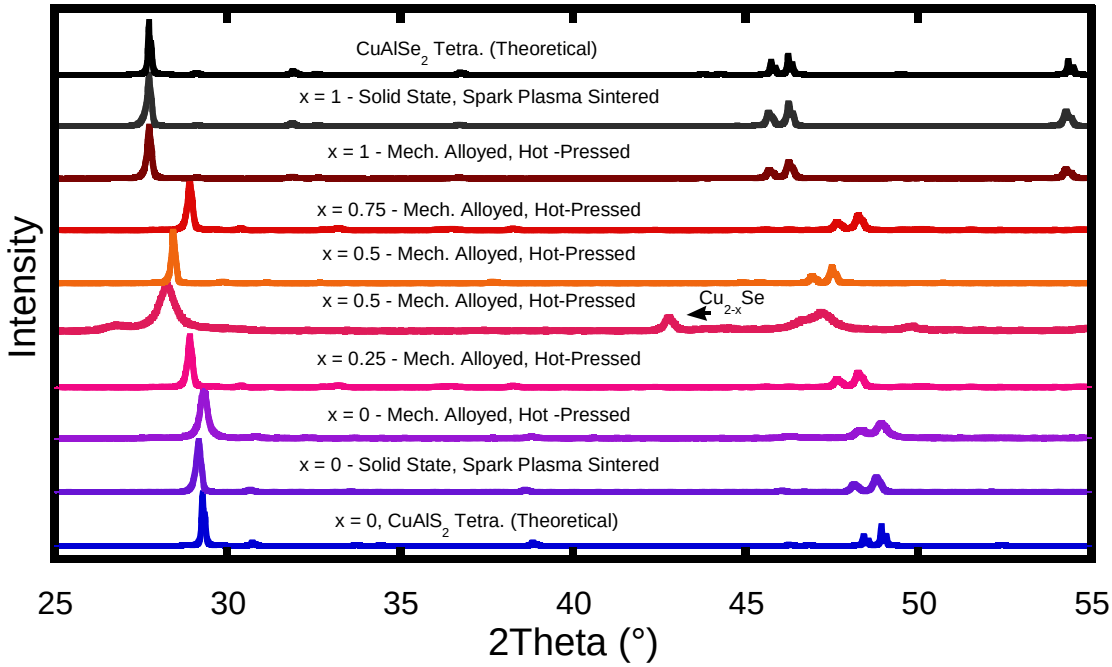

Figure 4-1: X-ray diffraction patterns of $CuAl(S_xSe_{1-x})_2$ solid solutions produced via mechanical alloying and hot pressing, compared to solid solutions produced by solid state synthesis and spark plasma sintering.

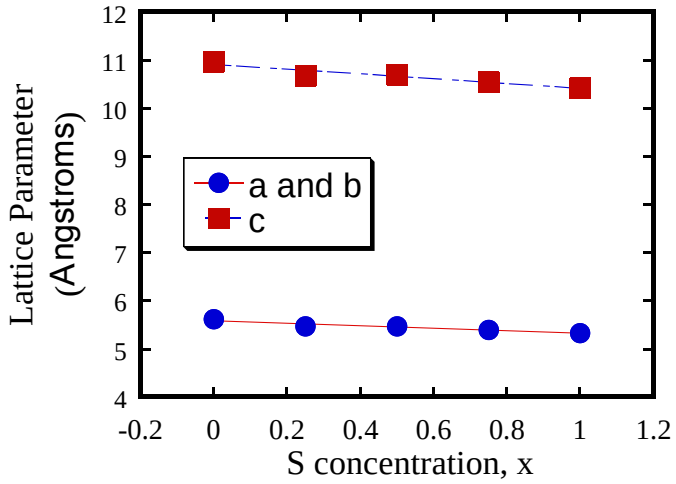

Figure 4-2: Refined lattice parameters for pellets of $CuAl(S_xSe_{1-x})_2$ produced by mechanical alloying and hot pressing. Both a, b and c lattice parameters decrease linearly with increasing S content, indicating solid solution alloying.

Differential scanning calorimetry results of the $CuAlS_2$ and $CuAlSe_2$ samples are shown in Figure 4-3. Solid-state synthesized $CuAlS_2$ shows no phase transitions or thermal events associated with impurity phases, without a clear melting event occurring in temperatures up to 1373 K, which is consistent with the melting point reported elsewhere as 1570 K. $CuAlSe_2$ features a series of thermal events at ~673 K and ~800 K that appear to be due to small amounts of impurity phases, potentially Al_2Se_3 or $Cu_{2-x}Se$. The onset of melting near 1273 K is consistent with previously reported thermogravimetric analyses conducted on $CuAlSe_2$.

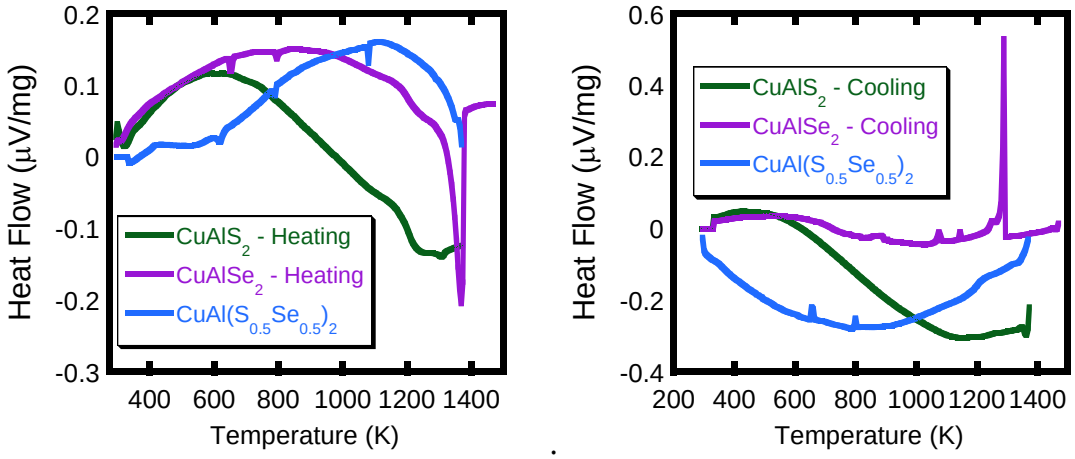

Figure 4-3: Left) Differential scanning calorimetry (DSC) heating signals for $CuAlS_2$, $CuAlSe_2$, and $CuAl(S_{0.5}Se_{0.5})_2$ produced by solid state synthesis. Right) Corresponding DSC cooling signals.

4.3.2 Thermoelectric properties

Densified samples were polished with metallographic paper and analyzed for thermal conductivity using the laserflash method. All tested samples yielded a true density at least 92% of the theoretical density, Table 4-1. A comparison of the thermal conductivities of samples synthesized by solid-state methods compared to that of the mechanically alloyed samples is shown in Figure 4-4.

Table 4-1: Pycnometer and theoretical densities for pellets of $CuAl(S_xSe_{1-x})_2$ samples.

	Synthesis Technique	(ρ^{pyc} g/cm³)	(ρ^{theo} g/cm³)	% of ρ^{theo}
$CuAlS_2$	Mech. Alloying	3.46	3.42	101%
$CuAl(S_{0.75}Se_{0.25})_2$	Mech. Alloying	3.86	3.79	102%
$CuAl(S_{0.5}Se_{0.25})_2$	Mech. Alloying	4.11	4.10	100%
$CuAl(S_{0.25}Se_{0.75})_2$	Mech. Alloying	4.00	4.33	92%
$CuAlSe_2$	Mech. Alloying	4.59	4.73	97%
$CuAlS_2$	Solid-State	3.47	3.42	101%
$CuAl(S_{0.5}Se_{0.5})_2$	Solid-State	4.46	4.10	109%
$CuAlSe_2$	Solid-State	4.66	4.73	99%

$CuAlSe_2$, independent of synthesis technique, yields a higher thermal conductivity, from ~2.9 W/mK at 273 K to ~1 W/mK at 873 K, than $CuAlS_2$ compounds, ~1.7 W/mK at 273 K to ~1 W/mK at 873 K, and other solid solution compounds. This is due to a much higher electronic contribution to the total thermal conductivity, likely due to the excess of charge carriers present in Se compared to S. Alloyed compounds of mixtures of $CuAlS_2$ and $CuAlSe_2$ exhibit thermal conductivities between $CuAlS_2$ and $CuAlSe_2$, with the exception of the mechanically alloyed $CuAl(S_{0.5}Se_{0.5})_2$ sample; however, this sample appears to have formed substantial impurity phases based on analysis of the X-ray diffractograms. Whereas mechanically alloying, known for reducing crystallite size and introducing phonon scattering grain boundaries, reduced the thermal conductivity of the $CuAlSe_2$ sample compared to that produced by solid-state synthesis, this was not true for the $CuAlS_2$ sample. It's possible that the extended time and high temperature during hot pressing could have caused significant recrystallization, enlarging grains and eliminating the effects of mechanical alloying more significantly that with the $CuAlSe_2$ sample.

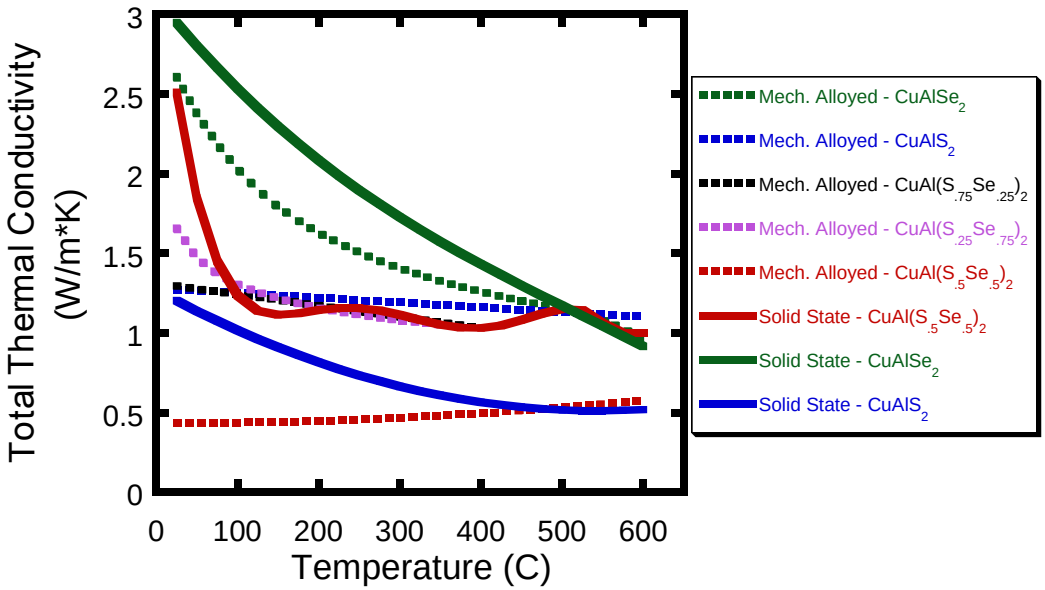

Figure 4-4: Thermal conductivity of $CuAl(S_xSe_{1-x})_2$ samples produced by mechanically alloying and by solid state synthesis. All samples were densified by hot pressing.

Figure 4-5 shows little effect from the densification technique on the thermal conductivity of sample, other than the anomalous increase in shown in the $CuAlS_2$ compound. It is not clear as to why spark plasma sintering would increase the thermal conductivity nearly two-fold at temperatures lower than 773 K, however, one possible answer is that the high resistivity of the compound could create substantial local heating during sintering, beyond that sensed by the thermocouples in the system, creating impurity phases that with higher thermal conductivity. Figure 4-6 compares the effect of substitutional doping at the Cu^+ site compared to the Al^{3+} site with transition metals synthesized by solid-state means in $CuAlSe_2$. Ag^+ ions were substituted for Cu^+, resulting in a slight decrease in thermal conductivity particularly at temperatures lower than 650 K. At 873 K both 5 and 10 mol. % doped samples yield thermal conductivities similar to undoped $CuAlSe_2$, ~1 W/mK.

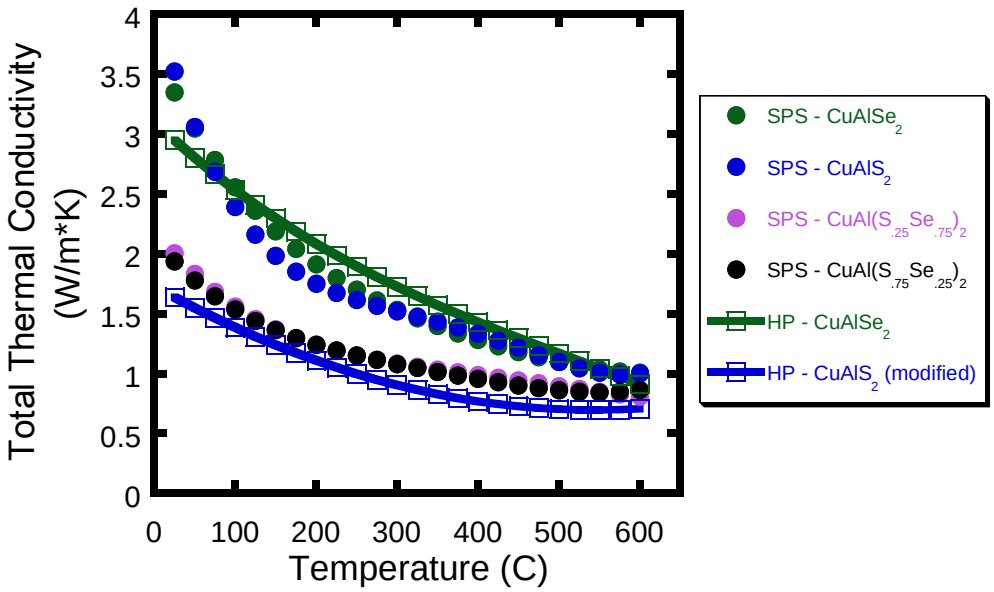

Figure 4-5: Effect of densification method, spark plasma sintering (SPS) compared to hot pressing (HP), on thermal conductivity of $CuAl(S_xSe_{1-x})_2$. SPS samples doped with Hf in place of Al are also considered.

The mass fluctuation from Cu^+ to Ag^+ ions can explain the small reduction though means of increased phonon scattering. 5 mol. % Hf^{4+}, Ti^{4+}, and Zr^{4+} were used to dope at the Al^{3+} site in $CuAlSe_2$, which is expected to increase the carrier concentration of holes in the system by removing electrons, but also significantly scatter phonons through mass fluctuation. This doping did in fact dramatically reduce the thermal conductivity over then entire temperature range, reaching that of the porous solid- state $CuAlS_2$; ~0.57 W/mK at 873 K. There is no significant difference in the thermal conductivity given the species of dopant at the Al^{3+} site, indicating that mass fluctuation reaches a diminishing effect. It is not likely that a majority of the reduction in thermal conductivity is due to the reduction in the electronic contribution to thermal conductivity given the increased number of carriers that could lead to further phonon scattering since the electronic conductivities are low for all materials, Figure 4-6.

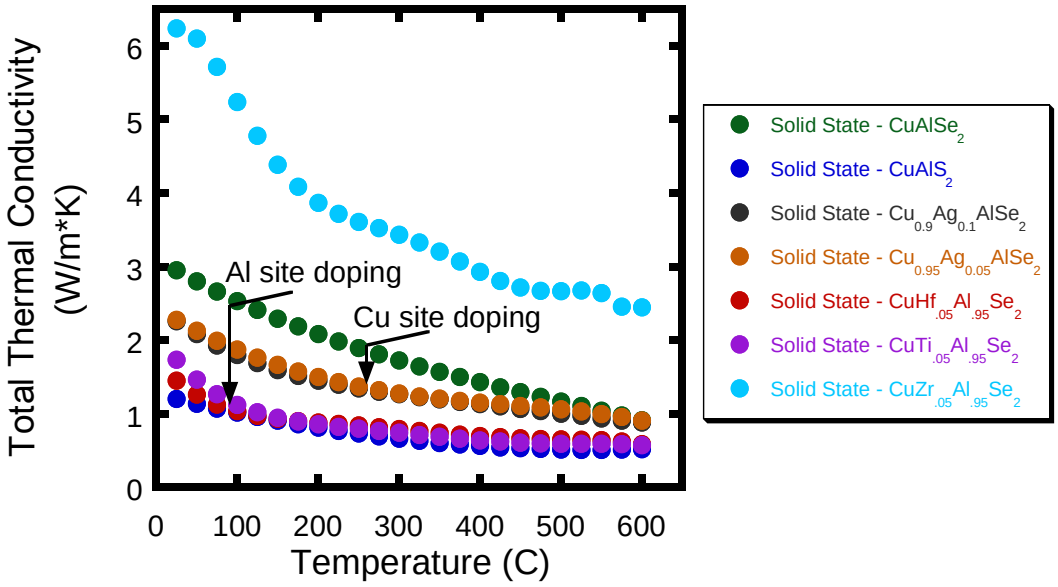

Figure 4-6: Effect of doping at the Cu^{1+} site and the Al^{3+} site on the thermal conductivity of $CuAl(S_xSe_{1-x})_2$ samples synthesized by solid state synthesis and densified by hot pressing.

The electronic conductivity, reported in Figure 4-7, falls far below the predicted values by Reshak, necessary for high *ZT* values.[157] $CuAlSe_2$, produced by solid-state synthesis and hot pressing, yielded the highest electronic conductivity of all samples tested, 30 S/cm at 273 K and decreasing to 17 S/cm at 450 K then increasing again to a maximum of 47 S/cm at 873 K. the sharp increase at 673 K for $CuAlSe_2$ could be caused by the small impurity phases discovered by DSC analysis. The Ag^+ doped samples yield lower conductivity than the undoped $CuAlSe_2$, with maximum conductivity of 19 S/cm at 500 K for the 5 mol. % doped sample, and 14 S/cm at 500 K for the 10 mol. % doped sample. Interestingly, the Hf^{4+} doped sample yielded higher conductivity than both the Ag^+ doped samples, and somewhat tracking the undoped sample. It can, therefore, be elucidated that the conductivity of this material is generally due to the mobility of Cu^+ ions such that replacing Cu^+ with the slightly less mobile Ag^+ significantly reduces the conductivity, but that replacing Al^{3+} with Hf^{4+} does little to affect the electronic conductivity. $CuAlS_2$ yielded the lowest electronic conductivity of all samples, exhibiting insulating behavior, reaching a maximum of only 0.28 S/cm at 873 K.

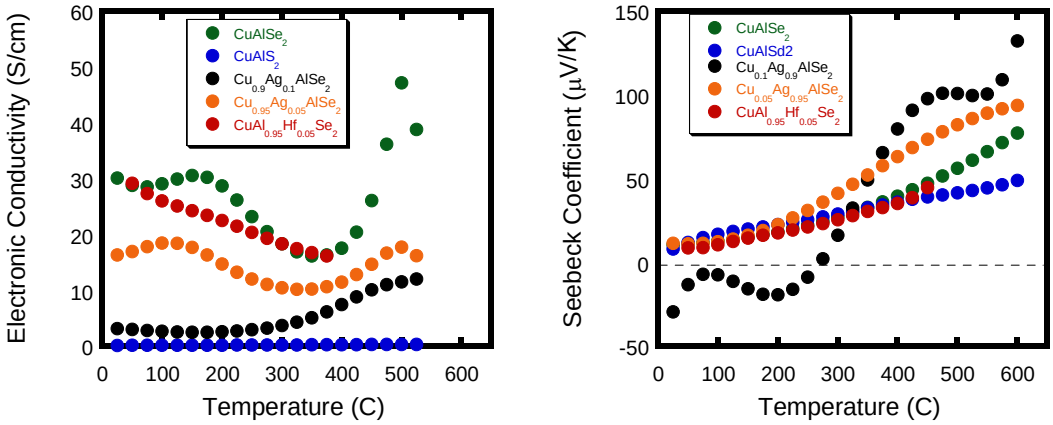

Figure 4-7: Left) Electronic conductivity and right) Seebeck coefficient of solid state synthesized and hot-pressed samples.

The Seebeck coefficient for each solid-state and hot-pressed sample is plotted in Figure 4-7, again falling short of the predicted values by DFT calculations. All samples show p-type behavior, except for the 10 mol. % doping of Ag^{+} below 275 K, which shows n-type Seebeck coefficient. The Seebeck coefficient for $CuAlSe_2$ and $CuAlS_2$ similarly start near 10 μV/K at room temperature, then increase to 38 μV/K at 700 K, then diverge with $CuAlSe_2$ increasing to a maximum of 77 μV/K at 873 K. Hf^{4+} doping does not affect the Seebeck coefficient of $CuAlSe_2$, which is consistent with the findings of the effect on electronic conductivity, further verification that substitutional doping at the Al^{3+} site does not change the electronic structure of the system. Interestingly, doping of 5 mol. % Ag^{+} for Cu^{+} increased the Seebeck coefficient for $CuAlSe_2$ at temperatures above 473 K, rising to a maximum of 94 μV/K at 873 K, suggesting that the carrier concentration in the system is reduced, which would also explain the sharp reduction in electronic conductivity. The 10 mol. % Ag^{+} sample exhibited a minimum value of -30 μV/K at 273 K then rises to a maximum of 132 μV/K at 873 K, the highest of any of the samples. The strong change in room temperature Seebeck coefficient from the 5 to 10 mol. % Ag^{+} doped samples points to a solubility of Ag^{+} in $CuAlSe_2$ that could be less than 10 mol. %, such that impurity CuAgSe phase is created that has been reported to exhibit a very similar thermopower profile. While the reduction

in electronic conductivity effectively reduces the value of this doped material as a promising thermoelectric, the possibility of creating CuAgSe nanoparticles within a $CuAlSe_2$ bulk offers an exciting potential for further microstructural engineering.

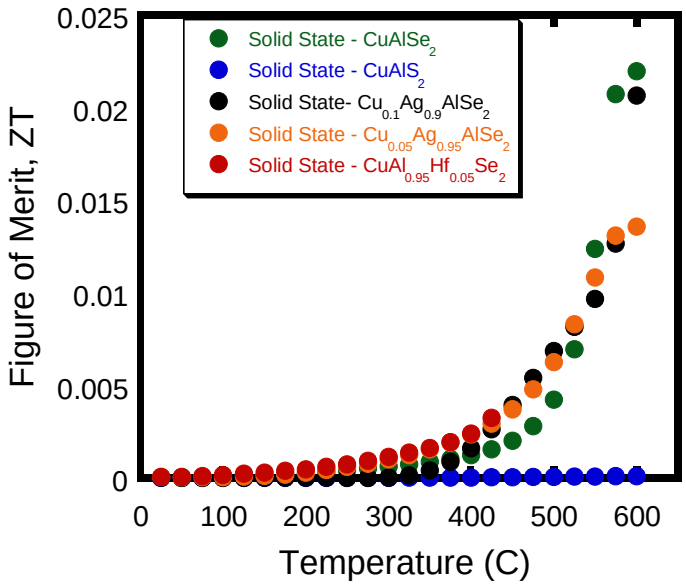

Figure 4-8: Figure of merit, ZT, of solid state synthesized then hot-pressed pellets of $CuAl(S_xSe_{1-x})_2$ and Ag doped samples.

The figure of merit, *ZT*, for all solid-state and hot-pressed samples too low for thermoelectric application, shown in Figure 4-8, and far below the values of *ZT* predicted by DFT calculations. $CuAlSe_2$ and 10 mo. % doped Ag^+ yield the highest value, reaching 0.021 at 873 K. The Hf^{4+} doped sample produces a higher *ZT* than all other materials at low temperature, but must be tested at higher temperatures in order to gain a direct comparison.

4.4 Conclusions

A series of $CuAl(S_xSe_{1-x})_2$ samples and samples doped with transition metals Ag, Hf, Ti, and Zr were synthesized using mechanical alloying and solid state synthesis. The effects of these synthesis methods, dopants, and densification techniques (hot pressing and spark plasma sintering)

on the thermoelectric performance of these materials was investigated spurred by the potential for high *ZT* predicted by DFT simulations. It was determined that solid solutions of $CuAl(S_xSe_{1-x})_2$ could be produced for all values of x. The thermal conductivity of all samples reaches near 1 W/mK which is surely sufficient for thermoelectric application. S-rich samples exhibited much lower thermal conductivity at lower temperature than Se-rich samples. It was also determined that mechanical alloying provided little reduction in thermal conductivity, but that doping of Ag^+ at the Cu^+ site substantially reduced the thermal conductivity, and even more so for doping of Hf^{4+}, Zr^{4+}, and Ti^{4+} at the Al^{3+} site. Most interestingly, through electronic transport characterization and analysis it was determined that a majority of the charge carriers are derived from the mobility of Cu^+ ions, allowing doping at the Al^{3+} site without affecting the electronic structure of the system. While the thermoelectric performance of these materials is quite disappointing, especially for power generation or refrigeration use, the possibility of further engineering of these notable compounds for multifunctional use can now target specific doping at each cation and anion position with some knowledge as to the effects.

CHAPTER 5

INDIUM PREFERENTIAL DISTRIBUTION ENABLES ELECTRONIC ENGINEERING OF MAGNETISM IN $FeSb_{2-x}In_xSe_4$ P-TYPE HIGH-TC FERROMAGNETIC SEMICONDUCTORS

5.1 Introduction

Transition metal chalcogenide compounds continue to attract tremendous attention as fertile playground for the discovery of next generation materials for use in thermoelectric,[45,160] photovoltaic,[161,162] and magnetic applications[163-169] due to their semiconducting nature, and their compositional and structural flexibilities, which enables engineering of specific magnetic and transport properties through doping, substitution or other means.[170,171] Furthermore, these compounds tend to adopt low-dimensional crystal structures, which can be modulated by controllable external stimuli for specific applications in spintronics and memory devices.[92,172-181] This combination of properties potentially leads to the development of multifunctional electronic and spintronic components, with the promise of improved energy efficiency and computing capability. In order to unlock the full potential of these material systems, careful engineering of the physical, electronic, thermal and magnetic properties through atomic substitution and, or doping of parent structures is necessary.

Recently, Djieutedjeu et al. demonstrated that the p-type transition metal chalcogenide, $FeSb_2Se_4$, exhibits ferromagnetism and semiconductivity above 300 K, and a reversible semiconductor-to-insulator transition below 130 K.[182] The monoclinic structure (space group *C2/m*, #12) of $FeSb_2Se_4$ can be divided into two layered building units, denoted as A and B (Figure 5-1), which alternate along [001]. Within layer A, octahedrally coordinated Fe atoms, $[Fe(3)]Se_{4+2}$, share edges to form a single-chain parallel to [010] that alternates along the *a*-axis with a double-chain of face-sharing monocapped trigonal prisms around M1(*4i*) positions. The M1 site in the structure of $FeSb_2Se_4$ is predominantly occupied by Sb atom (96%) with a small fraction (4%) of Fe atoms. Layer B is a NaCl-type unit consisting of octahedrally coordinated M4(*2a*) and M2(*4i*)

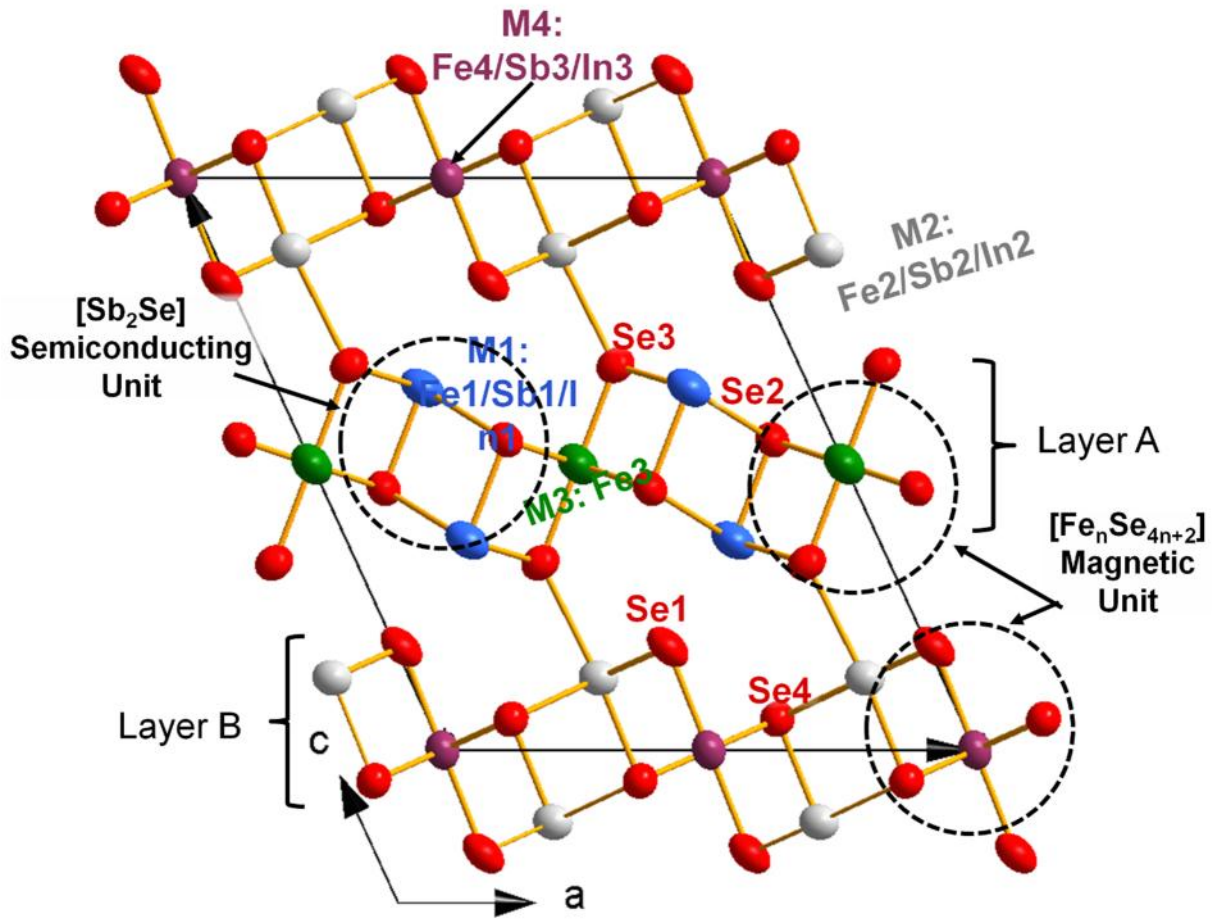

Figure 5-1: Schematic representation of the structure of $FeSb_{2-x}In_xSe_4$ projected down the b-axis showing the distribution of In at the M1(4i), M4(2a) and M2(4i) sites.

sites, which are mixed occupied by Sb and Fe (M2 = 96%Sb/4%Fe and M4 = 86%Fe/14%Sb) in the structure of $FeSb_2Se_4$. Layer A, given its high content of magnetic atoms, is considered to be responsible for the ferromagnetic-like behavior of $FeSb_2Se_4$ samples. The low symmetry of the $FeSb_2Se_4$ crystal structure enables independent manipulation of the chemistry of the magnetic (M3(*2d*) and M4(*2a*)) and non-magnetic (M1(*4i*) and M2(*4i*)) sublattices in order to tailor its electronic or magnetic properties. For instance, a recent study targeting Sn substitution at Fe sites ($Fe_{1-x}Sn_xSb_2Se_4$) indicated a preferential insertion of Sn at M4(*2a*) sites, and an increased ordering at the M1(*4i*) and M2(*4i*) positions.[183] For the composition with x = 0.13, the M1(*4i*) and M2(*4i*) positions are fully occupied by Sb atoms while the magnetic Fe atoms are only found at the M3(*2d*) and M4(*2a*) sites. This increase ordering of Fe atoms within the crystal structure led to a drastic decrease of the Curie transition temperature from 450 K for the sample with x = 0 to 325 K for the sample with x = 0.13 as well as a sharp drop on the thermopower presumably due to alterations in the electronic band structure near the Fermi level.[183] This significant alteration of the magnetic and electronic behavior due to change in the atomic ordering within the crystal structure is a potentially advantageous property for device applications, and highlights the impetus to further investigate means of p-type doping via substitution at the Sb sites ($FeSb_{2-x}M_XSe_4$).

Beyond band gap engineering through the redistribution of Fe atoms, isoelectronic doping can potentially also increase the carrier concentration through localized disruption of the electronic structure as recently shown by Jin et al. in a study discussing p-type doping of elemental bismuth with indium.[184] This work indicated that a doping agent with similar valence to the host could disrupt the core electrons, which in principle could avoid the effects of ionized impurity scattering. Group III element, In, was shown to act as a compensated partial acceptor, but with poor doping efficiency. Still, In doping improved the thermoelectric figure of merit, *ZT*, for the system. The

technique of increasing the carrier concentration without inducing an electronic change can be useful for magnetic applications.

In order to further understand the mechanisms driving the magnetic, electronic and thermal behavior of $FeSb_2Se_4$, we have investigated the effect of isoelectronic substitution of Sb by In, $FeSb_{2-x}In_xSe_4$, on the crystal structure as well as the magnetic and electronic properties. It is anticipated that the introduction of In at the Sb site will be isomorphic maintaining the parent lattice intact while increasing the carrier concentration of the p-type ferromagnetic semiconductor, $FeSb_2Se_4$. Therefore, this should enable probing the systematic response to electronic engineering at the Sb site only. While In and Sb share a +3 valence, the electron distribution of each ion is substantially different with the Sb^{+3} ($4d^{10}5s^2$) valence moving from characteristic s-orbital to the d-orbital character in In^{+3} ($4d^{10}$). It is anticipated that this change in bonding character will engineer the shape of the electronic band structure to provide more carriers in the form of holes. This affords a method to tune the carrier concentration of a semiconductor without introducing new scattering centers. In this work, various compositions of the solid-solution series $FeSb_{2-x}In_xSe_4$ compounds where x = 0, 0.05, 0.01, 0.125, 0.2 and 0.25, were prepared using standard solid-state synthesis techniques. The crystal structure of each sample was studied in detail using Rietveld refinement of powder X-ray diffraction patterns and X-ray photoelectron spectroscopy, which yielded insight into the distribution of metal atoms (In, Sb, Fe) within the crystal structure as well as their oxidation states. These results were then correlated to observed alteration in the electronic, thermal and magnetic properties of the synthesized materials.

5.2 Experimental

5.2.1 Synthesis and processing.

Several compositions of the $FeSb_{2-x}In_xSe_4$ series where x = 0, 0.05, 0.1, 0.125, 0.15, 0.2 and 0.25, were fabricated by standard solid-state reaction of the elements. Stoichiometric amounts of powder elements Fe (+99%, Alfa Aesar), In (+99%, Alfa Aesar), Sb (99%, Alfa Aesar), and Se (99.5%, Sigma Aldrich) were weighed and mixed by hand using an agate mortar and pestle within a glovebox under Ar atmosphere. The combined powders were sealed in fused silica tubes under a residual pressure of 10^{-4} Torr and heated to 573 K in 24 hours, held at that temperature for 24 hours, then heated to 773 K in 12 hours, held at that temperature for 96 hours, and finally cooled to room temperature in 24 hours. This process produced a fine, dark gray powder that did not show any evidence of melting. Densification of pellets was conducted under a residual pressure of 10^{-2} Torr, a pressing temperature of 723 K for 1 hour and an applied pressure of 100 MPa with a ramp up and down rate of 362 K/hour. All pellets yielded both a geometric and true density that was greater than 97% of the theoretical density.

5.2.2 Characterization

Powder X-ray Diffraction and Rietveld refinement. Phase analysis and the crystal structure of various compositions in both powder and pellet form was determined by powder X-ray diffraction (XRD) techniques. Rietveld refinement was performed on the diffraction patterns from the pellet samples using FullProf software package [113] in order to determine the lattice constants, unit cell volume and the distribution of metal atoms in the structure. The crystal structure of selected $FeSb_{2-x}In_xSe_4$ compositions was refined using the structure of $FeSb_2Se_4$ compound as the starting structure model. In the monoclinic crystal lattice of $FeSb_2Se_4$ (space group *C2/m*, #12), the configuration of atoms is such that there exists four independent metal positions, filled by Fe and Sb and four chalcogenide (Se) positions. These four metal sites are M1 and M2, both located at the Wyckoff position *4i*, M3 at special position *2d*, and M4 at the special position *2a*. Refinement

of single crystal diffraction data showed that the M3 and M4 sites are predominantly occupied by Fe, with the M3 fully occupied by Fe. The M1 and M2 sites are predominantly occupied by Sb, with a small fraction of Sb occupying the M4 site.[182] The procedure for Rietveld refinement of diffractograms from each pellet samples, using FullProf software, employed the simulation of peak shape by Thompson-Cox-Hastings pseudo-Voight * axial divergence asymmetry and followed a strict methodology to determine the position and occupancy of each atom as represented in Figure 5-2. First, the diffractogram of the x = 0 sample was refined and used as an initial input control file (PCR file) for each subsequent refinement of x > 0 samples. The background was first refined using a three-order polynomial with global relaxation factor of 1.0. The scale was then refined, separately from the background. The lattice parameters *a*, *b*, *c* and *β* were then individually refined while continuing to refine the scale. The peak shape of the pattern was then refined by means of 2-parameter asymmetry and refining the Caglioti parameters *u* (positive values), *v* (negative values), and *w* (positive values). The 14 individual atomic positions, Se1 – Se4, Sb1 – Sb3, Fe1 – Fe4 and In1 – In3, were then refined simultaneously. The occupancies for the x = 0 pattern were not refined as they were derived from single crystal diffraction data. The atomic positions and

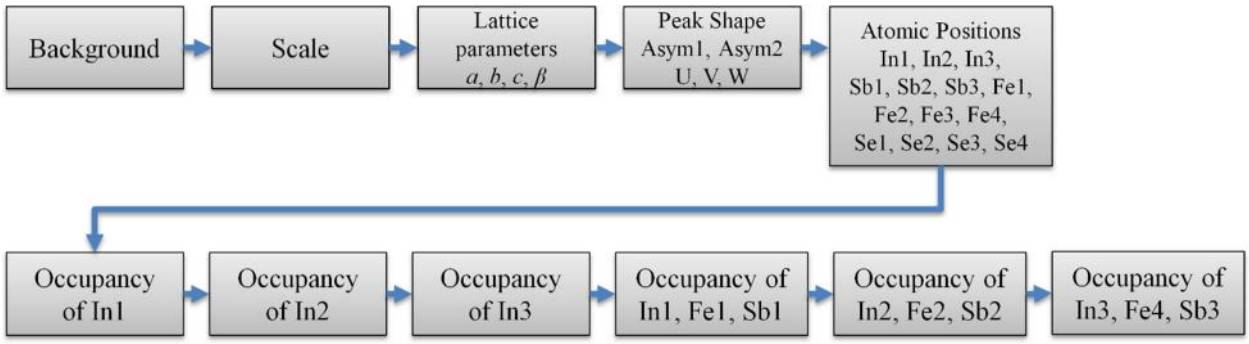

Figure 5-2: Rietveld refinement scheme used in FullProf software to determine the location and occupancy of each atom within the unit cell for various $FeSb_{2-x}In_xSe_4$ samples.

occupancies of x = 0.1, 0.2 and 0.25 samples are reported in Table 5-3. Refined interatomic distances for x = 0.1, 0.2 0.25 compositions are also reported in Table 5-4. This technique yielded

a very accurate fit between the simulated profile and the experimental data. This PCR file, referred to as $PCR_{x=0}$, was then used to refine the simulated profile for the $x > 0$ pellet diffractograms with further processing including occupancy refinement. After $PCR_{x=0}$ was loaded, the refinement of $x > 0$ samples continued by refining the background, then the scale, then the lattice parameters as before, the peak shape using both asymmetry and Caglioti parameters, and finally the individual atomic positions all using a global relaxation factor of 1.0. While this produced an accurate fit for all diffractograms $x > 0$, (Figure 5-4) the position and intensity of the (004) peak at ~30.1° appeared to be strongly correlated to the In content and became a focal point of the refinement of the occupancy factors. Three potential sites for In were identified as M1, M2 and M4 assigned as In1, In2, and In3 respectively for refinement. The occupancy of each species of atom at each atomic site was refined by first assuming that Se1, Se2, Se3 and Se4 were fully occupied, then refining the In concentration at each In site, then the Sb concentration at each Sb site, the Fe at each Fe site, and finally a combination of In, Sb, and Fe at the M1, M2 and M4 sites. All refinement utilized global relaxation factors of 0.25. To determine which sites the In preferred, the occupancy of the In1 site was refined with a starting value of 16% filled without refining other sites. After convergence, the same process was used to refine the In2 and In3 occupancies again starting with values of 16% occupancy for each. If a site was refined to a negative occupancy factor it was concluded that In did not occupy that site and an occupancy of 0% was utilized at that site for further refinement. In2 (position M2) and In3 (position M4) occupancies converged to negative occupancies for $x \leq 0.1$, indicating that In does not reside in those positions for those dopant concentrations; thus, the concentration was set to 0% for further refinement. For compounds $x > 0.1$ the refined occupancy of In3 converged to positive values and for $x = 0.25$ the refined occupancy of In2 converged to positive values; hence, it was concluded that In^{+3} resided at these

positions at those threshold concentrations. Sb occupancy was then individually refined at M1, M2 and M4 sites. Refinement of Fe at M1, M2, and M4 sites followed as well. Refinement of a combination of species at each specific metal site was then performed, i.e. simultaneous refinement of In1, Sb1, and Fe1. The calculated density and calculated chemical composition obtained in the OUT file produced by FullProf were then compared with the experimentally obtained values, which correlated well for all refined diffractograms.

5.3 Results and Discussion

5.3.1 Crystal structure of $FeSb_{2-x}In_xSe_4$

The comparison of the XRD patterns of the as synthesized powder samples of the $FeSb_{2-x}In_xSe_4$ series with the theoretical pattern calculated from the single crystal refinement of $FeSb_2Se_4$ (ICSD 421938)[182] revealed excellent matching of all diffraction peaks on the experimental patterns with peaks on the theoretical pattern (Figure 5-3) suggesting that the In-substituted phases, $FeSb_{2-x}In_xSe_4$ phases are isostructural with the parent compound, $FeSb_2Se_4$. Careful examination of the XRD patterns from the powder and pelletized samples (Figure 5-3) showed no structural change

or phase decomposition due to densification at high pressure and high temperature. It is clear, however, that with increasing In content the (004) peak shifts to higher angles. This is consistent

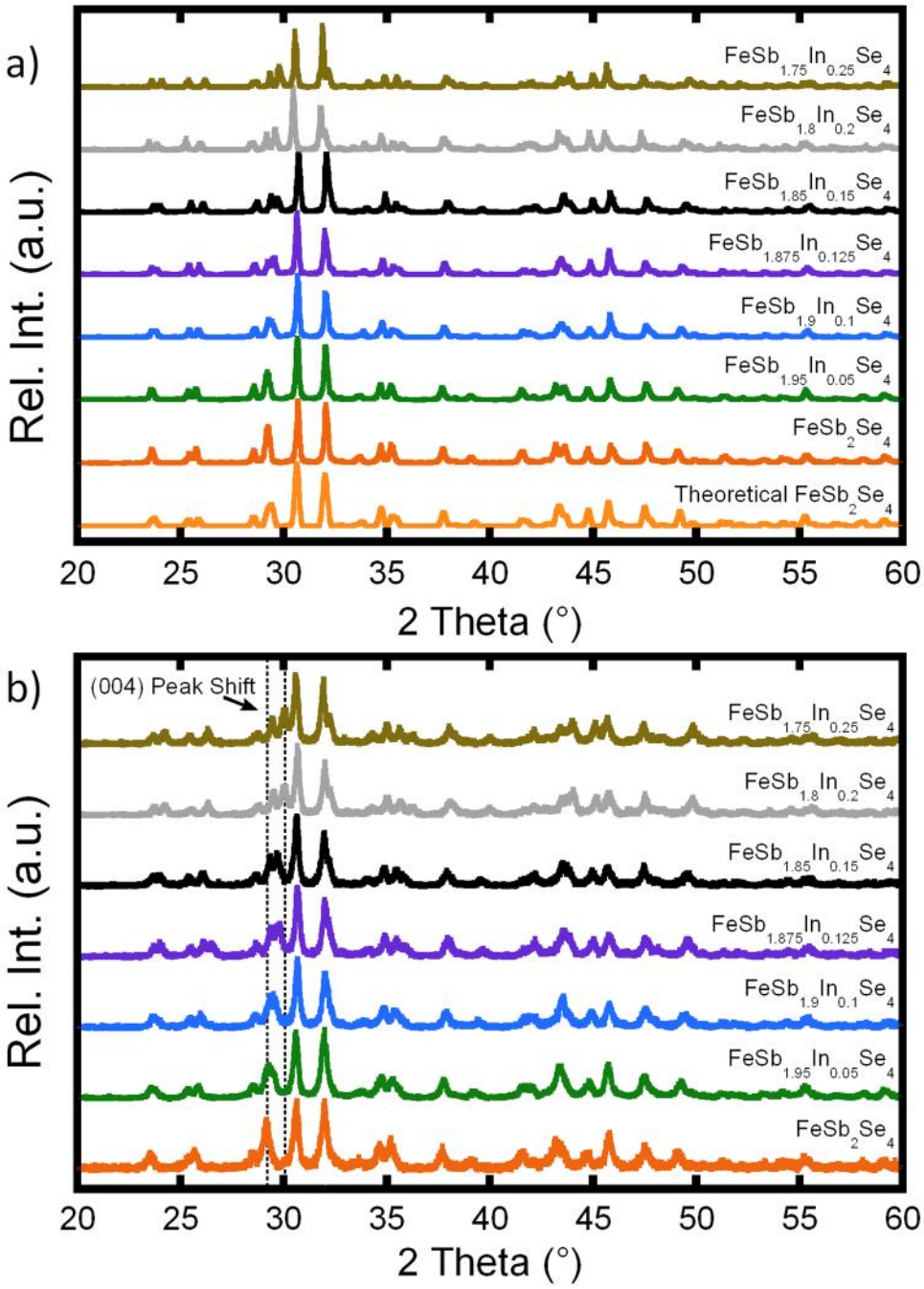

Figure 5-3: Powder X-ray diffraction patterns of various $FeSb_{2-x}In_xSe_4$ samples. a) As synthesized powders, b) after hot pressing. Both series of XRD patterns show the characteristic symmetry of the $FeSb_2Se_4$ structure regardless of In content. The shift in the (004) peak is more pronounced on the XRD patterns of hot-pressed samples presumably due to the annealing.

with the very small reduction in the *c* lattice parameter, from 15.2440 (1) Å for x = 0 to 14.8769(5) Å for x = 0.25 (Table 5-1).

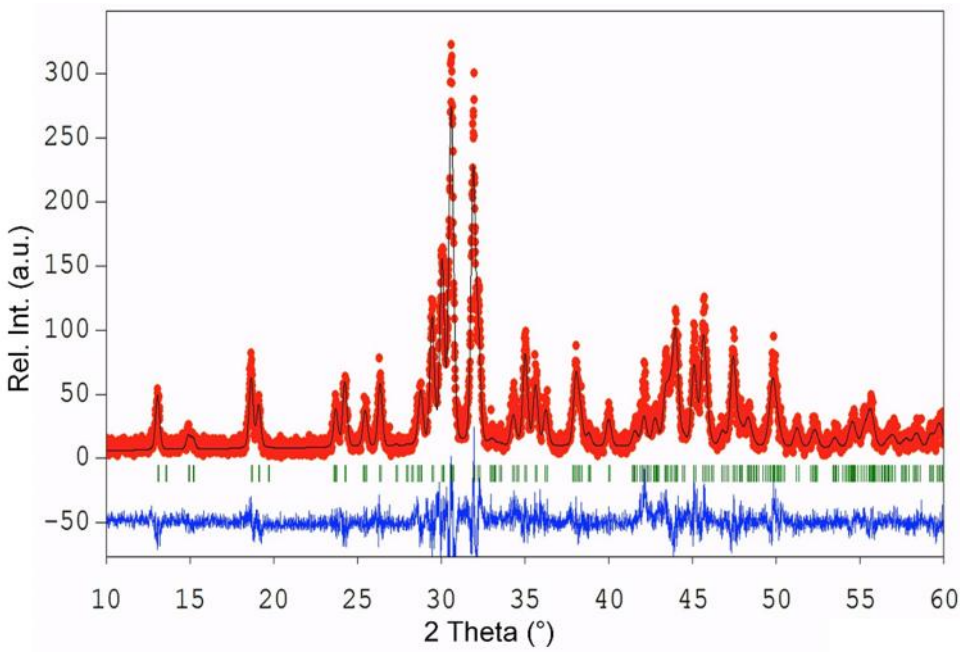

Figure 5-4: Rietveld refinement of XRD pattern from a $FeSb_{2-x}In_xSe_4$ pellet sample with x = 0.25.

The unit cell parameters and distribution of various metal atoms within the crystal structures of $FeSb_{2-x}In_xSe_4$ was determined by Rietveld refinement on XRD patterns from the pellets using FullProf software package, an example of which is shown in Figure 5-4.[113] EDS spectral results confirm that the composition of each synthesized compound is close to the targeted stoichiometry (Table 5-2), particularly with respect to the In content (Figure 5-5). The results of the refinement with respect to lattice parameters and unit cell volume are shown in Table 5-1 and the distribution of In atoms at various metal positions is shown in Table 5-3. No significant change in the lattice parameters *a*,

Table 5-1: Results of Rietveld refinement using X-ray diffractograms from $FeSb_{2-x}In_xSe_4$ pellets

Composition	Indium content	Cell parameters				Cell volume ($Å^3$)	*Refinement parameters*		
		a(Å)	*b*(Å)	*c*(Å)	β(°)		R_{f1}	R_{f2}	Chi
$FeSb_2Se_4$	0	13.067 (7)	3.960 (2)	15.244 (2)	115.1 (5)	714.5	15.7	12	1.5
$FeSb_{1.95}In_{0.05}Se_4$	0.05	13.077 (1)	3.970 (7)	15.160 (3)	114.9 (8)	713.8	10.8	6.6	2.2
$FeSb_{1.9}In_{0.1}Se_4$	0.1	13.045 (7)	3.962 (1)	15.101 (6)	114.9 (3)	707.9	10.1	6.2	1.5
$FeSb_{1.875}In_{0.125}Se_4$	0.125	13.036 (8)	3.963 (2)	15.014 (6)	114.8 (3)	703.9	10.4	6.7	1.8
$FeSb_{1.85}In_{0.15}Se_4$	0.15	13.075 (5)	3.974 (5)	15.055 (1)	114.8 (3)	710.3	12.6	7.3	1.6
$FeSb_{1.85}In_{0.2}Se_4$	0.2	13.031 (1)	3.967 (2)	14.893 (5)	114.7 (5)	699.4	12.1	8.0	1. 7
$FeSb_{1.75}In_{0.25}Se_4$	0.25	13.058 (6)	3.974 (3)	14.878 (3)	114.7 (7)	701.5	13.5	8.7	1.9

b and *c* was observed upon increasing In content. This is consistent with the small difference (ΔR/R = 5.3%) in the ionic atomic radii of Sb^{+3} (0.76 Å) and In^{3+} (0.8 Å) in octahedral coordination Figure 5-7.[185] However, a slight distortion of the monoclinic angle, β, was observed, which resulted in a small reduction in unit cell volume with increasing In content. The refinement of the

Table 5-2: Electron dispersive spectroscopy (EDS) and WDXRF results for each synthesized compound.

Sample	**Fe (at %, by WDXRF)**	**Fe (at%, by EDS)**	**Sb (at%, by EDS)**	**In (at%, by EDS)**	**Se (at%, by EDS)**
$FeSb_2Se_4$	1.538	0.776	1.704	0.000	4
$FeSb_{1.95}In_{0.05}Se_4$	0.906	0.722	1.649	0.081	4
$FeSb_{1.9}In_{0.1}Se_4$	1.244	0.753	1.685	0.105	4
$FeSb_{1.875}In_{0.125}Se_4$	1.066	0.828	1.819	0.127	4
$FeSb_{1.85}In_{0.15}Se_4$	1.026	0.766	1.675	0.157	4
$FeSb_{1.8}In_{0.2}Se_4$	1.012	0.739	1.572	0.182	4
$FeSb_{1.75}In_{0.25}Se_4$	0.996	0.818	1.660	0.256	4

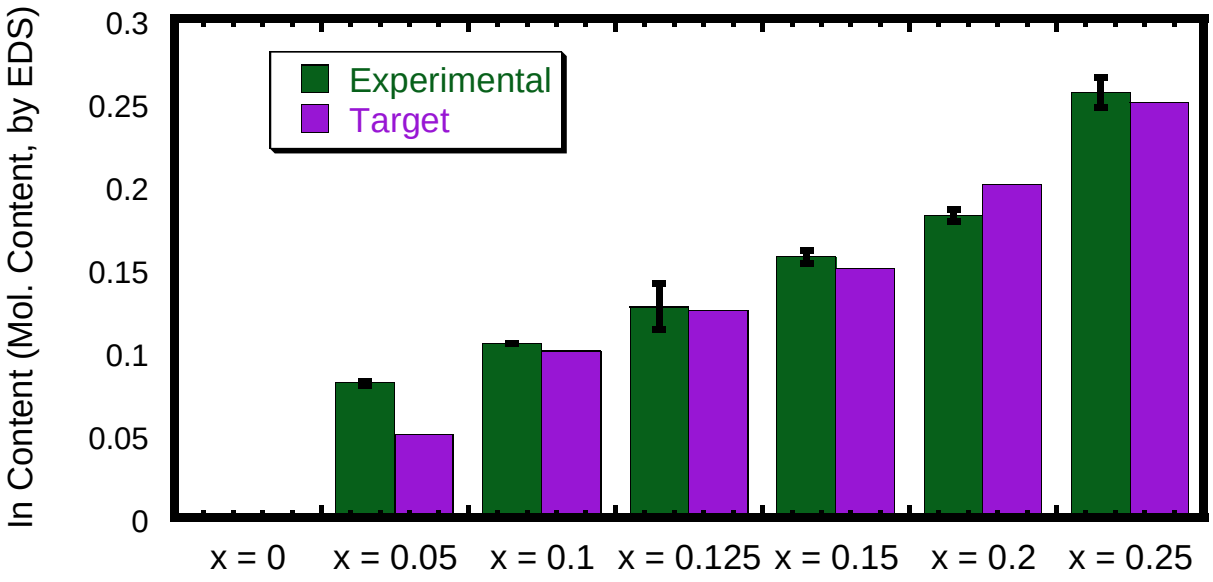

Figure 5-5: In content of each sample determined by EDS as compared to targeted value.

distribution of metal atoms at various metal positions was performed assuming a full occupancy of anions sites by Se atoms. The refinement results show that In^{+3} initially prefers to displace Sb^{+3} at the M1(*4i*) position and saturates at that position at a concentration of ~10% (x = 0.1), then begins to fill the M4 (*2a*) and finally the M2 (*4i*) position as the concentration of In increases (Figure 5-6). Interestingly, the substitution of Sb^{+3} by In^{+3} at various metal positions did not alter the distribution of Fe atoms in the structure. As observed in the structure of $FeSb_2Se_4$, the M3(*2d*) position in the structure of $FeSb_{2-x}In_xSe_4$ phases is exclusively occupied by Fe atoms, whereas various fractions of Fe are also found at M1(4%), M2(4%) and M4(84%). This change in the preferential distribution of In atoms at various metal positions in the crystal with the concentration of In atoms can lead to a drastic alteration in the electronic and magnetic properties of the samples.

The purity of the synthesized polycrystalline powders of $FeSb_{2-x}In_xSe_4$ phases as well as the effect of In substitution on the melting temperature was assessed using differential scanning calorimetry (DSC). The DSC heating curves shown in Figure 5-8 exhibit a single endothermic

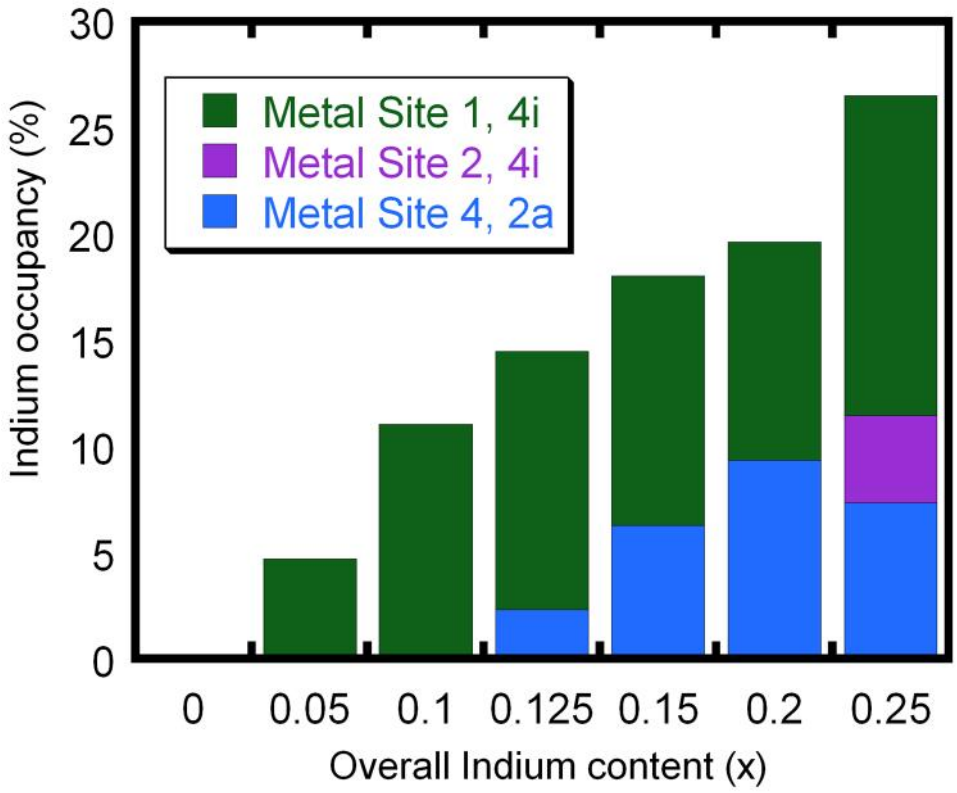

Figure 5-6: Results of Rietveld refinement of occupancy of In showing substitution for Sb^{+3} at the M1(4i) site, followed by substitution of Sb^{+3} at the M2(4i) and M4(2a) sites in the structure of $FeSb_{2-x}In_xSe_4$.

event for each sample, which is attributed to the congruent melting of the sample. Interestingly, the melting point of various samples slightly increases with In content from ~878 K for the In-free sample (x = 0) to 896 K for the sample with x = 0.25. This trend is quite surprising given the lower melting point of In (~430 K) compared to that of Sb (~904 K). However, it is consistent with the observed small contraction of the unit cell volume as well as the shortening of M – Se bond distances in the crystal structure (Table 5-3). The observed contraction of bond distances can be rationalized by the slightly larger electronegativity difference of In/Se pair of atoms compared to Sb/Se, which implies the formation of bonding with increasing ionicity, hence the observed increasing melting point of $FeSb_{2-x}In_xSe_4$ phases with In content. To further confirm the isoelectronic substitution of Sb^{3+} by In^{3+} in $FeSb_{2-x}In_xSe_4$ phases, the oxidation states of In atoms in various samples was probed using X-ray photoelectron spectroscopy (XPS). The spectrum of

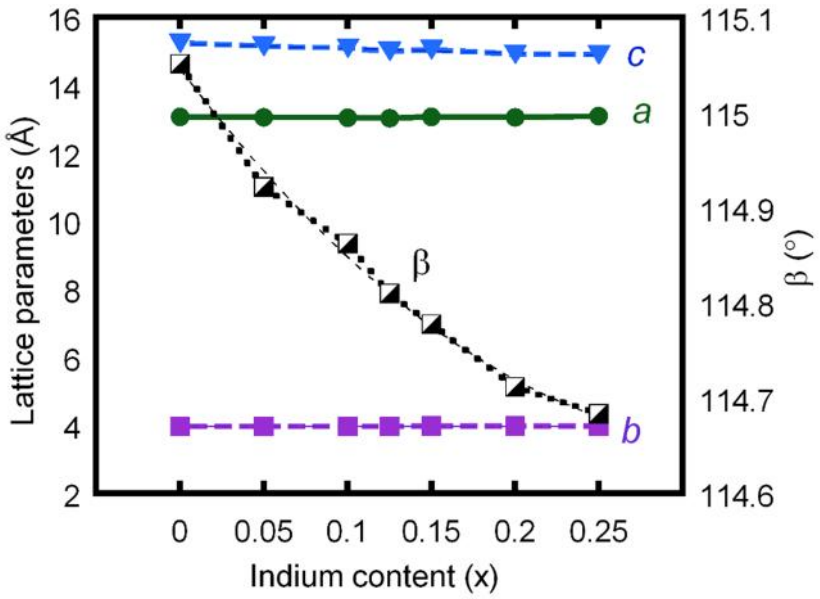

Figure 5-7: Dependence of the lattice parameters on In content obtained from Rietveld refinement performed on all XRD patterns taken from the pelletized and polished $FeSb_{2-x}In_xSe_4$ samples. While the lattice parameters a, b and c remain relatively constant with varying Indium content, the β angle decreases, which reduces the cell volume.

In_3d shell electrons for each substituted sample is shown in Figure 5-9. It can be seen clearly that the In^{+3} peak intensity increases with In content, confirming an effective insertion of In into the crystal structure. Furthermore, the binding energies of the $In\_3d_{5/2}$ and $In\_3d_{3/2}$ peaks in various samples remain constant at 444.54 eV and 452.13 eV, respectively, which are consistent with the values reported in In_2Se_3.[186] One can conclude based on the XPS data that In remains in the +3 oxidation state in all samples. This further supports the structure refinement results, which indicated that In atoms exclusively enter metal positions previously occupied by Sb atoms in the parent structure. Therefore, the substitution is isoelectronic and maintains both the local and overall electroneutrality of the samples regardless of the In content. This analysis is consistent with the observed constant values of oxidation states of Fe(+2), Sb(+3) and Se(-2) in all samples (Figure 5-10).

Table 5-3: Refined distribution of atoms at various metal positions for selected $FeSb_{2-x}In_xSe_4$ compositions (x = 0.1 (1st line), x = 0.2 (2nd line), x = 0.25 (3rd line)).

	Atom	x	y	z	Occupancy
M1(4i)	Sb1	0.2765(1)	0.00000	0.6343(1)	0.739(2)
		0.2790(1)	0.00000	0.6364(1)	0.754(2)
		0.2781(1)	0.00000	0.6359(1)	0.659(2)
	Fe1	0.2765(1)	0.00000	0.6343(1)	0.040(2)
		0.2790(1)	0.00000	0.6364(1)	0.040(2)
		0.2781(1)	0.00000	0.6359(1)	0.040(2)
	In1	0.2765(1)	0.00000	0.6343(1)	0.221(2)
		0.2790(1)	0.00000	0.6364(1)	0.206(2)
		0.2781(1)	0.00000	0.6359(1)	0.301(2)
M2(4i)	Sb2	0.3563(1)	0.00000	0.1295(1)	0.980(2)
		0.3555(1)	0.00000	0.1309(1)	0.940(2)
		0.3571(1)	0.00000	0.1333(1)	0.857(2)
	Fe2	0.3563(1)	0.00000	0.1295(1)	0.02(2)
		0.3555(1)	0.00000	0.1309(1)	0.06(2)
		0.3571(1)	0.00000	0.1333(1)	0.06(2)
	In2	0.3563(1)	0.00000	0.1295(1)	0.000
		0.3555(1)	0.00000	0.1309(1)	0.000
		0.3571(1)	0.00000	0.1333(1)	0.083(2)
M3(2d)	Fe3	0.00000	0.50000	0.50000	1
		0.00000	0.50000	0.50000	1
		0.00000	0.50000	0.50000	1
M4(2a)	Sb3	0.00000	0.00000	0.00000	0.152(2)
		0.00000	0.00000	0.00000	0.150(2)
		0.00000	0.00000	0.00000	0.149(2)
	Fe4	0.00000	0.00000	0.00000	0.848(2)
		0.00000	0.00000	0.00000	0.757(2)
		0.00000	0.00000	0.00000	0.778(2)
	In3	0.00000	0.00000	0.00000	0.000
		0.00000	0.00000	0.00000	0.093(2)
		0.00000	0.00000	0.00000	0.073(2)
Se1		0.0120(2)	0.00000	0.1792(2)	1
		0.0121(1)	0.00000	0.1835(1)	1
		0.0057(1)	0.00000	0.1808(1)	1
Se2		0.1101(8)	0.00000	0.4495(1)	1

	0.1140(1)	0.00000	0.4549(1)	1
	0.1111(1)	0.00000	0.4541(1)	1
Se3	0.3377(1)	0.00000	0.3227(1)	1
	0.3426(1)	0.00000	0.3258(1)	1
	0.3435(1)	0.00000	0.3275(1)	1
Se4	0.6511(2)	0.00000	0.0567(1)	1
	0.6608(2)	0.00000	0.0619(1)	1
	0.6656(2)	0.00000	0.0651(1)	1

Table 5-4: Interatomic distances (Å) for selected $FeSb_{2-x}In_xSe_4$ samples.

Atom 1	Atom 2	x = 0.1	x = 0.2	x = 0.25
Se1	Sb2	2.708 (2)	2.716 (2)	2.659 (2)
Se1	Fe2	2.708 (2)	2.716 (2)	2.659 (2)
Se1	Sb3	2.645 (2)	2.671 (2)	2.659 (2)
Se1	Fe4	2.645 (2)	2.671 (2)	2.659 (2)
Se1	In2	2.708 (2)	2.716 (2)	2.659 (2)
Se1	In3	2.645 (2)	2.671 (2)	2.659 (2)
Se2	Sb1	2.719 (2)	2.659 (2)	2.674 (2)
Se2	Sb1	3.048 (2)	3.051 (2)	3.074 (2)
Se2	Fe1	2.719 (2)	2.659 (2)	2.674 (2)
Se2	Fe1	3.048 (2)	3.051 (2)	3.074 (2)
Se2	Fe3	2.737 (2)	2.725 (2)	2.710 (2)
Se2	In1	2.719 (2)	2.659 (2)	2.674 (2)
Se2	In1	3.048 (2)	3.051 (2)	3.074 (2)
Se3	Sb1	2.717 (2)	2.741 (2)	2.736 (2)
Se3	Fe1	2.717 (2)	2.741 (2)	2.736 (2)
Se3	Sb2	3.028 (2)	2.977 (2)	2.968 (2)
Se3	Fe2	3.028 (2)	2.977 (2)	2.968 (2)
Se3	Fe3	2.622 (2)	2.548 (2)	2.527 (2)
Se3	In1	2.717 (2)	2.741 (2)	2.736 (2)
Se3	In2	3.028 (2)	2.977 (2)	2.968 (2)
Se4	Sb2	2.773 (2)	2.788 (2)	2.840 (2)
Se4	Sb2	3.134 (2)	3.041 (2)	3.018 (2)
Se4	Fe2	2.773 (2)	2.788 (2)	2.840 (2)
Se4	Fe2	3.134 (2)	3.041 (2)	3.018 (2)
Se4	Sb3	2.669 (2)	2.750 (2)	2.795 (2)
Se4	Fe4	2.669 (2)	2.750 (2)	2.795 (2)
Se4	In2	2.773 (2)	2.788 (2)	2.840 (2)
Se4	In2	3.134 (2)	3.041 (2)	3.018 (2)
Se4	In3	2.669 (2)	2.750 (2)	2.795 (2)

5.3.2 Thermoelectric properties

Thermal diffusivity data on hot pressed pellets of the synthesized materials were measured in the temperature range from 300 to 650 K in order to assess the effect of Sb to In substitution on the thermal conductivity. The total thermal conductivity of the samples calculated from the diffusivity data using samples density and specific

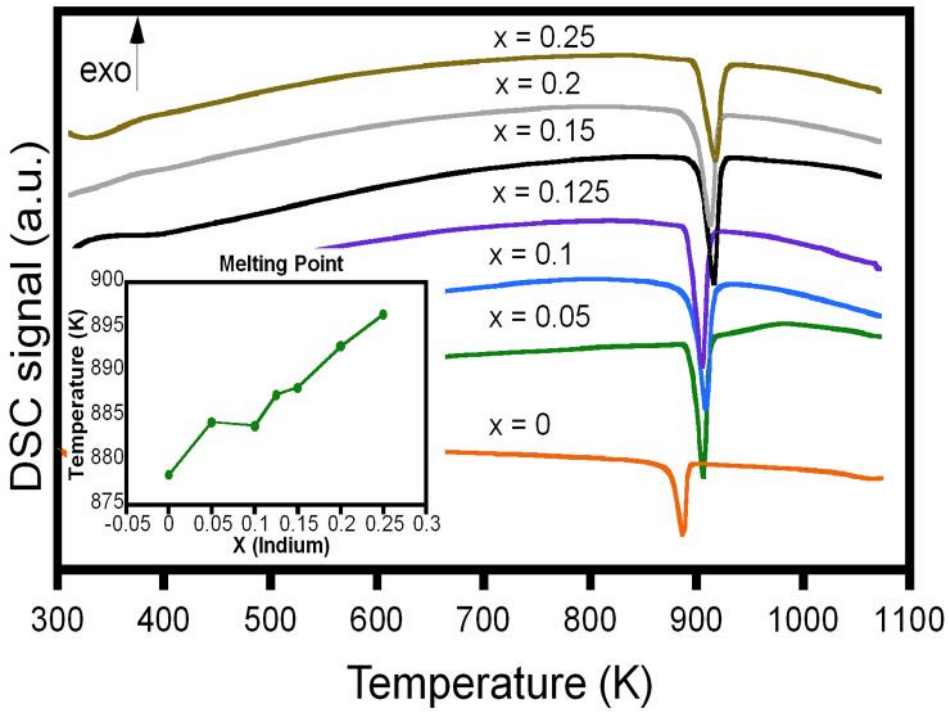

Figure 5-8: Differential scanning calorimetry spectrum of various $FeSb_{2-x}In_xSe_4$ samples upon heating showing a single thermal event for each composition. The melting point of the compounds increases with In content suggesting that In further stabilizes the crystal lattice.

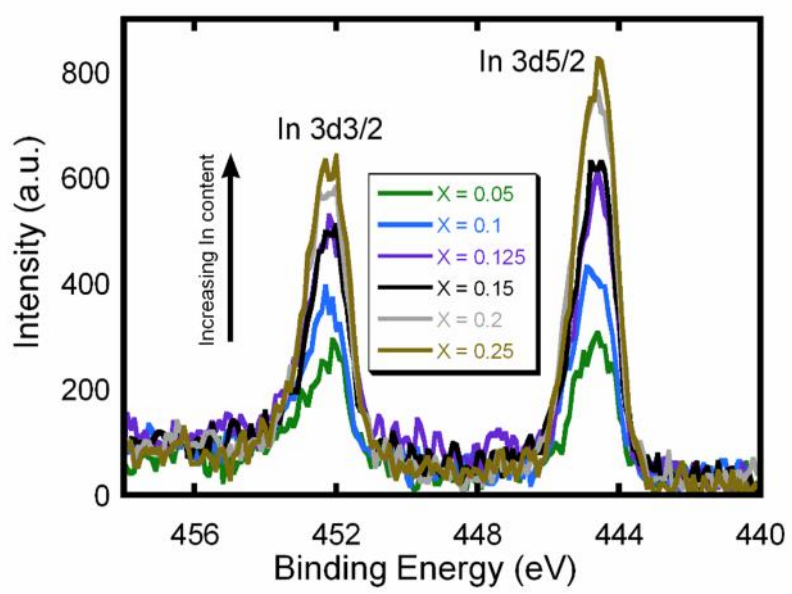

Figure 5-9: X-ray photoelectron spectra of various $FeSb_{2-x}In_xSe_4$ samples collected from a cold pressed pellet of the synthesized powder. It is clear that the In atoms reside in the +3 oxidation state, which suggests that they would sit at the Sb site within the crystal system.

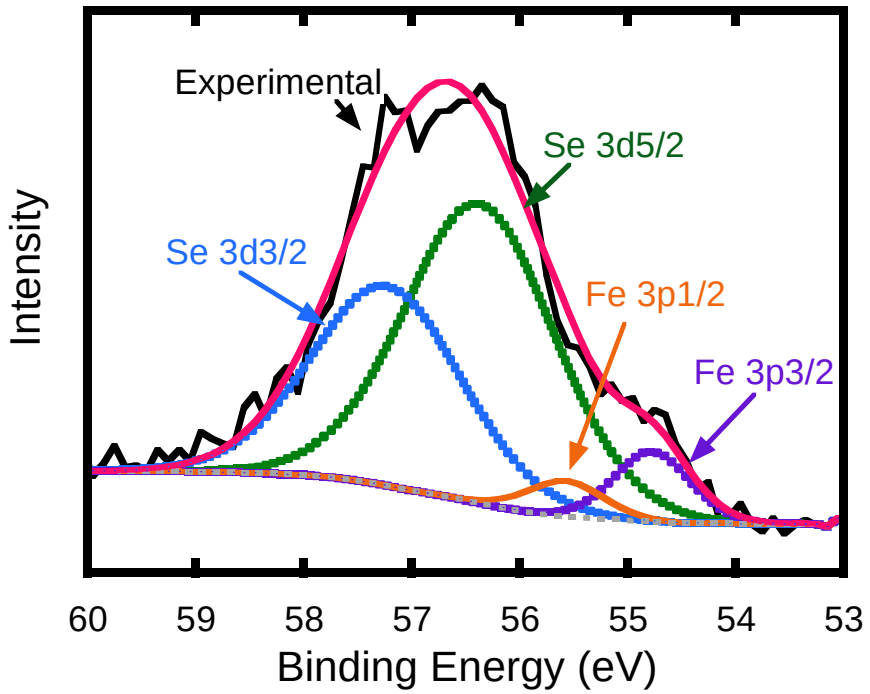

Figure 5-10: High resolution XPS spectrum of the $FeSb_{2-x}In_xSe_4$ sample with x = 0.25 showing Fe_3p peaks associated with Fe^{+2}.

heat is shown in Figure 5-11a. All samples showed very low total thermal conductivity values in the whole temperature range. The low values of the thermal conductivity originate from the complexity of the crystal structure as well as the heavy nature of the constituent atoms. At 300 K, the thermal conductivity decrease with increasing In content from ~0.45 $WK^{-1}m^{-1}$ for the sample with x = 0 to 0.25 $WK^{-1}m^{-1}$ for the samples with $x \geq 0.1$. The marginal drop in the thermal conductivity upon increasing the In content is not surprising given the small mass difference between In and Sb. The electronic contribution to the thermal conductivity was determined using the Wiedemann-Franz approximation $k_{electronic} = \sigma LT$, where σ is the electronic conductivity, T is the absolute temperature and L is the Lorenz number, taken as 2.44 X 10^{-8} $W\Omega K^{-2}$. As shown in Figure 5-12a, the electronic contribution to the overall thermal conductivity is extremely low with values ranging from 0.005 $WK^{-1}m^{-1}$ at 300 K for the sample with x = 0.25 to 0.04 $WK^{-1}m^{-1}$ for the sample with x = 0.125. This suggests that the total thermal conductivity is dominated by the lattice contribution.

Figure 5-11b shows the temperature dependence electrical conductivity of selected $FeSb_{2-x}In_xSe_4$ phases. At room temperature, the electrical conductivity of the sample with x = 0 is ~15 S/cm and remains nearly constant for samples with low In content $x \leq 0.1$. Surprisingly, further increase in In content ($x > 0.1$) resulted in a decrease in the electrical conductivity to ~5 S/cm. Regardless of the In content, the electrical conductivity increases with temperature suggesting semiconducting behavior. At 700 K, the electrical conductivity initially increase with In content, reaches a maximum at x = 0.1 and gradually decrease with further increase in In content. This sudden change in the trend of electrical conduction with increasing In content at the composition with x = 0.1 is consistent with the change in the distribution of In at various metal positions in the crystal structure. As observed from structure refinement, In exclusively occupies the metal atom

M1(*4i*) positions within layer A for compositions with x ≤ 0.1. Above this composition, In starts filling the M4(*2a*) and M2(*4i*) within layer B. This change in the distribution of In within the crystal lattice is presumably related to the alteration in the electrical conductivity trend for composition with x > 0.1. Further discussion of potential mechanism behind this change in the conducting behavior will be provided in the section discussing the magnetism of the samples. The observed alteration in the electrical conductivity upon isoelectronic substitution of Sb^{+3} by In^{3+} is surprising.

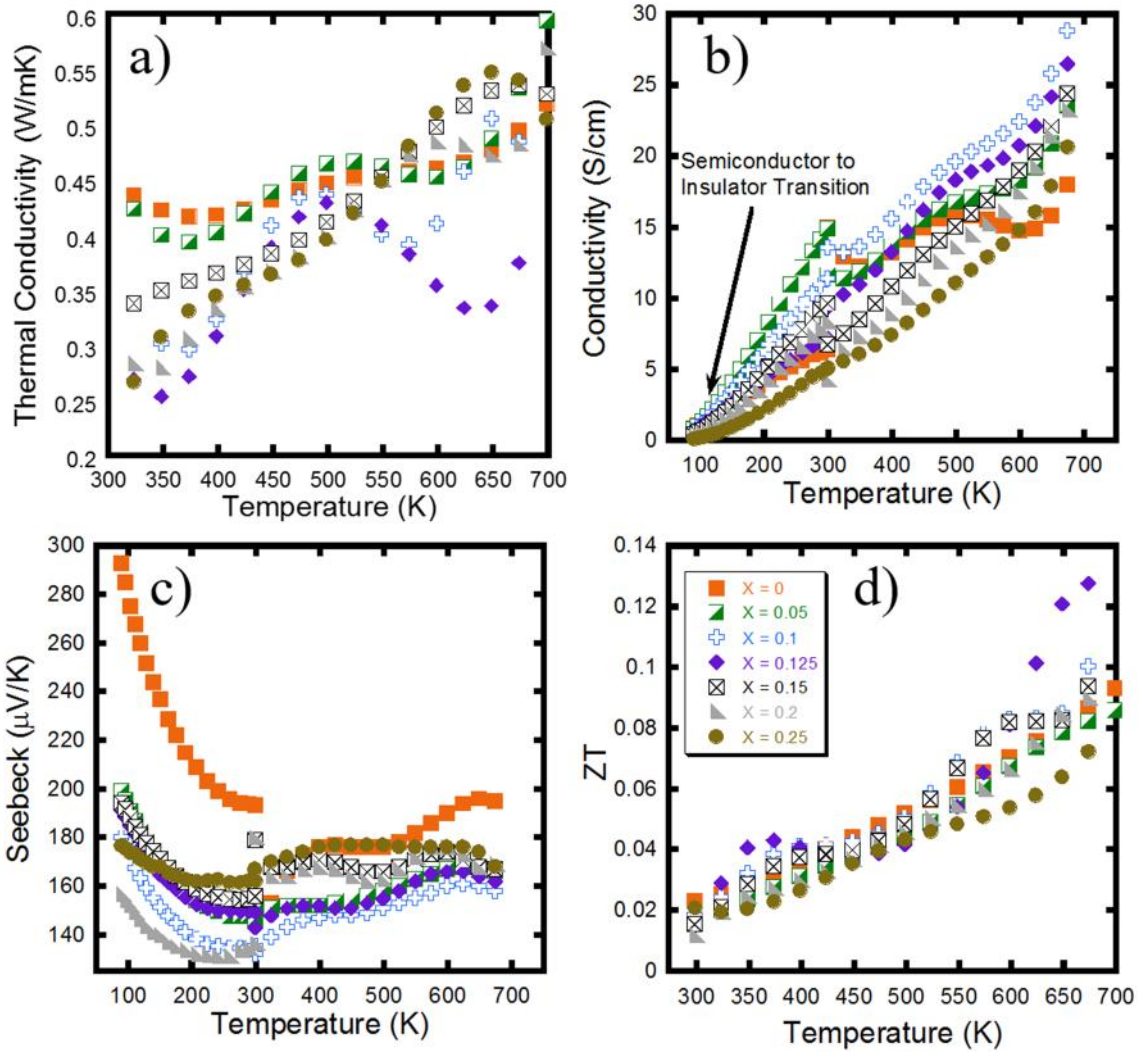

Figure 5-11: Temperature dependent thermoelectric properties of $FeSb_{2-x}In_xSe_4$ samples. a) Thermal conductivity, b) electrical conductivity, c) thermopower, d) thermoelectric figure of merit.

The initial small increase in the electrical conductivity with increasing In content ($x \leq 0.1$) suggests an increase in the carrier density, which is also consistent with the observed drop in the thermopower (Figure 5-11c). Therefore, one can speculate that the introduction of In^{3+} at the Sb^{3+} position slightly decreases the band gap enabling thermal excitation, at a given temperature, of a larger fraction of electrons from the valence band to impurity states within the band gap. These trends are also consistent for temperatures below 300 K, showing a transition from semiconductor-to-insulation for all samples near 130 K. There is a slight jump from low-temperature to high-temperature measurements for the x = 0.05 samples; however, that is likely due to inconsistencies between the two measurement systems.

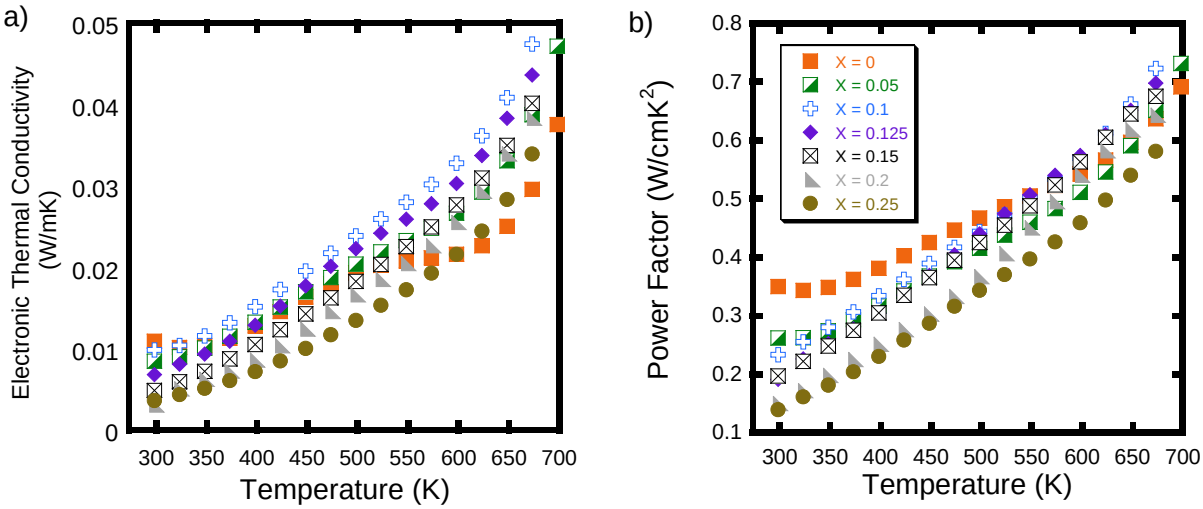

Figure 5-12: a) The electronic contribution to thermal conductivity of $FeSb_{2-x}In_xSe_4$ samples, calculated using the Wiedemann-Franz law and a Lorenz number of 2.44 X 10^{-8} $W\Omega K^{-2}$. b) The power factor (PF) of $FeSb_{2-x}In_xSe_4$ samples. Samples with x = 0.05, 0.1 and 0.125 exhibit higher PF than that of the undoped $FeSb_2Se_4$ due to increases in electronic conductivity coupled with a slight decrease in thermopower.

Figure 5-11c shows the temperature dependence thermopower data of various samples. All samples exhibit positive thermopower values indicating p-type semiconducting behavior. Interestingly, changes in the thermopower of various $FeSb_{2-x}In_xSe_4$ phases were found to be strongly correlated to the distribution of In atoms within the crystal structure. For samples

containing low In content ($x \leq 0.1$), the thermopower decrease with increasing In content from ~150 μWK-1 for samples with x = 0.05 to 130 μVK-1 for the sample with x = 0.1. In atoms in these samples are preferentially located within the M1(*4i*) site of layer A. For compositions with higher In content where In atoms are also found in M4(*2a*) and M2(*4i*) sites of layer B, the thermopower gradually increase with increasing In content. This trend is consistent with the observed alteration in the electrical conductivity further confirming a surprising drop in the effective carrier density in samples with large In content ($x>0.1$). This trend is also consistent at temperatures lower than 300 K with the exception of x = 0.2 that exhibits a sharp dip at 300 K, likely due to inconsistencies between the two measurement schemes. As the temperature approaches 130K the thermopower of all samples increases, indicating insulating behavior. Regardless of the composition, the thermopower steadily from 300 – 400 K, indicating that intrinsic carriers are produced as holes as temperature increases. From 400 – 500 K the thermopower for each material also either decreases in magnitude or remains relatively steady. It is important to note that Djieutedjeu et al. determined that the Curie temperature of $FeSb_2Se_4$ is 450 K.[187] Therefore, we reason that at the Curie temperature carriers that are localized due to bound magnetic polarons are liberated near 450 K, suddenly increasing the overall carrier concentration of the system. This follows the assumed trend that as carrier concentration is increased by In doping in the A-layer until saturation the Seebeck coefficient is reduced. After the Curie temperature is reached and carriers are no longer localized due to BMPs, the Seebeck coefficient again begins to rise due to reduced carrier mobility from increased scattering with phonons. At temperatures higher than 600 K the Seebeck coefficient again decreases, likely due to bipolar conduction, consistent with doped-semiconductor behavior. The electronic band gap of the

samples where estimated using the Goldsmid-Sharp equation, Equation 5-1,where T_{max} is the temperature of maximum thermopower, S_{max}.[188]

$$\textit{Equation 5-1: } E_g = 2eT_{max}S_{max}$$

The calculated band gaps are 0.245 eV (x = 0), 0.210 eV (x = 0.05), 0.200 eV (x = 0.1) and 0.199 eV (x = 0.15), suggesting a small contraction of the band gap upon In substitution at Sb sites in the structure of $FeSb_2Se_4$. Djieutedjeu et al. determined that the introduction of Sn at Fe sites resulted in an electronic structure that was dominated by an increase in the electron density in the impurity band evidenced by the switch of the thermopower from p-type to n-type with increasing Sn content; however, that does not appear to be the case with the substitution of In for Sb as the thermopower maintains a p-type nature.[187] Instead, it appears that the substation of In for Sb results in an increase in the density of states near the Fermi level, resulting in a slight reduction of the band gap.

The power factor and *ZT* for the series of samples are plotted in Figure 5-12b and Figure 5-11d, respectively. At 300 K, the largest power factor (PF) value is observed for the pristine compound and a gradual decrease in the PF is observed upon increasing In content from 0.05 to x = 0.25. Regardless of the composition, the PF of In substituted samples, rapidly increase with temperature and compositions with x ranging from 0.05 to 0.15 outperform the pristine sample (x = 0) at $T \geq 500$ K. This behavior is consistent with the observed strong temperature dependence of the thermopower and electrical resistivity of various $FeSb_{2-x}In_xSe_4$ phases. At 300 K, the substitution of Sb by In in $FeSb_{2-x}In_xSe_4$ phases only result in a marginal change in the *ZT* values. However, *ZT* values for samples with x ranging from 0.05 to 0.15 drastically increase with temperature, reaching values as high as 0.13 at 650 K for the composition with x = 0.125.

5.3.3 Magnetic properties

To investigate the effect of the distribution of In atoms at various metal positions on the magnetic behavior of $FeSb_{2-x}In_xSe_4$ phases, the magnetic susceptibility of selected samples were measured under field cooled (FC) and zero field cooled (ZFC) conditions from 2 – 300 K using a SQUID magnetometer. As shown in Figure 5-13, all $FeSb_{2-x}In_xSe_4$ phases exhibit, over the whole temperature range, a ferromagnetic-like behavior similar to the one observed in the pristine unsubstituted composition (x = 0). Regardless of the In content, the FC susceptibility slowly increases with decreasing temperature to the characteristic magnetic transition near 130 K, at which a spontaneous drop in susceptibility similar to the one reported in the unsubstituted composition is apparent.[182] Similar magnetic transition at 130 K is also observed on the ZFC magnetic susceptibility of $FeSb_{2-x}In_xSe_4$ samples (Figure 5-13). The observed similarity in the magnetic behavior of $FeSb_{2-x}In_xSe_4$ phases is consistent with the similarity in the distribution of Fe atoms at various metal positions in samples. Surprisingly, the magnitude of the ZFC and FC magnetic susceptibility strongly depend on both the concentration and distribution of In atoms in the crystal structure. For both FC and ZFC measurements, the magnitude of the magnetic susceptibility increases with increasing In content up to $x \leq 0.1$. Further increase of In content ($x > 0.1$) resulted in a gradual drop in the magnitude of the magnetic susceptibility. As can be seen from the structural data obtained from Rietveld refinements of powder diffractograms, the substitution of Sb by In only have marginal effect on the crystal structure. For example, the Fe(3) - Se(2) - Fe(3) bond angle within the magnetic chain in layer A, which is believed to be responsible for the ferromagnetism in $FeSb_2Se_4$, only increase by 0.4 º upon increasing the In content from x = 0 to x = 0.25. This suggests that the observed changes in the magnetic behavior cannot be explained using subtle structural distortions that may arise from the substitution of Sb by In atoms. While it is expected that an increase in carrier concentration could increase the magnitude of the

magnetic susceptibility of various samples, this trend appears to only occur for compositions with $x \leq 0.1$. The drop in the magnetic susceptibility for samples with $x > 0.1$ is contradictory to the anticipated behavior and suggests a surprising drop in the overall carrier concentration. A plausible mechanism responsible for the observed magnetic behavior is discussed in the following section.

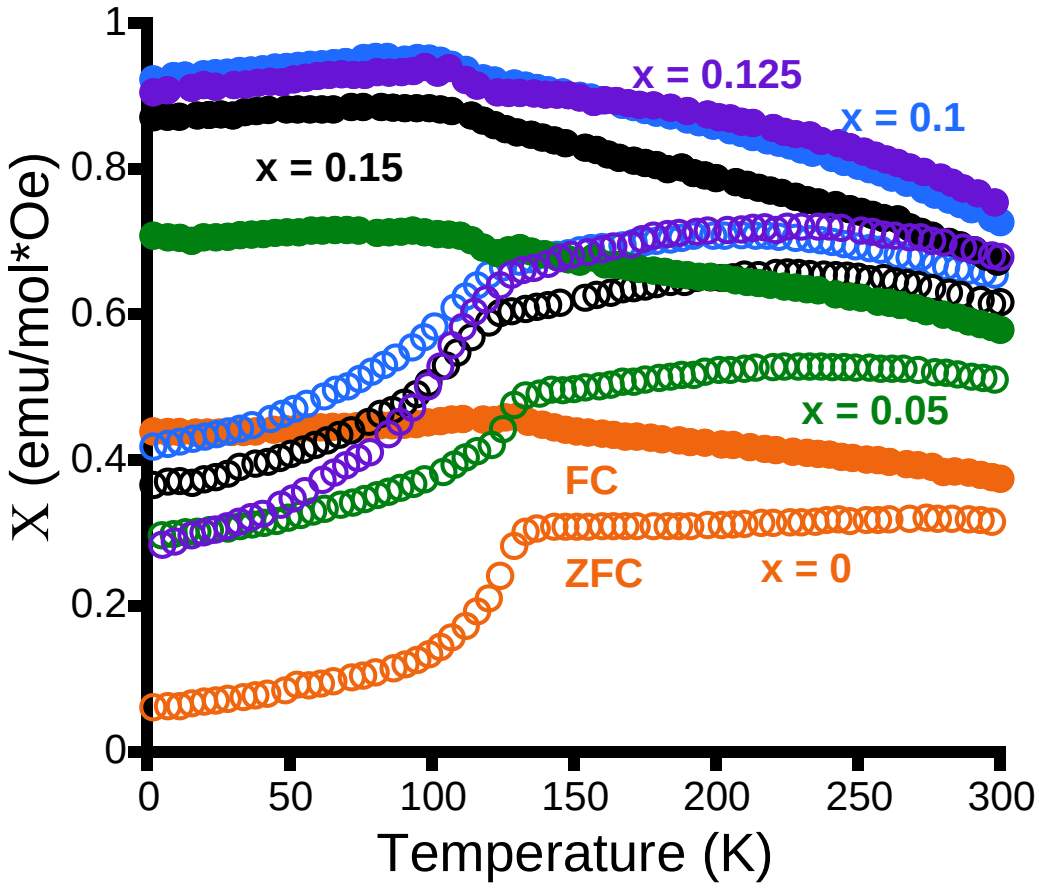

Figure 5-13: Tempereture dependent magnetic susceptibility curves of $FeSb_{2-x}In_xSe_4$ showing magnetic transition near 130 K under both zero field cooled (ZFC, open circles) and field cooled (FC, filled circles) conditions.

To further explore the ferromagnetic-like behavior of $FeSb_{2-x}In_xSe_4$ phases, isothermal magnetization curves of selected samples at 2K, 150K, and 300K, were also gathered via SQUID magnetometer. As shown in Figure 5-14, all samples exhibit ferromagnetic-like behavior given the snake-like shape of the hysteresis curves of various samples at temperatures before and after

the transition temperature of 130K. The coercivity for all samples decreases with increasing temperature, ranging from 1117 – 2250 Oe at 2 K to 180 – 295 Oe at 300K. It is suspected that the decrease in coercivity with increasing temperature is due to thermal spin fluctuations dominating the effect of magnetic coupling between the spin of free carriers and localized magnetic moments. Interestingly, the coercivity decreases with In content for samples with $x \leq 0.1$, then sharply increases with additional In content for samples with $x > 0.1$. This surprising trend is also probably related to the change in the distribution of In atoms at various metal positions within the structure. Even at high applied field the magnetization curves only approach saturation, but do not flatten entirely. This effect can be explained by the existence of free carriers present in the system at high applied fields, carriers that are not localized due to bound magnetic polarons (BMPs).

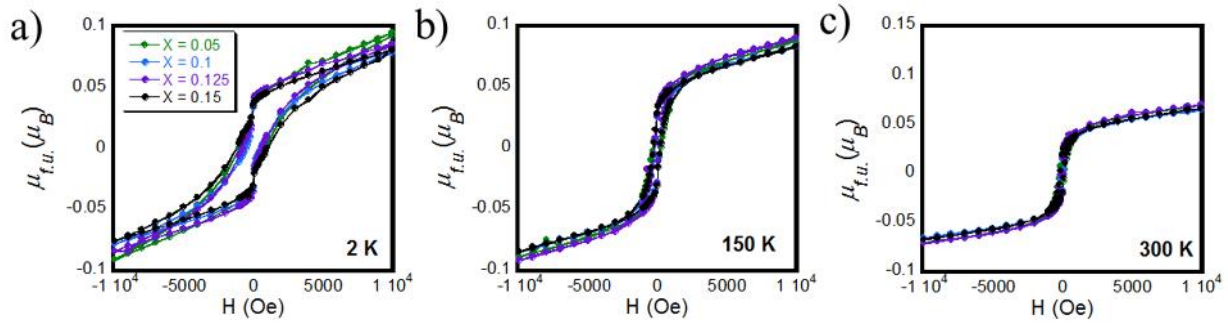

Figure 5-14: Isothermal magnetization curves of $FeSb_{2-x}In_xSe_4$ samples at 2K, 150K and 300K showing ferromagnetic behavior in all samples.

5.3.4 Structure-property relationship

The observed surprising drastic reversal in the trend of the variation of magnetic susceptibility, magnetization and electronic properties with In content can be correlated to the distribution of In atoms at various metal positions in the structure of $FeSb_{2-x}In_xSe_4$ samples. As discussed above, the substitution of Sb by In induces a marginal increase in the carrier density, presumably due to a local alteration of the electronic structure at the vicinity of the Fermi level. Spins of these additional carriers interact with localized spins on Fe^{2+} ions to form localized bound

magnetic polarons (BMPs).[183] The size of such BMPs increases with increasing carrier density (hence increasing In content) around the magnetic centers leading to overlapping of neighboring BMPs and a collective ferromagnetic ordering of localized moments (Figure 5-15). For samples with $x \leq 0.1$, In atoms exclusive substitute Sb atoms at M1(*4i*) site within layer A. Evidence of the removal of the stereoactive lone pair of Sb^{3+} 5s2 electrons is supported by the reduction in the angle β with increasing In content, which is the cause for the increase in carrier concentration. The dominant carrier in each of these systems is holes, hence the p-type behavior of the thermopower. As such, the removal of the localized lone pair of electrons harnessed by the BMPs contributes to an increase in hole carrier density. This reasoning is consistent with the supposition that BMPs are focused at Fe centers, which reside with higher occupancy in the A layer than the B layer, such that when In resides in the A layer the electronic conductivity is increased, and that when In resides in the B layer a competing effect is realized. This implies that the local change in the carrier density exclusively increases the size of BMPs within layer A in these samples (Figure 5-15a) leading to the observed increase in the magnitude of the magnetic susceptibility with increasing In content. However, metal positions in both layer A and layer B are affected by the substitution of Sb by In in samples with $x > 0.1$. Therefore, the local coupling of charge carriers spins and localized spins on magnetic centers (Fe^{2+}) results in an increase in the size of BMPs in both layers. While BMPs within individual layer overlap to induce intra-layer ferromagnetic ordering of localized magnetic moments, the surprising decrease in the overall magnetic susceptibility for samples with $x > 0.1$ suggests that BMPs in adjacent layers A and B are coupled anti-ferromagnetically (Figure 5-15b). The overall magnetic moment from layer A is larger than the magnetic moment from layer B given the higher concentration of Fe atoms within layer A, which explains the net ferromagnetic-like (or ferrimagnetic) behavior of $FeSb_{2-x}In_xSe_4$ samples. Upon increasing the concentration of In atoms

above x > 0.1, the magnitude of the magnetic moment from layer B increases leading to the observed drop in the overall magnetic susceptibility.

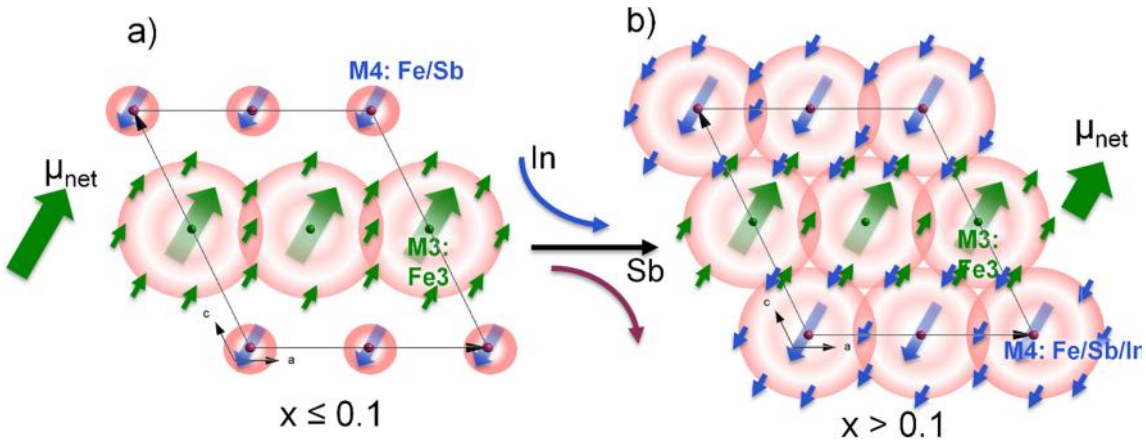

Figure 5-15: Schematic of the mechanism of magnetic coupling in FeSb2-xInxSe4 samples. a) For x ≤ 0.1 the bound magnetic polarons (BMPs) centered at the M3(2d) site dominate and are strengthened by the increased carrier concentration due to In insertion within the layer A, increasing the electronic conductivity and magnetic saturation. b) For values of x > 0.1 the In saturates layer A and begins to fill the layer B, causing localized scattering of carrier due to anti-ferromagnetically oriented overlapping BMPs.

The above described anti-ferromagnetic coupling mechanism between layer A and layer B also explains the observed surprising reversal of the effect of Sb to In substitution on the electronic properties of $FeSb_{2-x}In_xSe_4$ samples for x > 0.1. For samples with low In content (x ≤ 0.1), it was found that the electrical conductivity slightly increases with In content while the thermopower decrease, which is consistent with a local increase in the carrier density due to Sb to In substitution at the M1(*4i*) site within layer A. These additional carriers are ferromagnetically coupled to localized magnetic moments of Fe^{2+} ions leading to minimal scattering. In samples with x > 0.1, In atoms also occupy the M2(*4i*) and M4(*2a*) sites within layer B in addition to the M1(*4i*) site within layer A. While the local interaction between the added carriers and the magnetic centers within individual layers is ferromagnetic, the observed drop in the electrical conductivity and increase in the thermopower of samples with x > 0.1 suggest a decrease in the overall carrier density in the samples. This behavior in the electronic transport data is due to an increase scattering

of charge carriers due to the antiferromagnetic interactions of charge carriers spins at the interfaces between BMPs from adjacent layers A and B. The fraction of charge carriers involve in such anti-ferromagnetic scattering increases with increasing In content within layer B ($x > 0.1$), which is consistent with the observed trend in the electrical conductivity and thermopower data of samples with high In content ($x>0.1$).

There are two pieces of evidence for the existence of BMPs within the $FeSb_{2-x}In_xSe_4$ system and their effect on the overall magnetic and electronic properties. First, as shown through the analysis of the powder diffractograms of the samples, while there is no significant structural change to the system, nor is there a change to the concentration or distribution of magnetic atoms within the system, given that Fe is the only magnetic center present, there is a change to the magnetic and electronic transport properties when the Sb $5s^2$ lone pair of electrons is removed through the substitution of In. As this substitution essentially removes electrons from the p-type system, it is reasoned, as detailed above, that only the electronic structure of the system is changed by increasing the carrier concentration. Hence, the increase in magnetic susceptibility and coercivity of the system that corresponds with an increase in carrier concentration can only be due to the existence of BMPs in the absence of the introduction of new magnetic atoms or a significant structural change in the magnetic exchange interactions. Thus, the observed change in magnetism in the In doped samples validates the existence of BMPs in all $FeSb_{2-x}In_xSe_4$ samples, including the parent structure.

To further probe the existence of BMPs and the effect of In concentration on their strength and interaction the isothermal magnetization curves for each sample were fit with the Langevin function, Equation 5-2.[189]

Equation 5-2: $$M = M_0 L(x) + \chi_m * H$$

In this equation the Langevin term, $L(x) = \coth(x) - {}^{1}/_{\chi} = m_{eff} H k_B T$, multiplied with $M_0 = N m_s$ models the contribution of the BMPs to the total magnetization of the system. Here, χ_m is the susceptibility of the matrix, H is the applied field, m_{eff} is the effective spontaneous moment per BMP, k_B is the Boltzmann constant, T is the absolute temperature, N is the concentration of BMPs in the system, and m_s is the true spontaneous moment of the BMP. In order to analyze isothermal magnetization data with a simple procedure, the assumption that $m_s = m_{eff}$ is imposed in the high temperature regime, which is taken as above the insulator-to-semiconductor transition of 130K; however, using this scheme fit the data well to 50 K, an example of which is shown in Figure 5-16. In this fitting M_0, m_{eff}, and χ_m are taken as the dependent fitting parameters, which are plotted in Figure 5-17 along with N. As expected, the contribution to the magnetic moment of the system from the matrix, χ_m, is similar for all compositions of In doping, Figure 5-17b. The contribution from BMPs, M_0, shows relatively little difference with respect to In content, with x = 0.1 yielding the lowest magnitude and x = 0.2 the highest, Figure 5-17a. Still, there is little difference between these values, which can be expected as the difference in magnetic susceptibility saturation is similar for the doped samples. Of most interest is m_{eff}, which shows a distinct trend relatable to previous trends shown in the electronic conductivity, magnetic coercivity, and magnetic susceptibility, Figure 5-17c. As In content increases from x = 0.05 to 0.1 m_{eff} increases, indicating that the effective strength of the individual BMPs increases correlated to increasing carrier concentration due to increasing In content in the A layer. As In begins to occupy the B layer at x > 0.1, antiferromagnetically coupled to the A layer, m_{eff} decreases, indicating that the A layer and B layer BMPs compete, reducing the strength of each individual BMP. The consistency of the correlation of In content and carrier concentration to BMP true

spontaneous moment validates the assumption that the simple Langevin model accurately describes this magnetic system in which BMPs are present.

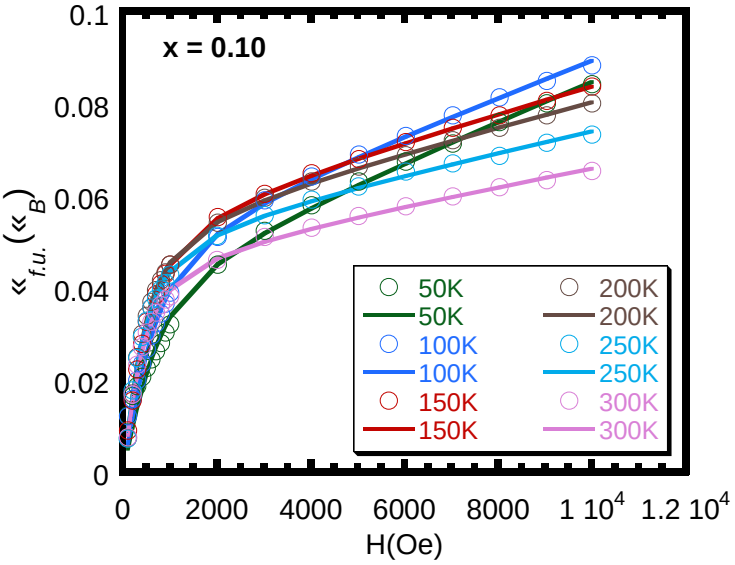

Figure 5-16: Langevin fitting of x = 0.1 sample for temperature range 50 – 300 K.

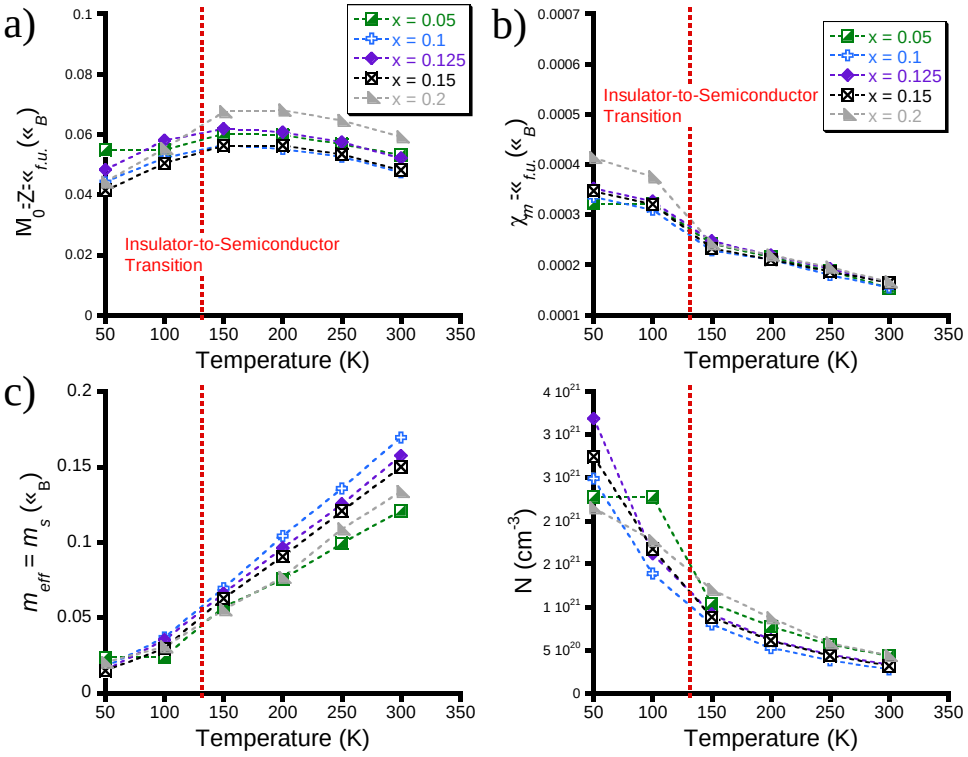

Figure 5-17: a) Temperature dependence of contribution to magnetization of system by BMPs, b) magnetic susceptibility of the matrix, c) the effective spontaneous moment of modeled BMPs and, d) concentration of BMPs in the system.

5.3.5 Conclusion

In summary, we have investigated the effect of Sb to In substitution on the electronic and magnetic properties of the $FeSb_{2-x}In_xSe_4$ solid-solution series. Although the $FeSb_{2-x}In_xSe_4$ series are isostructural, we observed that the electronic and magnetic behavior of various samples strongly depend on the distribution of In atoms at various metal positions in the crystal structure, which in turn is correlated to level of Sb to In substitution (x value). In the crystal structure of $FeSb_2Se_4$ (x = 0), Sb atoms are mixed with Fe at the M1(*4i*), M2(*4i*) and M4(*2a*) sites. We found that in compositions with low In content ($x \leq 0.1$), In atoms preferentially substitute Sb atoms at M1(*4i*) site within layer A. Further increase of In content results in the substitution of Sb atoms at M4(*2a*) and M2(*4i*) sites within layer B. A consequence of this preferential distribution of In atoms in the crystal structure is a drastic alteration of the electronic and magnetic behavior of $FeSb_{2-x}In_xSe_4$ samples with In content. It appears that a local substitution of Sb by In exclusively at M1(*4i*) within layer A increases the electrical conductivity and magnetic susceptibility on the samples. However, a gradual degradation of the electrical conductivity and magnetic susceptibility is observed when In atoms also substitute Sb at M2(*4i*) and M4(*2a*) sites within layer B. This drastic change in the electronic and magnetic behavior of $FeSb_{2-x}In_xSe_4$ samples with large In content ($x > 0.1$) is attributed to a drop in the carrier density presumably due to anti-ferromagnetic scattering of charge carriers at the interfaces between BMPs from adjacent layers A and B.

CHAPTER 6

THERMOELECTRIC AND OPTICAL PROPERTIES OF NEW NEEDLELIKE $Sr_{1-x}Sb_xHfSe_3$ (x = 0, 0.005, 0.01) AND PEROVSKITE $BaHfSe_3$ MATERIALS

6.1 Introduction

Ternary transition metal based chalcogenide materials have garnered a great deal of attention within the fundamental materials community as they have the potential to offer advanced and unique thermal,[190,191] electronic,[192,193] and magnetic transport properties[194-197] coupled with interesting optical response.[161,198-201] Their wide range in crystal structure and chemical composition allows for creative systematic engineering that has produced some of the most well-known photovoltaic and thermoelectric materials such as $CuInSe_2$[202-205] and CuAgSe.[123,140,206,207] The flexibility and ease at which these materials have been synthesized spurs the need to investigate new chalcogenide-based crystal structures, potentially offering novel properties and transport mechanisms and adding to the general understanding of how to engineer these materials to power our future.

Perovskite structured ternary transition metal chalcogenide materials have been notably absent from recent literature concerning this important material family. The perovskite structure, named for Russian mineralogist Lev Perovski, is based on the prototype crystal of $CaTiO_3$, formula $^{XII}A^{2+VI}B^{4+}X^{2-}{}_3$, forming in the orthorhombic *Pnma* symmetry. In the idealized cubic system, the

A cation is stationed at Wyckoff position *4a* (0, 0, 0), while B cations populate the body-center *4a* site (½, ½, ½). Many variations of this structure have been researched, most commonly the distorted orthorhombic, tetragonal, and hexagonal perovskite versions.[208-212] These relatively dense structures have offered various interesting physical properties such as superconductivity,[213,214] colossal magnetoresistance,[215,216] ultra-low thermal conductivity,[217] high-dielectric constant,[218,219] and high optical absorption coefficients.[220-223] These unique properties have led to the application of inorganic perovskite materials in photovoltaic solar cells, thermoelectric devices,[224,225] and even inorganic-organic memory devices,[226,227] often taking advantage of the specific electronic transport properties the high symmetry structure offers as well as high temperature stability.

Typically, these structures require significantly high temperatures and pressures for stable formation. Consequently, this has led to a focus on the production of oxides, which has deterred the creation and elucidation of chalcogenide-based perovskites. To date, of the chalcogenide based perovskites only sulfide-based compounds have been studied, specifically $EuZrS_3$,[228] $EuHfS_3$,[228] $CaZrS_3$,[229] $BaZrS_3$,[230,231] and $BaHfS_3$,[229] but the electronic and thermal properties of these compounds have not been extensively characterized. Recently, Sun *et al*. published the promising results of a theoretical study on a series of ABX_3 compounds with A = Ca, Sr, and Ba, B = Ti, Zr, and Hf, and X = S and Se, predicting the photovoltaic behavior of the distorted perovskite, needlelike, and hexagonal phases.[232] The results of this research predicted that the distorted perovskite phase of $ABSe_3$ where A = Ba, Ca, Sr and B = Hf and Zr exhibit band gaps between 1.3 – 1.7 eV, indicate the production of high efficiency photovoltaic devices. Further, the needle-like phases were predicted to exhibit band gaps of 0.75 – 1.0 eV, which can be quite useful for thermoelectric applications. More recently, Meng et al. calculated the electrical and optical

properties of $BaZrS_3$ from first-principle DFT calculations and were able to determine that $BaZr_{0.9}Ti_{0.1}S_3$ would exhibit a band gap of 1.46 eV, ideal for single- or multi-junction solar cells and predicted to deliver >20% photovoltaic conversion efficiency.[233] Though synthesis was challenging, they were also able to create perovskite $BaZrS_3$ and confirm that the band gap matched that of the calculations, 1.85 eV. To date, only the needle-like phases of $SrZrSe_3$ and $Ba_xSr_{1-x}ZrSe_3$ have been reported, with few if any physical measurements.[234] $BaZrSe_3$ has also been produced, but forms non-stoichiometrically in the hexagonal structure.[234]

Hence, the purpose of the research presented here is the development of the needle-like (orthorhombic) and distorted perovskite structures of $SrHfSe_3$ and $BaHfSe_3$ using both solid-state and mechanical alloying methods, and the physical property characterization and analysis of each material with respect to thermoelectric and optical behavior. Substitutional doping of Sb for Sr in $SrHfSe_3$ is also investigated in order to probe the effects on the electronic and thermal transport properties as well as the optical band gap.

6.2 Experimental

6.2.1 Synthesis and processing

This study focuses on the creation of a series of perovskite materials of the type $ABSe_3$ where A = Ca, Ba, or Sr and B = Zr or Hf. The only previously known structure of this group is $SrZrSe_3$, which was successfully synthesized as phase pure by Tranchitella et al. in 1997; however, the structure obtained was in fact needlelike rather than distorted perovskite,[234] and $BaZrSe_3$, synthesized in 1964 by Aslanov, adopted the hexagonal $CsNiCl_3$ structure (space group *P63/mmc* #194).[235] Tranchitella's approach to the creation of selenide based perovskites of the $GdFeO_3$ structure type is notable in that low-pressure synthesis techniques were employed. This work

follows a similar approach while incorporating mechanical alloying (high energy ball-milling) to produce a novel series of $ABSe_3$ materials, maintaining an approach that requires less instrumental sophistication than typical perovskite synthesis at high temperature (>1273 K) and pressure (>1 GPa).

Two approaches were taken to synthesize $ABSe_3$ where A = Ca, Ba, or Sr and B = Zr or Hf: *Synthesis Technique 1*) mixing of powder and granular reactants by 30 minutes of high energy ball-milling followed by solid state reaction at 1073 K, and *Synthesis Technique 2*) high energy ball-milling of the reactants for 100 hours.

Synthesis Technique 1: Stoichiometric amounts of Ba beads (Sigma Aldrich, 99% 0.5 – 2.0 mm), Ca granules (Alfa-Aesar, 99.5% -16mesh), Sr granules (Alfa-Aesar, 99% 19mm), Hf powder (American Elements, 99.5%), Zr powder (American Elements, 99%), Sb powder (99%, Alfa Aesar), and Se powder (99.5%, Sigma Aldrich) were weighed in a glovebox under Ar atmosphere and added to hardened steel jars with hardened steel ball bearings and sealed. The contents were processed for 30 minutes in order to ensure mixing of the reactants. The jars were then transferred to the glovebox and the contents were placed in a graphite crucible with lid (dia. 7 mm x 55 mm) and placed inside a silica tube which was flame sealed. The tube was then heated to 1073 K in 24 hours, held for 120 hours, then cooled to room temperature in 24 hours. This process was successful in creating >98% phase pure $SrHfSe_3$ and Sb-doped $SrHfSe_3$ by analysis of X-ray diffraction (XRD) data; however, Ba and Ca compounds were not successfully created with this method. Further processing of Ba and Ca compounds by cold-pressing the products of the first reaction at ~300 MPa into 13 mm diameter discs and reheating the pellets at 1073 K and 1173 K for an additional 120 hours did not complete the reaction. Binary compounds such as CaSe and BaSe constituted a majority of the products.

Synthesis Technique 2: Stoichiometric amounts of each reactant were added to hardened steel jars in a glovebox under Ar atmosphere as before. Milling proceeds for 100 hours at room temperature. Jars were then transferred to the glovebox to extract the contents. It is important to note that the risk of contamination from Fe during such intense milling is significant, and that it is typical to find Fe contamination of ~10 wt. % for 100 hours of milling.[191] X-ray fluorescence and X-ray diffraction methods were used to determine the level of contamination for each sample. The milled products were then hot-pressed in a graphite die at 1173 K and 100 MPa for 1 hour, with a ramp rate of 225 K/hr. This technique was successful in producing >85% pure $BaHfSe_3$ and >95% pure $SrHfSe_3$, yet, was unsuccessful in producing any other phase pure Ca or Zr compound.

Single Crystal Synthesis: Single crystals of $SrHfSe_3$ were successfully grown by annealing $SrHfSe_3$ produced using synthesis technique 1. Approximately 0.25 g of $SrHfSe_3$ was added to a 7 mm diameter x 12-inch-long silica tube and flame sealed with residual pressure of 10^{-4} Torr. The tube was heated to 1373 K in 24 hours and held for 240 hours, then cooled to room temperature in 24 hours. A lustrous black crystal was harvested from the products. Attempts to produce single crystals of $BaHfSe_3$ and other compounds failed, but did consistently create crystals which were too small for characterization by X-ray diffraction methods.

Densification: Samples of phase pure powder $SrHfSe_3$, Sb-doped $SrHfSe_3$ and $BaHfSe_3$ were formed into pellets using the hot-press method. Approximately 1 g of sample powder were added to a 10 mm diameter graphite die and pressed between graphite anvils. Densification of pellets was conducted under flowing Ar gas at 40 ml/min, a pressing temperature of 1123 K for 2 hours and an applied pressure of 100 MPa with a ramp up and down rate of 225 K/hour. Pellets were then removed from the graphite dies and polished to a mirror finish with metallographic paper, up to 1200 grit. All $Sr_{1-x}Sb_xHfSe_3$ pellets yielded both a geometric and true density that was

greater than 97% of the theoretical density. The density of the $BaHfSe_3$ pellet was 6.9 g/cm^3 which is only 56% of the calculated theoretical density of cubic $BaHfSe_3$ with *Pm-3m* (#221) symmetry, whereas it is 130% of the calculated theoretical density of $BaHfSe_3$ with tetragonal *P42mc* (#105) symmetry.

6.2.2 Characterization.

Optical band gap measurements: A Varian Cary 5000 spectrometer, equipped with a Harrick Praying Mantis diffuse reflectance accessory, was used to collect the optical diffuse reflectance spectra of the compounds over the ultraviolet, visible, and near infrared spectral regions (UV/VIS/NIR). Each sample was ground and placed in a sample holder to a depth of 3 mm. Barium sulfate (Fisher, 99.92%) was used as a 100% reflectance standard. The measurement was conducted at a scan rate of 600 nm/min. The optical bandgaps of the samples were estimated from the UV/VIS/NIR spectra by extrapolation of the absorption edge to the baseline. The absorption spectra were calculated from the reflectance spectra via the Kubelka−Munk equation.[236] The direct allowed transmission model was used to fit each set of data in order to produce Tauc plots to estimate the optical band gap.

6.3 Results and Discussion

6.3.1 Synthesis and Crystal structure of Needle-like $SrHfSe_3$.

Synthesis technique 1 produced a fine black powder that yielded an X-ray diffraction pattern dissimilar to the prototypical $GdFeO_3$ perovskite structure, but strikingly similar to that of

needle-like $SrZrSe_3$, indicating an orthorhombic structure with space group *Pnma* (#12), void of extraneous peaks, as shown in Figure 6-1. This is in agreement with the calculated Goldschmidt tolerance factor of $t = 0.82$, where $t = (r_A + r_0)/\sqrt{2}\,(r_B + r_0)$ and r_A is the ionic radius of the A-cation (Sr), r_B is the ionic radius of the B-cation (Hf), and r_0 is the ionic radius of the anion (Se).[237] WDXRF characterization of the synthesized powder shows a composition of $Sr_{1.16}Hf_{0.90}Se_3$, slightly Sr-rich with Fe contamination of less than 0.1 wt. %. This phase structure remained consistent through hot pressing, signaling that the synthesized compound is single phase. Sb-doped samples of $SrHfSe_3$ produced using synthesis technique 1 yielded similar diffraction

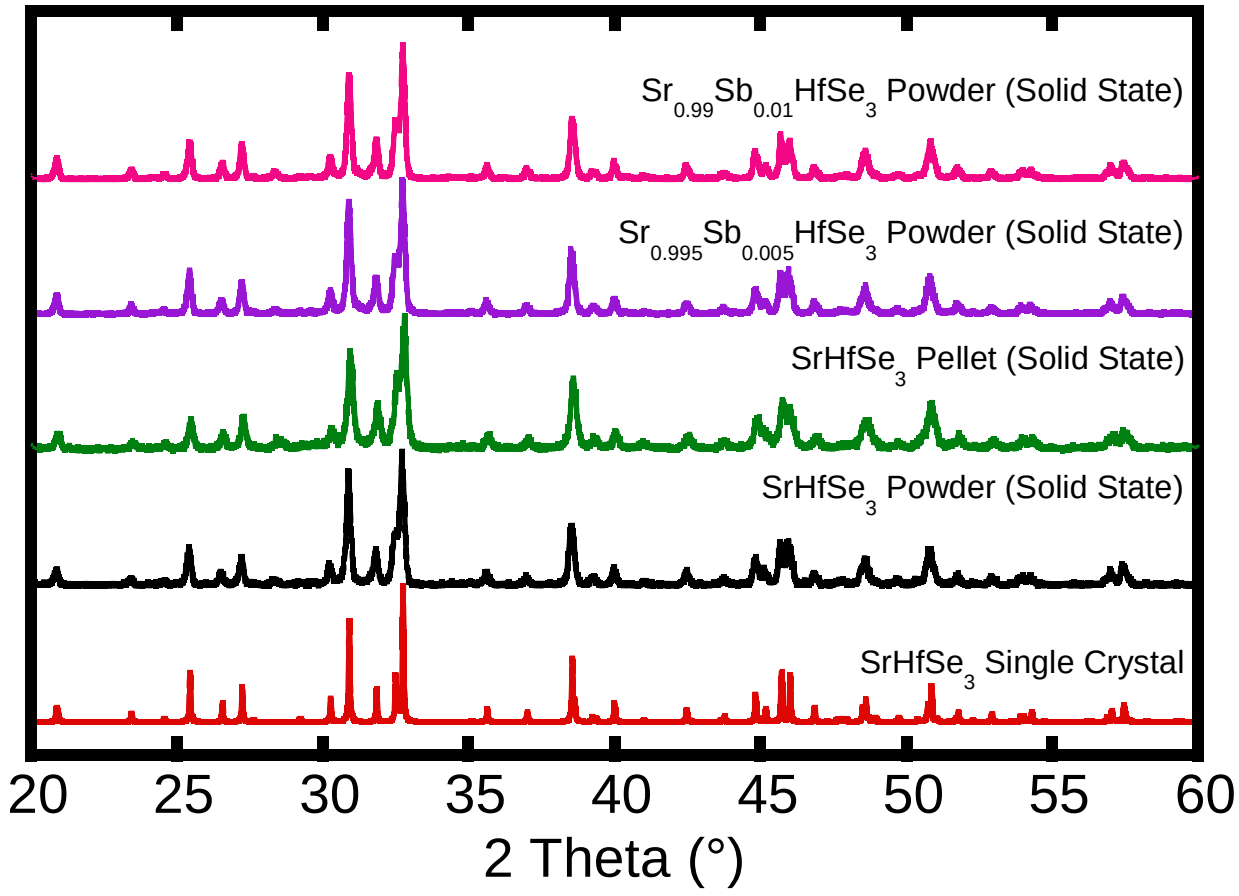

Figure 6-1: X-ray diffraction patterns of $SrHfSe_3$ compounds synthesized using technique 1 (solid state synthesis) and technique 2 (mechanical alloying). Synthesis technique 1 successfully produced single phase needle-like $SrHfSe_3$ and Sb-doped $SrHfSe_3$. Hot pressing also did not change the structure of the compounds. Synthesis technique 2 did not produce single phase $SrHfSe_3$.

patterns. Synthesis technique 2, which utilized 100 hours of high-energy ball –milling to produce $SrHfSe_3$, was not successful in creating pure needle-like or distorted perovskite structure, and instead features a small amount of binary impurity compounds such as $HfSe_3$, $Hf_{1.35}Se_2$, and $HfSe_2$ which were identified from X-ray diffractograms.

Table 6-1: Selected crystallographic data from refinement of single crystal of $SrHfSe_3$.

Crystal syst. space group	Orthorhombic, P*nma* (#62)
Formula weight (g/mol)	502.99
Calculated density (g/cm^3)	6.576
Lattice parameters (Å)	
a =	8.901(2)
b =	3.943(1)
c =	14.480(3)
V(Å^3); Z	508.07(2); 4
Radiation (Å)	λ (MoK$_\alpha$) = 0.71073
μ (cm^{-1})	522
2θ range	7° ≤ 2θ ≤ 67°
index range	–13 ≤ h ≤ 13
	–5≤ k ≤ 5
	–21 ≤ l ≤ 21
Transmission factors	0.029 - 0.198
Diff. elec. density [eÅ^{-3}]	+3.32 to –2.77
R_1 (F_o>4σ(F_o))[a]	0.029
wR_2 (all) [b]	0.065
GOF	1.148

[a] $R_1 = \Sigma||F_o|-|F_c||/\Sigma|F_o|$; [b] $wR_2 = [\Sigma w(F_o^2-F_c^2)^2/\Sigma w(F_o^2)^2]^{1/2}$

Table 6-2: Wycko Positions (WP), Atomic Coordinates, site occupancies, and Equivalent Isotropic Displacement Parameters ($U_{eq}/10^{-4}$ Å^2) for All Atoms in the Asymmetric Unit of $SrHfSe_3$ 300 K.

Atom	W.P.	*x*	*y*	*z*	*Ueq*
Hf1	4c	0.8308(6)	1/4	0.4431(3)	80(2)
Sr1	4c	0.5628(2)	3/4	0.6779(8)	112(3)

Se1	4c	0.6611(2)	1/4	0.5120(8)	73(2)
Se2	4c	0.9792(2)	1/4	0.6073(6)	59(2)
Se3	4c	0.7093(2)	1/4	0.2829(7)	78(3)

U_{eq} is defined as one-third of the trace of the orthogonalized U_{ij} tensor

Table 6-3: Bond valence sum calculations for $SrHfSe_3$ at 300 K.

Atom	BVS	Oxidation
Sr1	2.11	2+
Hf1	4.03	4+
Se1	2.16	2-
Se2	2.27	2-
Se3	2.14	2-

Table 6-4: Selected interatomic distances for $SrHfSe_3$.

Bond type	Distance [Å]	Bond type	Distance [Å]
Hf1—Se3	2.559(2)	Sr1—Se3^{v}	3.173(2)
Hf1—Se1	2.676(9)	Sr1—Se3^{vi}	3.174(2)
Hf1—Se1^{i}	2.676(9)	Sr1—Se2^{vii}	3.198(2)
Hf1—Se2^{ii}	2.698(8)	Sr1—Se3^{viii}	3.212(2)
Hf1—Se2^{iii}	2.698(8)	Sr1—Se3^{ix}	3.212(2)
Hf1—Se2	2.720(9)	Sr1—Se1^{iv}	3.229(2)
		Sr1—Se1	3.229(2)
		Sr1—Se1^{v}	3.395(2)
		Sr1—Se2^{iv}	3.844(2)

[a] Operators for generating equivalent atoms: (i) x, 1+y, z; (ii) 1-x, 1-y, 1-z; (iii) 1-x, -y, 1-z; (iv) x, -1+y, z; (v) 1-x, -1-y, 1-z; (vi) 1-x, -y, 1-z; (vii) -0.5+x, -1+y, 1.5-z; (viii) 1.5-x, -y, 0.5+z; (ix) 1.5-x, -1-y, 0.5+z; (x) 0.5+x, 1+y, 1.5-z; (xi) 1.5-x, 1-y, 0.5+z; (xii) 1.5-x, -y, -0.5+z; (xiii) 1.5-x, -1-y, -0.5+z; (xiv) 1.5-x, 1-y, -0.5+z.

A single crystal of $SrHfSe_3$ was successfully grown by annealing the solid-state synthesized compound at 1373 K for 10 days as described in the experimental procedure. Long black needle-like crystals were harvested from the annealed pellet, and analyzed using X-ray diffraction techniques. The results confirm that $SrHfSe_3$ forms with the needle-like orthorhombic structure *Pnma* (#62), with a = 8.9001(18) Å, b = 3.9424(8) Å, and $\alpha = \beta = \gamma = 90°$, Table 6-1 and Table 6-2. Bond valence sum calculations are reported in Table 6-3 which assume full occupation of each site.[238] Selected interatomic distances are shown in Table 6-4. The theoretical powder X-ray diffraction pattern created from the single crystal structure solution was compared to the diffractograms of the samples produced using synthesis technique 1 with good agreement with the calculated Goldschmidt tolerance factor of $t = 0.82$, where $t = (r_A + r_0)/\sqrt{2}\,(r_B + r_0)$ and r_A is the ionic radius of the A-cation (Sr), r_B is the ionic radius of the B-cation (Hf), and r_0 is the ionic radius of the anion (Se).[237] WDXRF characterization of the synthesized powder shows a composition of $Sr_{1.16}Hf_{0.90}Se_3$, slightly Sr-rich with Fe contamination of less than 0.1 wt. %. This phase structure remained consistent through hot pressing, signaling that the synthesized compound is single phase. Sb-doped samples of $SrHfSe_3$ produced using synthesis technique 1 yielded similar diffraction patterns. Synthesis technique 2, which utilized 100 hours of high-energy ball–milling to produce $SrHfSe_3$, was not successful in creating pure needle-like or distorted perovskite structure, and instead features a small amount of binary impurity compounds such as $HfSe_3$, $Hf_{1.35}Se_2$, and $HfSe_2$ which were identified from X-ray diffractograms.

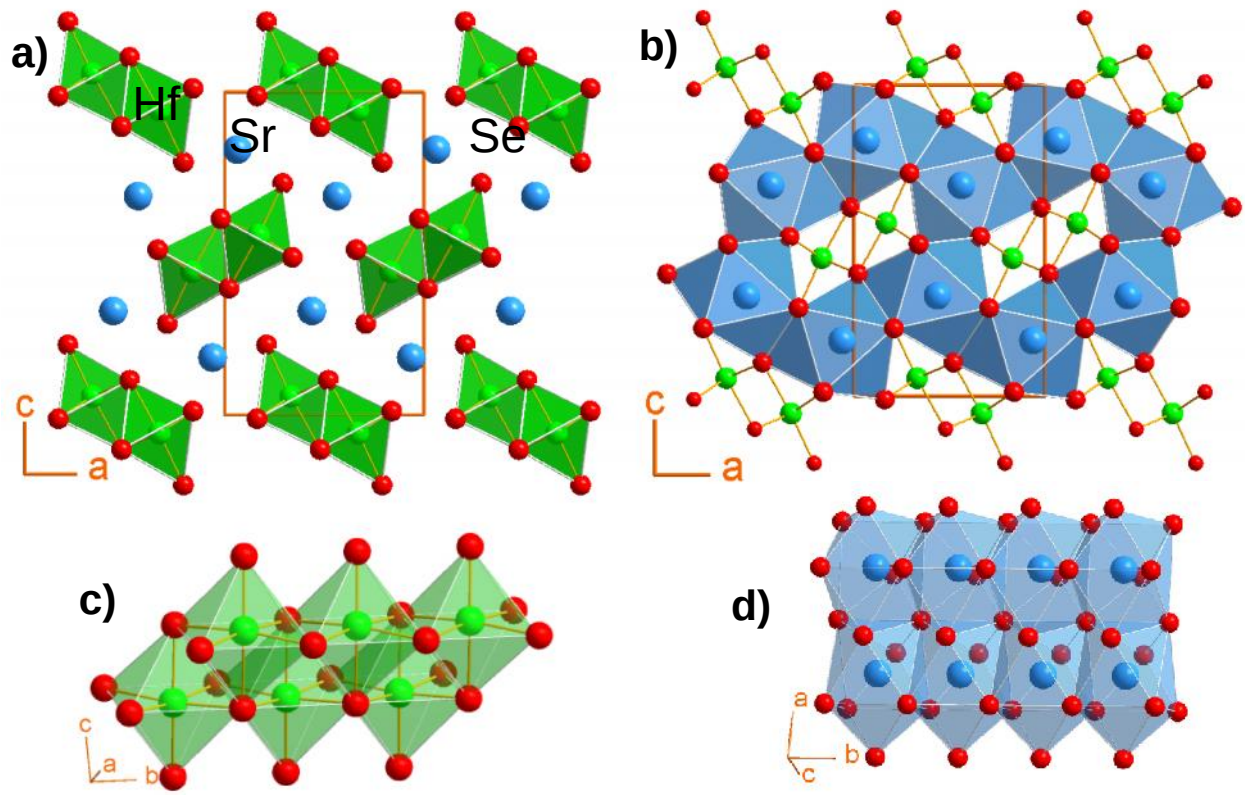

Figure 6-2: Projection of the crystal structure of SrHfSe3 along the b-axis highlighting: a) the octahedral coordination around Hf atoms and b) the tricapped trigonal prismatic coordination around Sr atom; c) Double chains of edge-sharing HfSe6 octahedra running parallel to the b-axis; d) Adjacent SrSe9 tricapped trigonal prims share faces in all directions to form a 3D network separating adjacent double chains of edge-sharing HfSe6 octahedra.

. The solution of the single crystal diffraction yields a crystal structure very similar to needle-like $SrZrSe_3$ (prototype structure NH_4CdCl_3) first developed by Tranchitella *et al.*[234] All atoms reside at Wyckoff position *4c*, with edge-sharing columns of $HfSe_6$ projecting along the *b*-axis, Figure 6-2. Between these columns, Sr is coordinated by 9 Se atoms forming distorted polyhedra. The Hf-Se distances range from 2.5597(14) to 2.6977(8) Å, whereas, the Sr-Se distances range from 3.1734(13) to 3.3949(16) Å with a longer bond of 3.8444(17) similar to $SrZrSe_3$. Thus, the bonding of $SrHfSe_3$ is nearly identical to the reported bonding of $SrZrSe_3$, which is to be expected due to the similar oxidation state (+4) and ionic radius of Zr (230 pm) and Hf

(225). The cell volume of $SrHfSe_3$, 508.1(2) $Å^3$, is also within 1% of the cell volume of $SrZrSe_3$, 513.0(4) $Å^3$.

Differential scanning calorimetry of the solid-state produced $SrHfSe_3$ indicates that the material is generally single phase, Figure 6-3. At ~700 K on the initial heating cycle a small peak appears which subsequently disappears upon cooling, and thus can be attributed to further ordering of the structure or even the completion of the reaction of the system which is supported by the identical XRD patterns for the solid-state powder and the hot-pressed pellet of the powder. At ~820 K and ~1033 K small peaks consistent in multiple heating and cooling cycles can be identified as phase changes of the impurity SrSe.[239] Given that SrSe was not identified in the XRD of the $SrHfSe_3$ compound produced by solid-state synthesis, it is reasoned that the SrSe content is relatively insignificant for transport and band gap measurements. The material appears to melt congruently at 1510 K.

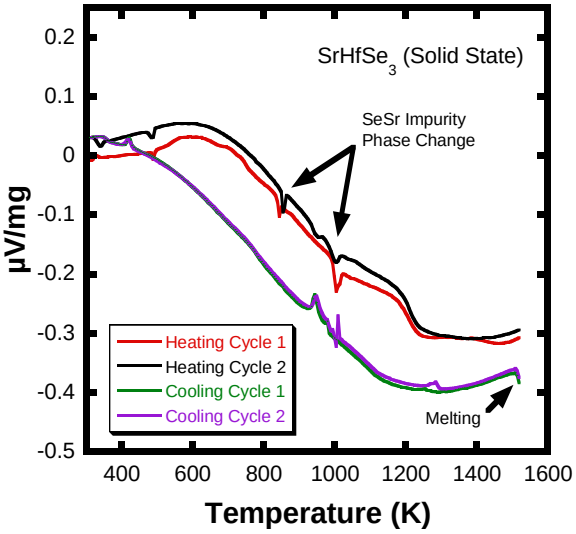

Figure 6-3: Differential scanning calorimetry (DSC) results for $SrHfSe_3$ produced by solid-state synthesis. The compound is nearly single phase, showing a small impurity phase change at 820 K and 1033 K that can be attributed to SrSe.

X-ray photoelectron spectroscopy confirms that the material is predominantly needle-like $SrHfSe_3$, with oxidation states of Sr^{2+}, Hf^{4+}, and Se^{2-}, Figure 6-4. There is evidence, by the pairs of doublet peaks for both Sr 3d and Se 3p spectra, that there exists a small quantity of impurity SrSe phase present. The fitting parameters used for Sr 3d peaks assumes a full-width half-maximum ratio of 0.69 rather than the theoretical 0.67. The Hf 4f spectrum does not indicate the presence of any Hf-based compounds beyond $SrHfSe_3$.

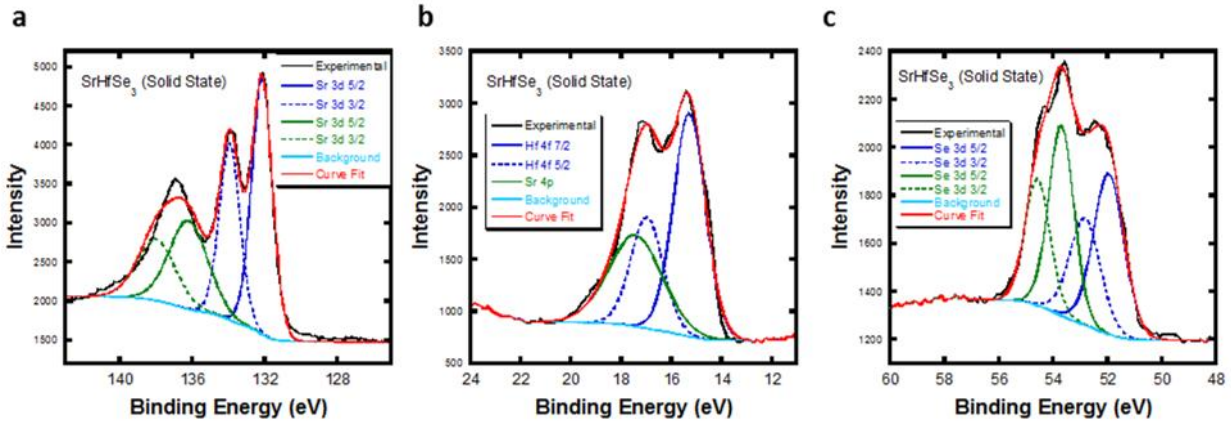

Figure 6-4: a) XPS spectrum and curve-fitting analysis of Sr^{2+} in $SrHfSe_3$. Two sets of doublet peaks indicate possible SrSe impurity in small amounts. b) XPS spectrum and curve-fitting analysis of Hf^{4+} in $SrHfSe_3$. c) XPS spectrum and curve-fitting analysis of Se^{2-} in $SrHfSe_3$. Two sets of doublet peaks indicate possible SrSe impurity in small amounts.

6.3.2 Synthesis and Crystal structure of Distorted Perovskite $BaHfSe_3$.

Attempts to produce single phase $BaHfSe_3$ using synthesis technique 1 (solid state method) consistently created compounds with substantial portions of binary impurity phases $HfSe_2$, Hf_2Se, $Hf_{1.35}Se_2$, and $BaSe_3$ as determined from X-ray diffraction. However, synthesis technique 2 (mechanical alloying) was successful in creating a ternary compound that can be identified via XRD pattern identification as the perovskite $BaHfSe_3$, Figure 6-5, using the known diffractogram of perovskite $BaHfO_3$. Intriguingly, the tolerance factor for this compound, $t = 0.88$, is slightly below the threshold for perfect cubic perovskites, $t = 0.9$, but could be stabilized by a high defect density due to the intense mechanical alloying. Unfortunately, the synthesized fine black powder, produced after a lengthy 100 hours of ball-milling, was determined by WDXRF to contain 11.4 wt.% iron as a contaminate originating from the hardened steel jars. Rietveld refinement performed on the diffractogram using the perovskite phase $CaTiO_3$ (ICSD #153174) primitive cubic symmetry with $BaHfO_3$ lattice parameters and atomic spacing, space group Pm-3m (#221), as a prototype structure for $BaHfSe_3$ identified Fe_3O_4, magnetite, as the iron-based impurity phase with a X^2 of 5.66 and R_f factors 26.7 for $BaHfSe_3$ and 34.3 for Fe_3O_4.[240,241] Based

on this refinement, the lattice parameters, atomic positions, and selected unique bond distances are reported in

Table 6-5. However, large discrepancy between the experimental density (6.9 g/cm^3) and the calculated density using $Pm\bar{3}m$ symmetry (12.604 g/cm^3) indicate that the structure could be more closely related to the tetragonal *P42mc* symmetry with calculated density of 5.33791 g/cm^3, Figure 6-6.

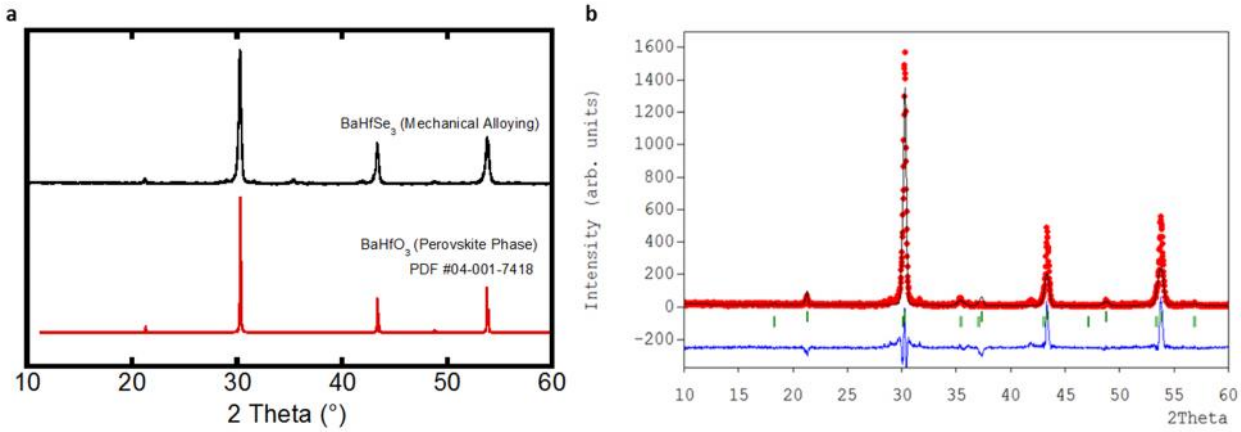

Figure 6-5: Powder X-ray diffraction pattern for $BaHfSe_3$ synthesized using mechanical alloying (synthesis technique 2). The structure shares a similar profile to perovskite $BaHfO_3$.

Table 6-5: Refined lattice parameters, atomic positions, and selected bond lengths determined by Rietveld refinement of $BaHfSe_3$ pellet samples using $BaHfO_3$ structure as reference.

Space Group		**FW** (g/mol.)	**Density** (g/cm^3)
Pm	#221	552.71	12.604

Cell Parameters

a	*b*	*c*	*α*	*β*	*γ*	Cell Volume ($Å^3$)	R_f	X^2
4.176(1)	4.176(1)	4.176(1)	90	90	90	72.82(5)	26.7	5.66

Atom	**Wyckoff Position**	**x**	**y**	**z**	**Selected Bond Lengths**	
Ba1	1a	0	0	0	Se1 - Se1	2.9528(1)
Hf1	1b	0.5	0.5	0.5	Se1 - Ba1	2.9528(1)
Se1	3c	0	0.5	0.5	Se1 - Hf1	2.0879(1)

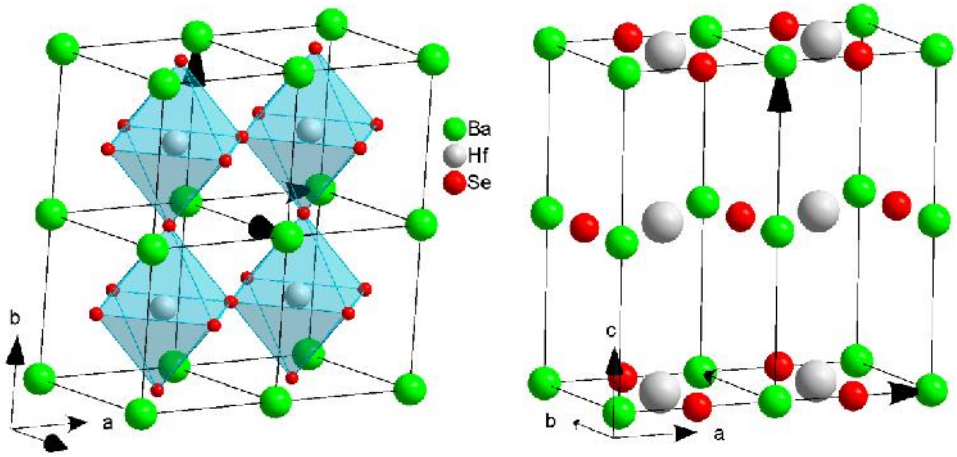

Figure 6-6: Structure of $BaHfSe_3$ based on refinement using cubic perovskite structure of $BaHfO_3$ (left) and the tetragonal structure (right).

Differential scanning calorimetry results for mechanically alloyed $BaHfSe_3$ are shown in Figure 6-7, which show a potential phase change for $BaHfSe_3$ near 775 K and a melting point approaching 1375 K. Based on these results, it appears that $BaHfSe_3$ melts congruently and does not exhibit any secondary phases associated with Se-based binary impurities. Given the consistency in the first and second heating cycles as well as the first and second cooling cycles, it

can be concluded that $BaHfSe_3$ is extremely thermally stable to temperatures higher than 1100 K. High-resolution XPS spectra of Ba 3d, Hf 4f, and Se 3d peaks are shown in Figure 6-8. Consistent with DSC data, the XPS spectra show no secondary bonding for Ba, Hf or Se, exhibiting a single set of peaks fit for each species. A phase change for the impurity Fe_3O_4, originating from the 100 hours of ball milling in steel jars, can be seen at 839 K.[242]

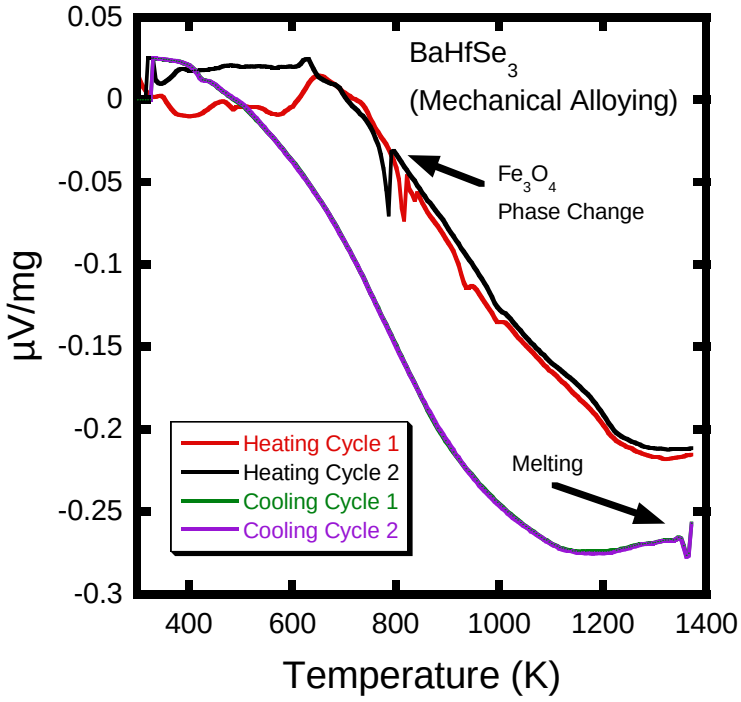

Figure 6-7: Differential scanning calorimetry results of $BaHfSe_3$ perovskite material produced using mechanical alloying. The impurity Fe_3O_4 shows a phase change at ~839 K.[242]

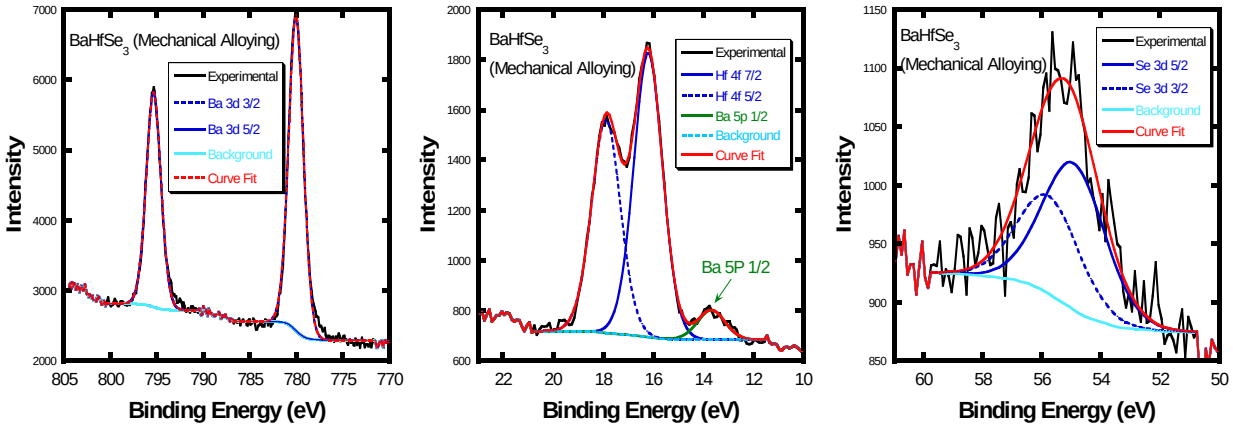

Figure 6-8: a) XPS spectrum and curve-fitting analysis of Ba^{2+} in $BaHfSe_3$. Single set of doublet peaks indicates that Ba^{2+} only exists in the ternary phase. b) XPS spectrum and curve-fitting analysis of Hf^{4+} in $BaHfSe_3$. c) XPS spectrum and curve-fitting analysis of Se^{2-} in $BaHfSe_3$.

6.3.3 Thermoelectric properties.

Densified pellets of phase-pure $SrHfSe_3$, Sb-doped $SrHfSe_3$, and $BaHfSe_3$ were evaluated for thermal conductivity, electronic conductivity, and thermopower in the mid-temperature range, 300 – 700 K. Thermal conductivity results indicate that $SrHfSe_3$ exhibits a relatively low thermal conductivity of 0.9 – 1.3 W/mK in this temperature range, sufficient for thermoelectric application, Figure 6-9. The substitution of 0.5 mol. % and 1 mol. % Sb for Sr reduces the thermal conductivity further to 0.77. At temperatures below 673 K, 1 mol. % Sb yields the lowest thermal conductivity, which can be expected due to mass impurity scattering since the atomic mass of Sb is nearly 1.5 times greater than Sr, although there appears to be little difference in the thermal conductivity of 0.5 and 1 mol. % Sb at temperatures 673 K and beyond.

Perovskite $BaHfSe_3$ exhibits a much higher thermal conductivity compared to needle-like $SrHfSe_3$, measuring 2.7 W/mK at 300 K and rising to 3.1 W/mK at 873 K. $BaHfSe_3$ shows a similar thermal conductivity response over this temperature range to perovskite $BaTiO_3$, indicating that the perovskite structure inherently offers higher thermal conductivity than the needle-like structure, which offers a much more meandering path for phonon transport shown schematically

in Figure 6-10.[243] As Fe_3O_4 has a much higher thermal conductivity as high as 6 W/mK at 300 K, it is reasoned that this contribution could also have substantially increased the thermal conductivity of the perovskite $BaHfSe_3$ sample.

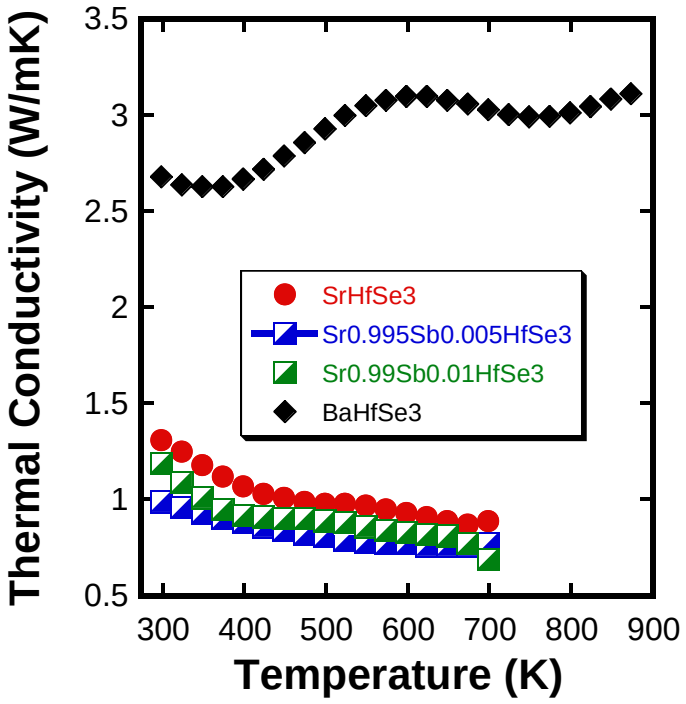

Figure 6-9: Thermal conductivity of $Sr_{1-x}Sb_xHfSe_3$ samples produced using solid-state method and $BaHfSe_3$ produced using mechanical alloying. Thermal conductivity decreases with increasing Sb content.

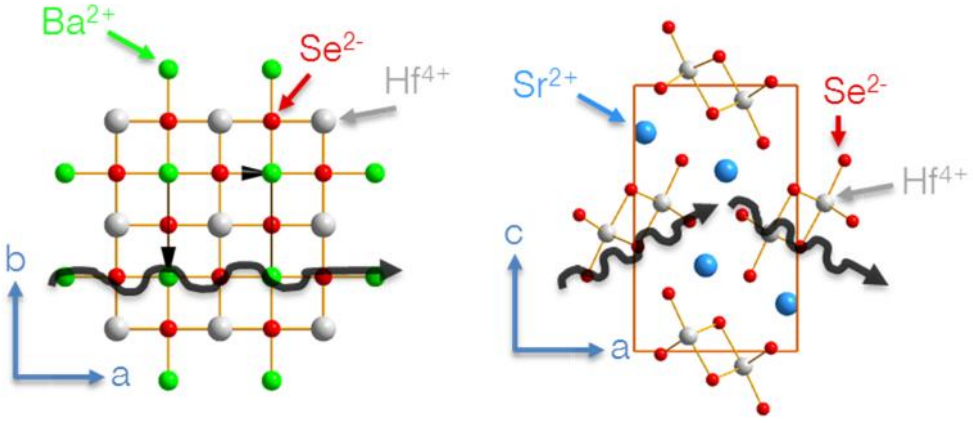

Figure 6-10: Possible phonon path through left) higher symmetry $BaHfSe_3$ showing smaller phonon mean free path compared to right) lower symmetry needle-like $SrHfSe_3$ as an explanation for the higher thermal conductivity of $BaHfSe_3$.

Room temperature Hall effect measurement of the densified solid state produced sample shows that $SrHfSe_3$ has a high p-type carrier concentration of 1.05 x 10^{19}. $SrHfSe_3$ samples were substitutionally doped with Sb ($5s^25p^3$) for Sr ($5s^2$) in order to reduce the number of carriers in the system to probe the effect on electronic transport properties. The electronic conductivity of $Sr_{1-x}Sb_xHfSe_3$ compounds is extremely low, increasing to a maximum of 6.7 S/cm for 0.5 mol. % Sb. Following this insulating nature, the thermopower of $SrHfSe_3$ shows p-type behavior rising to a maximum of 250 μV/K at 800 K, well within the appropriate range for thermoelectric power generation or other application. Interestingly, the thermopower at room temperature is only 6.7 μV/K and increases linearly to 600 K, which could mean that there is an n-to-p-type phase transition near room temperature. The linear increase in thermopower from 300 – 600 K indicated that holes are the single carrier species in this temperature regime. Sb content increases the thermopower for both 0.5 and 1.0 mol. % to 283 μV/K at 873 K. The thermopower is increased for both 0.5 and 1.0 mol. % Sb doping over the entire temperature regime. There is little difference in the magnitude of the 0.5 and 1.0 mol. % Sb doped samples; however, both samples show a significant increase in thermopower at room temperature compared to the undoped sample. Counterintuitively, Sb-doping, effectively adding electrons to the system, increased both the thermopower and electronic conductivity of $SrHfSe_3$ over the entire temperature range tested. One explanation for this behavior could be that the n-type doping moved the fermi level towards the conduction band: extrinsic carriers countering intrinsic carriers, increasing the effective mass of the carriers in the system, but also increasing the mobility of carriers in the system. The increased mobility and effective mass would therefore increase both the thermopower and conductivity with increasing Sb content. While the overall performance of this material is not impressive, Sb-doping did substantially improve both the maximum power factor, 0.522 $\mu W/cmK^2$ for 0.5 mol. % doped

at 798 K compared to 0.182 μW/cmK^2 at 698 K for $SrHfSe_3$, and the figure of merit, 0.046 for 0.5 mol. % doped at 698 K compared to 0.014 at 698 K for $SrHfSe_3$.

Room temperature Hall effect measurements for $BaHfSe_3$ did not produce sufficiently discernable data for determination of carrier concentration and mobility, instead identifying a magnetic interference due to the Fe_3O_4 impurity. Despite this issue, contaminated $BaHfSe_3$ densified samples were used for electronic transport measurements in order to elucidate basic thermoelectric performance data. The electronic conductivity of $BaHfSe_3$ is similar to $SrHfSe_3$, starting at 0.53 S/cm at 300 K and rising linearly to 2.62 S/cm at 873 K, which again is quite low for thermoelectric applications, and can be attributed to either low carrier concentration or low carrier mobility. Interestingly, the thermopower of this material has n-type characteristic starting at –49.62 μV/K at 300 K and linearly increasing to -105.22 μV/K at 873 K. It is, therefore, hypothesized that the perovskite structure of $SrHfSe_3$ would also be an n-type material given the predicted similarity in the crystal structure to perovskite $BaHfSe_3$. Given the low electronic conductivity of this material over the experimental temperature range as well as the substantially high thermal conductivity, the power factor reaches a maximum of only 0.030 μW/cmK^2 at 873 K and a figure of merit of only 8.1×10^{-4}. However, the results of Sb-doping of $SrHfSe_3$ give promise to the potential to dope this material to significantly increase its thermoelectric performance.

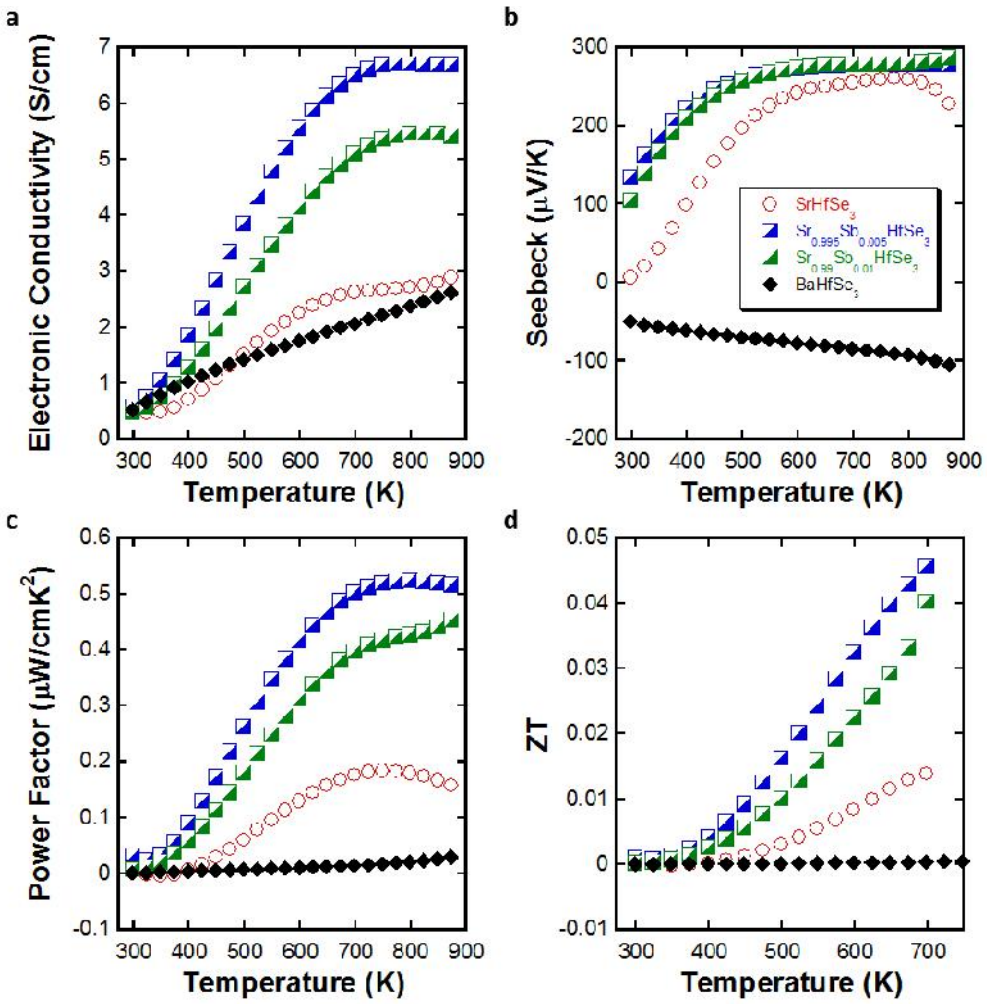

Figure 6-11: a) Electronic conductivity of $Sr_{1-x}Sb_xHfSe_3$ and $BaHfSe_3$ samples. Conductivity is maximized for Sb content of 0.5 mol. % due to a reduced carrier concentration. b) Thermopower of $BaHfSe_3$ and $Sr_{1-x}Sb_xHfSe_3$ samples showing a maximum with 0.5 mol. % Sb. c and d) Power factor and figure of merit, ZT, for $BaHfSe_3$ and $Sr_{1-x}Sb_xHfSe_3$ samples.

6.3.4 Optical properties

The optical band gap of each material was determined by quantifying the diffuse reflectance of each sample over the near-IR and UV-visible light spectrums. Tauc plots of the response of $Sr_{1-x}Sb_xHfSe_3$ samples are shown in Figure 6-12. The direct transmission model is applied to all samples as direct band gaps were estimated from the density functional theory analysis performed by Sun et al. associated with $SrHfSe_3$ and $BaHfSe_3$.[232] For $Sr_{1-x}Sb_xHfSe_3$ samples the band gap is estimated at 1.05 for the undoped sample, increasing to 1.7 eV and 1.85

eV for the 0.5 and 1.0 mol. % samples respectively. The increase in band gap through Sb doping offers evidence that beyond increasing the fermi level, Sb doping dramatically changes the electronic structure of the system. This is an intriguing result as it identifies a possible avenue for engineering the band gap of the material for photovoltaic applications. The ideal direct band gap for photovoltaic applications is expected to be between 1.02 and 1.15 eV, which has the promise for efficiencies eclipsing 28%, and thus, Sb-doped needle-like $SrHfSe_3$ appears to provide a promising opportunity for further development.[244]

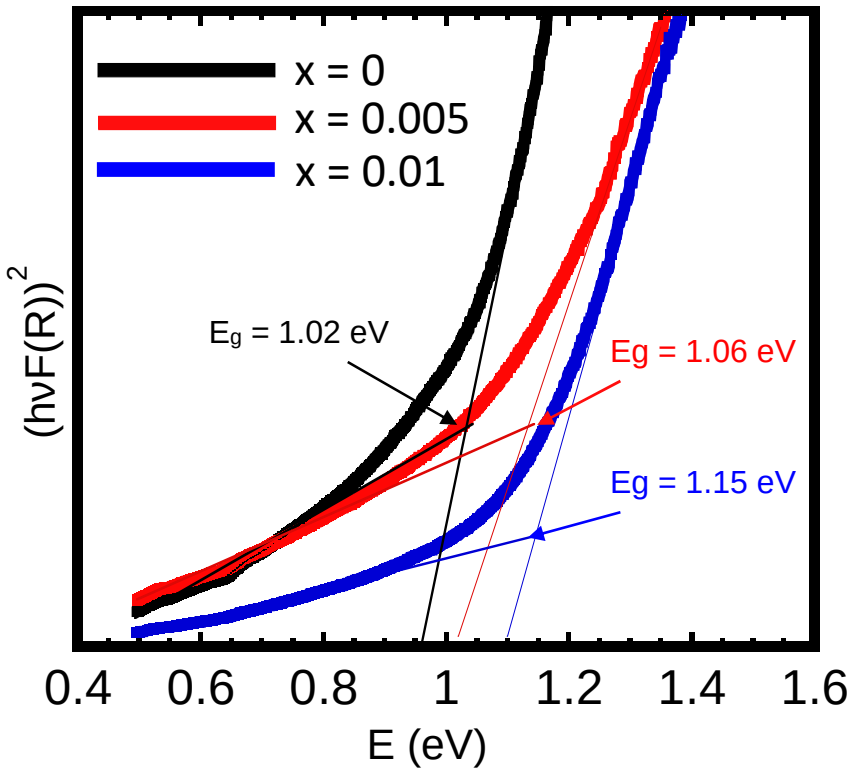

Figure 6-12: Optical band gaps of $SrHfSe_3$, $Sr_{0.995}Sb_{0.005}HfSe_3$, and $Sr_{0.99}Sb_{0.01}HfSe_3$ showing increasing band gap with increasing Sb content.

A similar procedure was conducted to determine the band gap of $BaHfSe_3$ produced by mechanical alloying. Multiple peaks in the absorption spectrum are associated with both $BaHfSe_3$ and impurity Fe_3O_4, which has a reported band gap between 1.8 and 2.02 eV for nanoparticles,[245] which is appropriate due to the extensive ball-milling of the sample. Based on this analysis the

band gap of $BaHfSe_3$ was estimated to be ~1.6 eV, which is within the predicted ideal energy level for photovoltaic conversion efficiency.

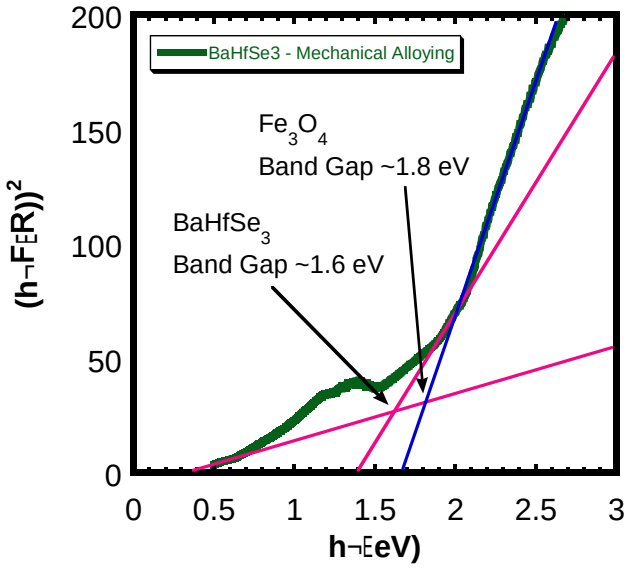

Figure 6-13: Tauc plot of optical absorption spectrum of BaHfSe3 produced by mechanical alloying. Band gap is estimated to be ~1.6 eV.

6.4 Conclusions

In summary, we have investigated the synthesis of $SrHfSe_3$ and $BaHfSe_3$ compounds using both solid state and mechanical alloying methods. $SrHfSe_3$ needle-like phase pure samples were produced using the solid state method, as well as samples doped with 0.5 and 1.0 mol. % Sb for Sr. A single crystal of $SrHfSe_3$ was grown and the crystal structure was identified and compared with high precision to that of the bulk samples produced. $BaHfSe_3$ was produced in the perovskite phase by means of mechanical alloying for 100 hours and hot pressing, whereas the solid state synthesis method failed to produce a pure phase. The diffraction pattern of $BaHfSe_3$ was compared to that of the known perovskite $BaHfO_3$ with good agreement. Fe_3O_4 impurity phases were identified in the $BaHfSe_3$ deriving from the extensive ball-milling. This represent the first known production of a selenide-based perovskite material in bulk form. It is also important to note that

high temperature synthesis was not necessary to produce this compound, offering a potentially low-cost and low-sophistication batch manufacturing technique.

Thermal and electronic transport properties were collected for each densified bulk material. $SrHfSe_3$ was determined to exhibit a low thermal conductivity and insulating electronic behavior with a thermopower greater than 200 μV/K from 520 – 800 K, producing a thermoelectric figure of merit of only 0.014 at 698 K. Sb doping reduced the thermal conductivity of $SrHfSe_3$ further to a low point of 0.77 at ~800 K. Sb doping also increased the electronic conductivity and thermopower of $SrHfSe_3$, possibly by reduction of carrier concentration, raising the figure of merit to 0.046 for 0.5 mol. % Sb doped at 698 K. In contrast, perovskite $BaHfSe_3$ yielded n-type insulating behavior with a much higher thermal conductivity, possibly due to Fe_3O_4 contamination. The maximum thermopower of $BaHfSe_3$ is -105.22 μV/K at 873 K, yielding a small figure of merit of 8.1×10^{-4} μV/K.

The optical band gaps of each material were determined by the diffuse reflectance method and subsequent Kubelka-Munk treatment. $SrHfSe_3$ was shown to yield a band gap of ~1.05 eV, which was increased by Sb doping of 0.5 mol. % to ~1.7 eV and further to ~1.85 eV by doping of 1.0 mol. % Sb. Perovskite $BaHfSe_3$ yielded a band gap of ~1.6 eV, within the predicted ideal range for photovoltaic devices. Both of the band gaps for $SrHfSe_3$ and $BaHfSe_3$ are in good agreement with the predicted values from DFT calculations.

CHAPTER 7

GENERAL CONCLUSIONS AND FUTURE WORKS

7.1 Summary

The goal of this work was to further the development of advanced materials for thermoelectric, magnetic, and photovoltaic applications by engineering the material properties of important transition metal chalcogenide compounds. This goal was accomplished by the systematic investigation of the effects of synthesis, stoichiometry, and processing of materials on the resultant crystal structure, and ultimately the relationships between structure and useful physical properties. This work led to a series of discoveries that will enable both the creation and optimization of new advanced materials with interesting optoelectronic, thermoelectric, and magnetic properties.

Through use of an innovative low-temperature two-step synthesis approach, a template nanostructure was used to efficiently produce hexagonal nanoplatelets of CuAgSe with promising thermoelectric performance. This process incorporated solvothermal synthesis to create relatively uniform hexagonal nanoplatelets of $Cu_{2-x}Se$ which were then used as sacrificial templates to be converted via ion exchange mechanism. Leveraging the high mobility of Cu^{+} ions in the systems of both $Cu_{2-x}Se$ and CuAgSe allowed for a controlled reaction at room temperature in an electrolyte. This process was also shown to offer conversion not only of $Cu_{2-x}Se$ to CuAgSe, but

also further to Ag_2Se. Thus, this important technique offers a low-temperature, scalable process toward the production of nanostructured versions of metastable phase materials which can be applied to the creation of thin film and bulk devices.

$CuAl(S_xSe_{1-x})_2$ compounds were also investigated for their use as potential thermoelectric bulk materials, studying the effects of synthesis technique, densification, and transition metal substitutional doping. While DFT studies had predicted that these alloys would provide high *ZT*, these materials produced high Seebeck coefficient, but significantly insulating electronic transport behavior, severely impacting their thermoelectric performance, regardless of the processing used. Still, doping studies utilizing transition metals elucidated important information about the possible optimization of these wide band gap materials. Isoelectronic substitution of Cu^+ by Ag^+ reduced the thermal conductivity of the system, but also reduced the electronic conductivity of the system. At 10 mol. % Ag the compound also exhibited a Seebeck coefficient similar to that of CuAgSe, indicating that CuAgSe nanoparticles could have segregated from the bulk of $CuAl(S_xSe_{1-x})_2$, potentially an important strategy for improving the electronic transport of the system independent of the thermal transport. Substitution of Al^{3+} by transition metals was also shown to greatly reduce the thermal conductivity of $CuAl(S_xSe_{1-x})_2$ without affecting the electronic transport of the system, boosting the *ZT*. These important findings could lead to the use of these wide band gap solid solutions as multifunctional materials that incorporate both photovoltaic and thermoelectric properties for innovative renewable energy devices.

A detailed study using refinement and characterization techniques of the dilute magnetic semiconductor $FeSb_2Se_4$ doped with In^{3+} for Sb^{3+} showed that the magnetic properties of the material could be adjusted by changes in the local carrier concentration without significantly affecting the structure. This important finding shows that the ferromagnetic behavior of the system

can be mediated though doping, a valuable characteristic of this material for spintronic application. This study not only verified the role that BMPs play in the ferromagnetic nature of $FeSb_2Se_4$, but also quantified the strength of BMPs with respect to local carrier concentration, and verified that the layered structure of $FeSb_2Se_4$ is indeed antiferromagnetically coupled.

Lastly, solid-state synthesis and mechanical alloying approaches were utilized to produce the intriguing photovoltaics materials needlelike $SrHfSe_3$ and distorted perovskite $BaHfSe_3$. The creation of nearly-cubic $BaHfSe_3$ is the first distorted perovskite selenide created to date, providing n-type electronic behavior. Both $SrHfSe_3$ and $BaHfSe_3$ exhibited band gaps within the targeted range of 1.15 – 1.5 eV for solar cell applications. Sb-doping of $SrHfSe_3$ also indicated that the band gap of these materials could be tuned with very little dopant.

7.2 Future works

This work on ternary and quaternary transition metal based chalcogenide systems has delivered important insight into the fundamental electronic, magnetic, thermal and optical properties of newly engineered materials by discovering effective synthesis and processing approaches. The natural progression of this work is to utilize these innovative techniques coupled with the understanding of the effects of these techniques on the desired material properties to create new and promising materials, particularly in metastable phases, as well as the optimization of currently important thermoelectric, magnetic, and photovoltaic materials. Three such directions are 1) to further investigate the conversion of $Cu_{2-x}Se$ nanoplatelets into other ternary and quaternary materials such as $Cu(In,Ga)Se_2$ and $CuAl(S_xSe_{1-x})_2$, 2) to study the effects of other transition metal dopants in the $FeSb_2Se_4$ system in order to further manipulate the carrier concentration and thus the magnetic properties of the material, and 3) to continue to synthesize a series of perovskite selenides in both bulk and thin-film form for photovoltaic applications.

As mentioned in the conclusions section of Chapter 3, the application of the novel two-step low-temperature synthesis process to other materials systems has shown some exciting early results in the production of $CuAlSe_2$ compounds. One major roadblock in this study has been the small conversion rate from $Cu_{2-x}Se$ to $CuAlSe_2$ due in part to the creation of the intermediary CuSe phase. Thus, an important avenue to pursue is the production of CuSe and CuS template nanoplatelets to use for conversion into other phases, namely $CuAl(S_xSe_{1-x})_2$. Vinod et al. were able to create such CuSe hexagonal nanoplatelets using a similar liquid synthesis technique to the one presented in this work, producing platelets with significantly smaller diameter (~100 nm average).[246] Similar results have been shown by Liu et al. for the production of CuS hexagonal nanoplatelets.[247] Using these template nanoplatelets a series of interesting studies could be completed targeting the conversion of CuSe nanoplatelets to $CuAlSe_2$, the conversion of CuS nanoplatelets to $CuAlS_2$, and the creation of a mixed phase $CuAl(S_xSe_{1-x})_2$ system as a composite or solid solution by the densification of $CuAlSe_2$ and $CuAlS_2$ nanoplatelets. These experiments will undoubtedly offer new information as to the limiting factors associated with this synthesis process which will ultimately be useful for the production of other interesting and new copper-based ternary chalcogenide systems such as Cu_2BaSe_2, $Cu_{2-x}Sr_xSe_2$, and $Cu_{2-x}Au_xSe$.

The work in chapter 5 concerning the substitutional doping of In^{3+} for Sb^{3+} in the high T_c diluted magnetic semiconductor $FeSb_2Se_4$ has led to two exciting new avenues for research. First, the initial modeling using Langevin fitting into the effect of In^{3+} concentration on the strength of the bound magnetic polarons has not yet included the antiferromagnetic interactions between BMPs in the A and B layers of the system. Modeling of interaction BMPs in a system has been tackled by a few research groups, namely Durst et al. which developed a fairly simple model, but which does not accurately depict the BMP "bubble" of interaction at moderate temperature

ranges.[248] Given the relatively high temperature application possibilities for $FeSb_2Se_4$, Durst et al.'s model should be applied to this system in order to attempt to more accurately quantify the effect of In^{3+} concentration on the overall magnetic properties of the material. In addition to this new direction, further studies should include substitutional doping of $FeSb_2Se_4$ with other transition metals to determine the structural, electronic, and magnetic effects. In direct comparison with In^{3+} doping, Ga^{3+} of Y^{3+} could also be used for isostructural and isoelectronic doping, which have drastically different electron configurations compared to Sb. Other doping studies include the substitution of Mn for Fe, which would p-type dope the system further, possibly providing more carriers to each magnetic center as an amplifying effect. Bi^{3+} could also replace Sb^{3+} to introduce more electrons to the system and reduce the carrier concentration, perhaps selectively based on layer. The combination of accurately modeling BMPs and greater understanding of how dopants can manipulate the carrier concentration will provide the necessary information about $FeSb_2Se_4$ for its use in spintronic applications, and potentially for integration with silicon-based microchip processors. Finally, one further development for the continuation of this work would entail the experimental determination of the local carrier concentration in each layer. As mentioned in Chapter 5, Hall-effect measurements did not provide stable data from which to determine the carrier concentration, which would also not necessarily have determined the localized carrier concentration affecting the magnetic properties of the system. An interesting technique to accomplish this task would be carrier concentration profiling via capacitance-voltage profiler. This would require either the thin film deposition, by pulsed laser deposition or molecular beam epitaxy, or single crystal growth of $FeSb_{2-x}In_xSe_4$ by mass vapor transport means, which would then be analyzed using a system such as a Bio-Rad PN4300PC.

Finally, the work in Chapter 6 centered on the development of ABX_3 perovskite-like structures where A = Ca, Ba, or Sr, B = Hf, Zr, and X = Se; however, only needle-like $SrHfSe_3$ and perovskite $BaHfSe_3$ were synthesized, both with small impurities. Since both of these materials exhibited optical band gaps near the ideal range for photovoltaic application, the focus of this work should now be placed in two directions, towards the analysis of the absorption coefficient and cell integration and performance of $SrHfSe_3$ and $BaHfSe_3$, and also towards the production of these materials in a phase pure manner using solid-state synthesis and substitutional doping techniques. The logical next steps towards the experimental determination of the photovoltaic conversion efficiency of $SrHfSe_3$ and $BaHfSe_3$ is to create thin-films of these materials either by means of pulsed laser deposition or molecular beam epitaxy techniques. Ellipsometry methods can then be used to experimentally determine the absorption coefficients of these materials. Thin-film development of these perovskite-like structures will also indicate compatibility with industry standard substrates, notably lattice parameter matching. Secondly, attempts should be made to produce $SrHfSe_3$ and $BaHfSe_3$, as well as other perovskite phases of selenides, as phase pure using solid-state synthesis and other methods, utilizing a template $ABSe_3$ structure. Early attempts to produce $BaTiSe_3$ using a similar heating profile to that utilized to produce $BaUSe_3$ have been successful in producing the hexagonal phase (*P63/mmc* (#194)).[249] Substitutional doping of up to 75% Zr for Ti in this material using the same synthesis route have also shown to maintain the hexagonal perovskite phase, with some indication that the impurity phase of $Ba_{15}Zr_{14}Se_{42}$ has been created, Figure 7-1. As Zr replaces Ti, the (201) main peak of the XRD results shows that the unit cell increases in volume, signaling that the Zr is in a solid solution. This then presents a possible avenue for substitution of Hf for Ti to obtain phase pure $BaHfSe_3$, or even Ca and Sr for Ba, which could induce a lattice shift towards the distorted cubic perovskite phase with an expected band gap

preferential for the production of thin-film solar cells. Another possible route would be to produce template nanoplatelet structure of cubic BaSe using the solvothermal route described in Chapter 3 substituting barium acetate for copper acetate, and then to convert those platelets into the perovskite phases in the presence of excess selenium using the ion exchange reaction route. As seen with the example of cubic CuAgSe produced at room temperature, it could be possible to convert the cubic BaSe into cubic perovskite $BaHfSe_3$ or other perovskite compounds.

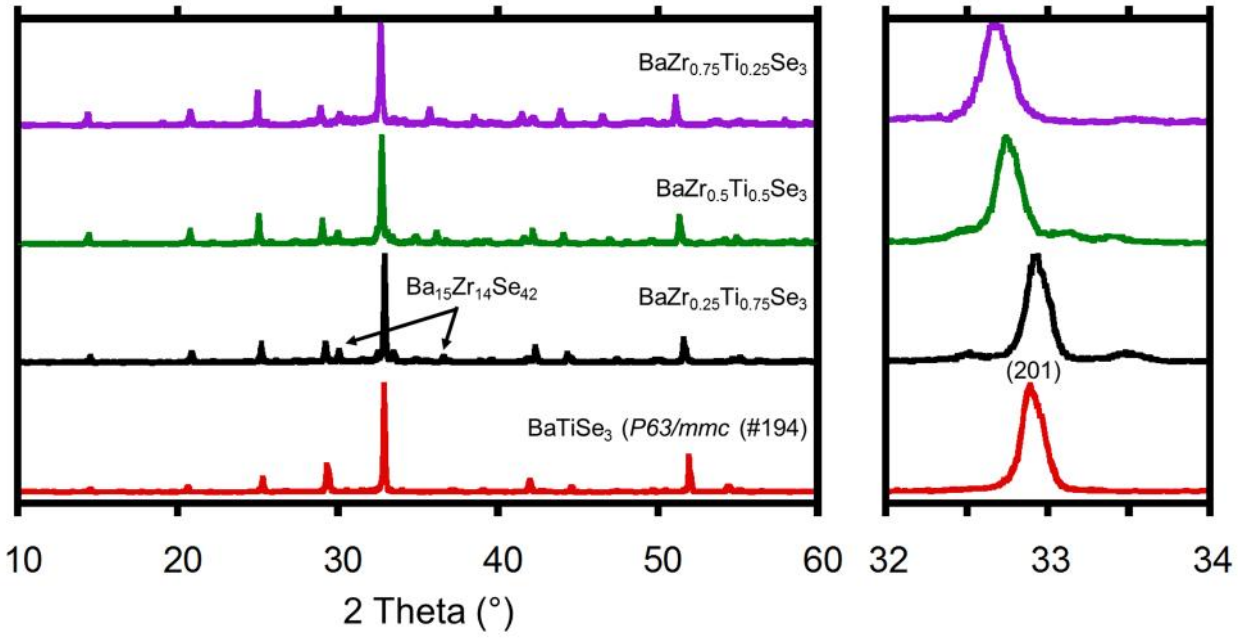

Figure 7-1: XRD results of solid-state synthesis of hexagonal perovskite $BaTiSe_3$ and substitutional doping of Zr for Ti. With increasing Zr content the (201) peak shifts to smaller angles indicating an enlarging of the unit cell.

REFERENCES

(1) Aramoto, T.; Kumazawa, S.; Higuchi, H.; Arita, T.; Shibutani, S.; Nishio, T.; Nakajima, J.; Tsuji, M.; Hanafusa, A.; Hibino, T. *Japanese Journal of Applied Physics* **1997**, *36*, 6304.

(2) Green, M. A. *Journal of Materials Science: Materials in Electronics* **2007**, *18*, 15.

(3) Wu, X. *Solar energy* **2004**, *77*, 803.

(4) Birkmire, R.; Dinetta, L.; Lasswell, P.; Meakin, J.; Phillips, J. *Solar Cells* **1986**, *16*, 419.

(5) Contreras, M. A.; Ramanathan, K.; AbuShama, J.; Hasoon, F.; Young, D. L.; Egaas, B.; Noufi, R. *Progress in Photovoltaics: Research and Applications* **2005**, *13*, 209.

(6) Kazmerski, L.; White, F.; Morgan, G. *Applied Physics Letters* **1976**, *29*, 268.

(7) Romeo, A.; Terheggen, M.; Abou-Ras, D.; Bätzner, D.; Haug, F. J.; Kälin, M.; Rudmann, D.; Tiwari, A. *Progress in Photovoltaics: Research and Applications* **2004**, *12*, 93.

(8) Repins, I.; Contreras, M. A.; Egaas, B.; DeHart, C.; Scharf, J.; Perkins, C. L.; To, B.; Noufi, R. *Progress in Photovoltaics: Research and applications* **2008**, *16*, 235.

(9) Yamashita, O.; Tomiyoshi, S.; Makita, K. *Journal of Applied Physics* **2003**, *93*, 368.

(10) Zhao, X.; Ji, X.; Zhang, Y.; Zhu, T.; Tu, J.; Zhang, X. *Applied Physics Letters* **2005**, *86*, 062111.

(11) Hicks, L.; Dresselhaus, M. *Physical Review B* **1993**, *47*, 12727.

(12) Tang, X.; Xie, W.; Li, H.; Zhao, W.; Zhang, Q.; Niino, M. *Applied physics letters* **2007**, *90*, 12102.

(13) Pirovano, A.; Lacaita, A. L.; Benvenuti, A.; Pellizzer, F.; Bez, R. *IEEE Transactions on Electron Devices* **2004**, *51*, 452.

(14) Hudgens, S.; Johnson, B. *MRS bulletin* **2004**, *29*, 829.

(15) Lacaita, A. *Solid-State Electronics* **2006**, *50*, 24.

(16) Wong, H.-S. P.; Raoux, S.; Kim, S.; Liang, J.; Reifenberg, J. P.; Rajendran, B.; Asheghi, M.; Goodson, K. E. *Proceedings of the IEEE* **2010**, *98*, 2201.

(17) Maimon, J.; Spall, E.; Quinn, R.; Schnur, S. In *Aerospace Conference, 2001, IEEE Proceedings.*; IEEE: 2001; Vol. 5, p 2289.

(18) Valov, I.; Waser, R.; Jameson, J. R.; Kozicki, M. N. *Nanotechnology* **2011**, *22*, 254003.

(19) Waser, R. *Microelectronic Engineering* **2009**, *86*, 1925.

(20) Burr, G. W.; Kurdi, B. N.; Scott, J. C.; Lam, C. H.; Gopalakrishnan, K.; Shenoy, R. S. *IBM Journal of Research and Development* **2008**, *52*, 449.

(21) Cockburn, B. F. In *MEMS, NANO and Smart Systems, 2003. Proceedings. International Conference on*; IEEE: 2003, p 321.

(22) Wolf, S.; Awschalom, D.; Buhrman, R.; Daughton, J.; Von Molnar, S.; Roukes, M.; Chtchelkanova, A. Y.; Treger, D. *Science* **2001**, *294*, 1488.

(23) Horii, H.; Yi, J.; Park, J.; Ha, Y.; Baek, I.; Park, S.; Hwang, Y.; Lee, S.; Kim, Y.; Lee, K. In *VLSI Technology, 2003. Digest of Technical Papers. 2003 Symposium on*; IEEE: 2003, p 177.

(24) Lai, S.; Lowrey, T. In *Electron Devices Meeting, 2001. IEDM'01. Technical Digest. International*; IEEE: 2001, p 36.5. 1.

(25) Panthani, M. G.; Akhavan, V.; Goodfellow, B.; Schmidtke, J. P.; Dunn, L.; Dodabalapur, A.; Barbara, P. F.; Korgel, B. A. *Journal of the American Chemical Society* **2008**, *130*, 16770.

(26) Rockett, A.; Birkmire, R. *Journal of Applied Physics* **1991**, *70*, R81.

(27) Lee, B.-S.; Abelson, J. R.; Bishop, S. G.; Kang, D.-H.; Cheong, B.-k.; Kim, K.-B. *Journal of Applied Physics* **2005**, *97*, 093509.

(28) Zhou, P.; Zhao, B.; Yang, J.; Zhang, Y. In *ACM SIGARCH computer architecture news*; ACM: 2009; Vol. 37, p 14.

(29) Biswas, K.; He, J.; Blum, I. D.; Wu, C.-I.; Hogan, T. P.; Seidman, D. N.; Dravid, V. P.; Kanatzidis, M. G. *Nature* **2012**, *489*, 414.

(30) Biswas, K.; He, J.; Zhang, Q.; Wang, G.; Uher, C.; Dravid, V. P.; Kanatzidis, M. G. *Nature chemistry* **2011**, *3*, 160.

(31) Girard, S. N.; He, J.; Zhou, X.; Shoemaker, D.; Jaworski, C. M.; Uher, C.; Dravid, V. P.; Heremans, J. P.; Kanatzidis, M. G. *Journal of the American Chemical Society* **2011**, *133*, 16588.

(32) Harman, T.; Walsh, M.; Turner, G. *Journal of electronic materials* **2005**, *34*, L19.

(33) He, J.; Blum, I. D.; Wang, H.-Q.; Girard, S.; Doak, J.; Zhao, L.-D.; Zheng, J.-C.; Casillas, G.; Wolverton, C.; Jose-Yacaman, M. *Nano letters* **2012**, *12*, 5979.

(34) Pei, Y.; LaLonde, A.; Iwanaga, S.; Snyder, G. J. *Energy & Environmental Science* **2011**, *4*, 2085.

(35) (US), N. R. C. *Materials science and engineering: Forging stronger links to users*, National Research Council (US), 1999.

(36) Howell, P. R. *Earth, air, fire & water: Elements of materials science*; Pearson Custom Pub., 2005.

(37) Goldsmid, H. J. *Introduction to thermoelectricity*; Springer, 2010; Vol. 121.

(38) Physics, U. D. o.

(39) Wei, S.-H.; Zhang, S. *Physical Review B* **2002**, *66*, 155211.

(40) Yi, J.; Lim, C.; Xing, G.; Fan, H.; Van, L.; Huang, S.; Yang, K.; Huang, X.; Qin, X.; Wang, B. *Physical review letters* **2010**, *104*, 137201.

(41) Banik, A.; Biswas, K. *Journal of Materials Chemistry A* **2014**, *2*, 9620.

(42) Banik, A.; Shenoy, U. S.; Anand, S.; Waghmare, U. V.; Biswas, K. *Chemistry of Materials* **2015**, *27*, 581.

(43) Liu, W.; Tan, X.; Yin, K.; Liu, H.; Tang, X.; Shi, J.; Zhang, Q.; Uher, C. *Physical review letters* **2012**, *108*, 166601.

(44) Majumdar, A. *Science* **2004**, *303*, 777.

(45) Snyder, G. J.; Toberer, E. S. *Nat Mater* **2008**, *7*, 105.

(46) Chung, D.-Y.; Hogan, T.; Brazis, P.; Rocci-Lane, M.; Kannewurf, C.; Bastea, M.; Uher, C.; Kanatzidis, M. G. *Science* **2000**, *287*, 1024.

(47) Parker, D.; Singh, D. J. *Physical Review B* **2010**, *82*, 035204.

(48) Pei, Y.; Lensch-Falk, J.; Toberer, E. S.; Medlin, D. L.; Snyder, G. J. *Advanced Functional Materials* **2011**, *21*, 241.

(49) Wang, H.; Pei, Y.; LaLonde, A. D.; Snyder, G. J. *Advanced Materials* **2011**, *23*, 1366.

(50) Dresselhaus, M. S.; Chen, G.; Tang, M. Y.; Yang, R.; Lee, H.; Wang, D.; Ren, Z.; Fleurial, J. P.; Gogna, P. *Advanced Materials* **2007**, *19*, 1043.

(51) Minnich, A.; Dresselhaus, M.; Ren, Z.; Chen, G. *Energy & Environmental Science* **2009**, *2*, 466.

(52) Narducci, D.; Selezneva, E.; Cerofolini, G.; Frabboni, S.; Ottaviani, G. *Journal of Solid State Chemistry* **2012**, *193*, 19.

(53) Paul, B.; Kumar, A.; Banerji, P. *Journal of Applied Physics* **2010**, *108*, 064322.

(54) Soni, A.; Shen, Y.; Yin, M.; Zhao, Y.; Yu, L.; Hu, X.; Dong, Z.; Khor, K. A.; Dresselhaus, M. S.; Xiong, Q. *Nano letters* **2012**, *12*, 4305.

(55) Xie, W.; Weidenkaff, A.; Tang, X.; Zhang, Q.; Poon, J.; Tritt, T. M. *Nanomaterials* **2012**, *2*, 379.

(56) Heremans, J. P.; Jovovic, V.; Toberer, E. S.; Saramat, A.; Kurosaki, K.; Charoenphakdee, A.; Yamanaka, S.; Snyder, G. J. *Science* **2008**, *321*, 554.

(57) Lin, S.; Li, W.; Chen, Z.; Shen, J.; Ge, B.; Pei, Y. *Nature communications* **2016**, *7*.

(58) Pei, Y.; Wang, H.; Snyder, G. *Advanced materials* **2012**, *24*, 6125.

(59) Zevalkink, A.; Toberer, E. S.; Bleith, T.; Flage-Larsen, E.; Snyder, G. J. *Journal of applied physics* **2011**, *110*, 013721.

(60) Zhang, J.; Chang, C.-Z.; Zhang, Z.; Wen, J.; Feng, X.; Li, K.; Liu, M.; He, K.; Wang, L.; Chen, X. *Nature communications* **2011**, *2*, 574.

(61) Hochbaum, A. I.; Chen, R.; Delgado, R. D.; Liang, W.; Garnett, E. C.; Najarian, M.; Majumdar, A.; Yang, P. *Nature* **2008**, *451*, 163.

(62) Kim, W.; Zide, J.; Gossard, A.; Klenov, D.; Stemmer, S.; Shakouri, A.; Majumdar, A. *Physical Review Letters* **2006**, *96*, 045901.

(63) Yang, J.; Meisner, G.; Chen, L. *Applied physics letters* **2004**, *85*, 1140.

(64) Poudel, B.; Hao, Q.; Ma, Y.; Lan, Y.; Minnich, A.; Yu, B.; Yan, X.; Wang, D.; Muto, A.; Vashaee, D. *Science* **2008**, *320*, 634.

(65) Poudeu, P. F.; D'Angelo, J.; Kong, H.; Downey, A.; Short, J. L.; Pcionek, R.; Hogan, T. P.; Uher, C.; Kanatzidis, M. G. *Journal of the American Chemical Society* **2006**, *128*, 14347.

(66) Pei, Y.-L.; Wu, H.; Sui, J.; Li, J.; Berardan, D.; Barreteau, C.; Pan, L.; Dragoe, N.; Liu, W.-S.; He, J. *Energy & Environmental Science* **2013**, *6*, 1750.

(67) Romano, G.; Di Carlo, A.; Grossman, J. C. *Journal of Computational Electronics* **2012**, *11*, 8.

(68) Telkes, M. *Journal of Applied Physics* **1947**, *18*, 1116.

(69) Zhang, H.; Talapin, D. V. *Angewandte Chemie International Edition* **2014**, *53*, 9126.

(70) Zhao, L.-D.; Lo, S.-H.; Zhang, Y.; Sun, H.; Tan, G.; Uher, C.; Wolverton, C.; Dravid, V. P.; Kanatzidis, M. G. *Nature* **2014**, *508*, 373.

(71) Pei, Y.; Shi, X.; LaLonde, A.; Wang, H.; Chen, L.; Snyder, G. J. *Nature* **2011**, *473*, 66.

(72) Chung, D. Y.; Hogan, T.; Schindler, J.; Iordanidis, L.; Brazis, P.; Kannewurf, C. R.; Chen, B.; Uher, C.; Kanatzidis, M. G. In *IEEE* 1997.

(73) Coey, J.; Sanvito, S. *Journal of Physics D: Applied Physics* **2004**, *37*, 988.

(74) Gregg, J.; Petej, I.; Jouguelet, E.; Dennis, C. *Journal of Physics D: Applied Physics* **2002**, *35*, R121.

(75) Snow, C.; Cooper, S.; Young, D.; Fisk, Z.; Comment, A.; Ansermet, J.-P. *Physical Review B* **2001**, *64*, 174412.

(76) Haas, C. *Critical Reviews in Solid State and Material Sciences* **1970**, *1*, 47.

(77) Nagaev, É. L. *Physics-Uspekhi* **1975**, *18*, 863.

(78) Callen, E. *Physical Review Letters* **1968**, *20*, 1045.

(79) Kalinnikov, V.; Aminov, T.; Novotortsev, V. *Inorganic materials* **2003**, *39*, 997.

(80) Koshihara, S.; Oiwa, A.; Hirasawa, M.; Katsumoto, S.; Iye, Y.; Urano, C.; Takagi, H.; Munekata, H. *Physical Review Letters* **1997**, *78*, 4617.

(81) Zener, C. *Physical Review* **1951**, *82*, 403.

(82) Zener, C. *Physical Review* **1951**, *81*, 440.

(83) Panigrahi, P.; Araujo, C. M.; Hussen, T.; Ahuja, R. *Science and Technology of Advanced Materials* **2016**.

(84) Ruderman, M. A.; Kittel, C. *Physical Review* **1954**, *96*, 99.

(85) Parkin, S.; Mauri, D. *Physical Review B* **1991**, *44*, 7131.

(86) Yafet, Y. *Physical Review B* **1987**, *36*, 3948.

(87) Gibbs, M.; Hill, E.; Wright, P. *Journal of Physics D: Applied Physics* **2004**, *37*, R237.

(88) Panguluri, R. P.; Kharel, P.; Sudakar, C.; Naik, R.; Suryanarayanan, R.; Naik, V.; Petukhov, A.; Nadgorny, B.; Lawes, G. *Physical Review B* **2009**, *79*, 165208.

(89) Steeneken, P.; Tjeng, L.; Elfimov, I.; Sawatzky, G.; Ghiringhelli, G.; Brookes, N.; Huang, D.-J. *Physical review letters* **2002**, *88*, 047201.

(90) Behan, A.; Mokhtari, A.; Blythe, H.; Score, D.; Xu, X.; Neal, J.; Fox, A.; Gehring, G. *Physical review letters* **2008**, *100*, 047206.

(91) Fukumura, T.; Jin, Z.; Ohtomo, A.; Koinuma, H.; Kawasaki, M. *Applied physics letters* **1999**, *75*, 3366.

(92) Dietl, T. *Nat Mater* **2010**, *9*, 965.

(93) Ohno, H.; Shen, A.; Matsukura, F.; Oiwa, A.; Endo, A.; Katsumoto, S.; Iye, Y. *Applied Physics Letters* **1996**, *69*, 363.

(94) Van Esch, A.; Van Bockstal, L.; De Boeck, J.; Verbanck, G.; Van Steenbergen, A.; Wellmann, P.; Grietens, B.; Bogaerts, R.; Herlach, F.; Borghs, G. *Physical Review B* **1997**, *56*, 13103.

(95) Story, T.; Gałazka, R.; Frankel, R. B.; Wolff, P. *Physical review letters* **1986**, *56*, 777.

(96) Dietl, T.; Ohno, H.; Matsukura, F.; Cibert, J.; Ferrand, D. *Science* **2000**, *287*, 1019.

(97) Torrance, J.; Shafer, M.; McGuire, T. *Physical Review Letters* **1972**, *29*, 1168.

(98) Wolff, P. *Semiconductors and Semimetals* **1988**, *25*, 413.

(99) Djieutedjeu, H.; Poudeu, P. F.; Takas, N. J.; Makongo, J.; Rotaru, A.; Ranmohotti, K. G.; Anglin, C. J.; Spinu, L.; Wiley, J. B. *Angewandte Chemie International Edition* **2010**, *49*, 9977.

(100) Moroz, N. A.; Lopez, J. S.; Djieutedjeu, H.; Ranmohotti, K. G.; Olvera, A.; Ren, P.; Page, A.; Takas, N. J.; Uher, C.; P. Poudeu, P. F. *Chemistry of Materials* **2016**.

(101) Williams, L.; Kioupakis, E.; Lopez, J.; Poudeu, P. F. P. In *APS Meeting Abstracts* 2016.

(102) SALAH M. BEDAIR, J. M. Z. A. N. E.-M. In *IEEE Spectrum* 2010.

(103) Guo, Q.; Ford, G. M.; Yang, W.-C.; Walker, B. C.; Stach, E. A.; Hillhouse, H. W.; Agrawal, R. *Journal of the American Chemical Society* **2010**, *132*, 17384.

(104) Santra, P. K.; Kamat, P. V. *Journal of the American Chemical Society* **2012**, *134*, 2508.

(105) Siebentritt, S.; Schorr, S. *Progress in Photovoltaics: Research and Applications* **2012**, *20*, 512.

(106) Todorov, T.; Gunawan, O.; Chey, S. J.; de Monsabert, T. G.; Prabhakar, A.; Mitzi, D. B. *Thin Solid Films* **2011**, *519*, 7378.

(107) *Technology Roadmap: Solar Photovoltaic Energy*, International Energy Agency - IEA, 2014.

(108) Fairman, R.; Ushkov, B. *Semiconducting chalcogenide glass III: Applications of chalcogenide glasses*; Elsevier, 2004; Vol. 80.

(109) Mehta, N. *Journal of Scientific and Industrial Research* **2006**, *65*, 777.

(110) Kim, H.; Ballikaya, S.; Chi, H.; Ahn, J.-P.; Ahn, K.; Uher, C.; Kaviany, M. *Acta Materialia* **2015**, *86*, 247.

(111) Al13ean 2011, p Schematic diagram of the high and low resistance states in a spin valve.

(112) Maeda, T.; Gong, W.; Wada, T. *Japanese Journal of Applied Physics* **2016**, *55*, 04ES15.

(113) Rodriguez carvajal, J. *Physica B* **1993**, *192*, 55.

(114) Sheldrick, G. M. *Acta Crystallographica Section A: Foundations of Crystallography* **2008**, *64*, 112.

(115) Gong, J.-Y.; Yu, S.-H.; Qian, H.-S.; Luo, L.-B.; Liu, X.-M. *Chemistry of materials* **2006**, *18*, 2012.

(116) Ibáñez, M.; Zamani, R.; LaLonde, A.; Cadavid, D.; Li, W.; Shavel, A.; Arbiol, J.; Morante, J. R.; Gorsse, S.; Snyder, G. J. *Journal of the American Chemical Society* **2012**, *134*, 4060.

(117) Kriegel, I.; Rodríguez-Fernández, J.; Wisnet, A.; Zhang, H.; Waurisch, C.; Eychmüller, A.; Dubavik, A.; Govorov, A. O.; Feldmann, J. *ACS nano* **2013**, *7*, 4367.

(118) Liu, H.; Shi, X.; Xu, F.; Zhang, L.; Zhang, W.; Chen, L.; Li, Q.; Uher, C.; Day, T.; Snyder, G. J. *Nature Materials* **2012**, *11*, 422.

(119) Miyatani, S.-y.; Miura, Y.; Ando, H. *Journal of the Physical Society of Japan* **1979**, *46*, 1825.

(120) Stanbery, B. J. *Critical reviews in solid state and materials sciences* **2002**, *27*, 73.

(121) Wu, C.; Yu, S.-H.; Chen, S.; Liu, G.; Liu, B. *Journal of Materials Chemistry* **2006**, *16*, 3326.

(122) Zhao, Y.; Burda, C. *Energy & Environmental Science* **2012**, *5*, 5564.

(123) Hong, A.; Li, L.; Zhu, H.; Zhou, X.; He, Q.; Liu, W.; Yan, Z.; Liu, J.-M.; Ren, Z. *Solid State Ionics* **2014**, *261*, 21.

(124) Zhao, Y.; Kumar, A.; Hin, C.; Priya, S. In *Nanoscale Thermoelectrics*; Springer: 2014, p 327.

(125) Alam, H.; Ramakrishna, S. *Nano Energy* **2013**, *2*, 190.

(126) Venkatasubramanian, R.; Siivola, E.; Colpitts, T.; O'quinn, B. *Nature* **2001**, *413*, 597.

(127) Chen, D.; Chen, G.; Jin, R.; Xu, H. *CrystEngComm* **2014**, *16*, 2810.

(128) Nethravathi, C.; Rajamathi, C. R.; Rajamathi, M.; Maki, R.; Mori, T.; Golberg, D.; Bando, Y. *Journal of Materials Chemistry A* **2014**, *2*, 985.

(129) Glazov, V.; Pashinkin, A.; Fedorov, V. *Inorganic materials* **2000**, *36*, 641.

(130) Zhou, G.-T.; Yao, Q.-Z.; Wang, X.; Jimmy, C. Y. *Materials chemistry and physics* **2006**, *98*, 267.

(131) Lesnyak, V.; George, C.; Genovese, A.; Prato, M.; Casu, A.; Ayyappan, S.; Scarpellini, A.; Manna, L. *ACS nano* **2014**, *8*, 8407.

(132) Baikulov, R.; Asadov, Y. G. *Inorganic materials* **2005**, *41*, 338.

(133) Chrissafis, K.; Vouroutzis, N.; Paraskevopoulos, K.; Frangis, N.; Manolikas, C. *Journal of alloys and compounds* **2004**, *385*, 169.

(134) Rivest, J. B.; Fong, L.-K.; Jain, P. K.; Toney, M. F.; Alivisatos, A. P. *The Journal of Physical Chemistry Letters* **2011**, *2*, 2402.

(135) Ishiwata, S.; Shiomi, Y.; Lee, J.; Bahramy, M.; Suzuki, T.; Uchida, M.; Arita, R.; Taguchi, Y.; Tokura, Y. *Nature materials* **2013**, *12*, 512.

(136) Ballikaya, S.; Chi, H.; Salvador, J. R.; Uher, C. *Journal of Materials Chemistry A* **2013**, *1*, 12478.

(137) Guin, S. N.; Pan, J.; Bhowmik, A.; Sanyal, D.; Waghmare, U. V.; Biswas, K. *Journal of the American Chemical Society* **2014**, *136*, 12712.

(138) Liu, Q.; Liu, H.; Liang, Y.; Xu, Z.; Yin, G. *Materials research bulletin* **2006**, *41*, 697.

(139) Basar, K.; Shimoyama, T.; Hosaka, D.; XiangLian; Sakuma, T.; Arai, M. *Journal of thermal analysis and calorimetry* **2005**, *81*, 507.

(140) Moroz, N.; Olvera, A.; Willis, G.; Poudeu, P. *Nanoscale* **2015**, *7*, 9452.

(141) Shimoyama, T.; Arai, M.; Sakuma, T. In *Superionic Conductor Physics* 2007; Vol. 1, p 27.

(142) Trots, D.; Skomorokhov, A.; Knapp, M.; Fuess, H. *The European Physical Journal B-Condensed Matter and Complex Systems* **2006**, *51*, 507.

(143) Chiang, M.-Y.; Chang, S.-H.; Chen, C.-Y.; Yuan, F.-W.; Tuan, H.-Y. *The Journal of Physical Chemistry C* **2011**, *115*, 1592.

(144) Pan, D.; An, L.; Sun, Z.; Hou, W.; Yang, Y.; Yang, Z.; Lu, Y. *Journal of the American Chemical Society* **2008**, *130*, 5620.

(145) Rinco, C. *Physical Review B* **1992**, *45*, 12716.

(146) Tuttle, J.; Albin, D.; Noufi, R. *Solar Cells* **1991**, *30*, 21.

(147) Wei, S.-H.; Ferreira, L. G.; Zunger, A. *Physical Review B* **1992**, *45*, 2533.

(148) Wei, S.-H.; Zhang, S.; Zunger, A. *Applied physics letters* **1998**, *72*, 3199.

(149) Bodnar, I.; Smirnova, G.; Smirnova, T.; Aleshchenko, Y. A.; Vodopyanov, L. *physica status solidi (b)* **1988**, *145*, 117.

(150) Suri, D.; Nagpal, K.; Chadha, G. *Journal of Applied Crystallography* **1989**, *22*, 578.

(151) Tsuji, I.; Kato, H.; Kobayashi, H.; Kudo, A. *The Journal of Physical Chemistry B* **2005**, *109*, 7323.

(152) Yamamoto, N. *Japanese Journal of Applied Physics* **1980**, *19*, 95.

(153) Honeyman, W. *Journal of Physics and Chemistry of Solids* **1969**, *30*, 1935.

(154) Bodnar', I. *Inorganic materials* **2002**, *38*, 647.

(155) Brik, M.; Piasecki, M.; Kityk, I. *Inorganic chemistry* **2014**, *53*, 2645.

(156) Harada, Y.; Nakanishi, H.; Chichibu, S. F. *Journal of applied physics* **2002**, *91*, 5909.

(157) Reshak, A. *Journal of Physics and Chemistry of Solids* **2015**, *78*, 46.

(158) Moreh, A.; Momoh, M.; Hamza, B. *International Journal of Engineering Science Invention* **2013**, *2*, 2319.

(159) Rodriguez-Carvajal, J. In *satellite meeting on powder diffraction of the XV congress of the IUCr*; Toulouse, France:[sn]: 1990; Vol. 127.

(160) Sootsman, J. R.; Chung, D. Y.; Kanatzidis, M. G. *Angew Chem Int Edit* **2009**, *48*, 8616.

(161) Jariwala, D.; Sangwan, V. K.; Lauhon, L. J.; Marks, T. J.; Hersam, M. C. *ACS nano* **2014**, *8*, 1102.

(162) Lv, R. T.; Robinson, J. A.; Schaak, R. E.; Sun, D.; Sun, Y. F.; Mallouk, T. E.; Terrones, M. *Accounts Chem Res* **2015**, *48*, 897.

(163) Gao, M. R.; Xu, Y. F.; Jiang, J.; Yu, S. H. *Chem Soc Rev* **2013**, *42*, 2986.

(164) Nakamura, K.; Kato, Y.; Akiyama, T.; Ito, T.; Freeman, A. J. *Phys Rev Lett* **2006**, *96*, 047206.

(165) Ranmohotti, K. G. S.; Djieutedjeu, H.; Lopez, J.; Page, A.; Haldolaarachchige, N.; Chi, H.; Sahoo, P.; Uher, C.; Young, D.; Poudeu, P. F. P. *J Am Chem Soc* **2015**, *137*, 691.

(166) Zhou, Z. H.; Chien, Y. J.; Uher, C. *Phys Rev B* **2006**, *74*, 224418.

(167) Zhou, Z. H.; Chien, Y. J.; Uher, C. *Appl Phys Lett* **2005**, *87*, 112503.

(168) Sanford, N.; Davies, R. W.; Lempicki, A.; Miniscalco, W. J.; Nettel, S. J. *Phys Rev Lett* **1983**, *50*, 1803.

(169) Goldstein, L.; Gibart, P.; Selmi, A. *J Appl Phys* **1978**, *49*, 1474.

(170) Moroz, N. A.; Olvera, A.; Willis, G. M.; Poudeu, P. F. P. *Nanoscale* **2015**, *7*, 9452.

(171) Wang, H. T.; Yuan, H. T.; Hong, S. S.; Li, Y. B.; Cui, Y. *Chem Soc Rev* **2015**, *44*, 2664.

(172) Djieutedjeu, H.; Makongo, J. P. A.; Rotaru, A.; Palasyuk, A.; Takas, N. J.; Zhou, X. Y.; Ranmohotti, K. G. S.; Spinu, L.; Uher, C.; Poudeu, P. F. P. *Eur J Inorg Chem* **2011**, 3969.

(173) Kuc, A. *Chemical Modelling* **2014**, *11*, 1.

(174) Poudeu, P. F. P.; Djieutedjeu, H.; Ranmohotti, K. G. S. *Abstr Pap Am Chem S* **2012**, *244*.

(175) Thilagam, A. *Physica B* **2015**, *464*, 44.

(176) Yoffe, A. D. *Solid State Ionics* **1990**, *39*, 1.

(177) Zhang, H. J.; Liu, C. X.; Qi, X. L.; Dai, X.; Fang, Z.; Zhang, S. C. *Nat Phys* **2009**, *5*, 438.

(178) Dietl, T. *Nat Mater* **2003**, *2*, 646.

(179) Tian, Y. F.; Li, Y. F.; He, M.; Putra, I. A.; Peng, H. Y.; Yao, B.; Cheong, S. A.; Wu, T. *Appl Phys Lett* **2011**, *98*, 162503.

(180) Chattopadhyay, A.; Das Sarma, S.; Millis, A. J. *Phys Rev Lett* **2001**, *87*, 227202.

(181) Quilty, J. W.; Shibata, A.; Son, J. Y.; Takubo, K.; Mizokawa, T.; Toyosaki, H.; Fukumura, T.; Kawasaki, M. *Phys Rev Lett* **2006**, *96*, 027202.

(182) Djieutedjeu, H.; Poudeu, P. F. P.; Takas, N. J.; Makongo, J. P. A.; Rotaru, A.; Ranmohotti, K. G. S.; Anglin, C. J.; Spinu, L.; Wiley, J. B. *Angew Chem Int Edit* **2010**, *49*, 9977.

(183) Djieutedjeu, H.; Olvera, A.; Page, A.; Uher, C.; Poudeu, P. F. P. *Inorg Chem* **2015**, *54*, 10371.

(184) Jin, H., Bartlomiej Wiendlocha, and Joseph P. Heremans *Energy & Environmental Science* **2015**, *8*, 2027.

(185) Shannon, R. *Acta Crystallographica Section A: Crystal Physics, Diffraction, Theoretical and General Crystallography* **1976**, *32*, 751.

(186) Song, Z.; Liu, H.; Du, Z.; Liu, X.; Cui, J. *physica status solidi (a)* **2016**, in Print.

(187) Djieutedjeu, H.; Olvera, A.; Page, A.; Uher, C.; Poudeu, P. F. *Inorganic chemistry* **2015**, *54*, 10371.

(188) Goldsmid, H. J.; Sharp, J. W. *Journal of electronic materials* **1999**, *28*, 869.

(189) McCabe, G.; Fries, T.; Liu, M.; Shapira, Y.; Ram-Mohan, L.; Kershaw, R.; Wold, A.; Fau, C.; Averous, M.; McNiff, E. *Physical Review B* **1997**, *56*, 6673.

(190) Aldakov, D.; Lefrançois, A.; Reiss, P. *Journal of Materials Chemistry C* **2013**, *1*, 3756.

(191) Suryanarayana, C. *Progress in materials science* **2001**, *46*, 1.

(192) Lai, C.-H.; Lu, M.-Y.; Chen, L.-J. *Journal of Materials Chemistry* **2012**, *22*, 19.

(193) Zimmermann, C.; Anson, C. E.; Weigend, F.; Clérac, R.; Dehnen, S. *Inorganic chemistry* **2005**, *44*, 5686.

(194) Bronger, W. *Pure and Applied Chemistry* **1985**, *57*, 1363.

(195) Gao, M.-R.; Xu, Y.-F.; Jiang, J.; Yu, S.-H. *Chemical Society Reviews* **2013**, *42*, 2986.

(196) Mitchell, K.; Ibers, J. A. *Chemical reviews* **2002**, *102*, 1929.

(197) Sturza, M.; Allred, J. M.; Malliakas, C. D.; Bugaris, D. E.; Han, F.; Chung, D. Y.; Kanatzidis, M. G. *Chemistry of Materials* **2015**, *27*, 3280.

(198) Kershaw, S. V.; Susha, A. S.; Rogach, A. L. *Chemical Society Reviews* **2013**, *42*, 3033.

(199) Lv, R.; Robinson, J. A.; Schaak, R. E.; Sun, D.; Sun, Y.; Mallouk, T. E.; Terrones, M. *Accounts of chemical research* **2014**, *48*, 56.

(200) Santra, P. K.; Kamat, P. V. *Journal of the American Chemical Society* **2013**, *135*, 877.

(201) Wang, H.; Yuan, H.; Hong, S. S.; Li, Y.; Cui, Y. *Chemical Society Reviews* **2015**, *44*, 2664.

(202) Böer, K. W. In *Handbook of the Physics of Thin-Film Solar Cells*; Springer: 2013, p 699.

(203) Feng, W.; Zheng, W.; Chen, X.; Liu, G.; Cao, W.; Hu, P. *Chemistry of Materials* **2015**, *27*, 983.

(204) Panthani, M. G.; Stolle, C. J.; Reid, D. K.; Rhee, D. J.; Harvey, T. B.; Akhavan, V. A.; Yu, Y.; Korgel, B. A. *The journal of physical chemistry letters* **2013**, *4*, 2030.

(205) Stolle, C. J., 2015.

(206) DUAN, H.; LI, Y.; ZHAO, K.; QIU, P.; SHI, X.; CHEN, L. *JOM* **2016**, *68*, 2659.

(207) Han, C.; Sun, Q.; Cheng, Z. X.; Wang, J. L.; Li, Z.; Lu, G. Q.; Dou, S. X. *Journal of the American Chemical Society* **2014**, *136*, 17626.

(208) Blasse, G. *Journal of Inorganic and Nuclear Chemistry* **1965**, *27*, 993.

(209) Glazer, A. *Acta Crystallographica Section B: Structural Crystallography and Crystal Chemistry* **1972**, *28*, 3384.

(210) Glazer, A. *Acta Crystallographica Section A: Crystal Physics, Diffraction, Theoretical and General Crystallography* **1975**, *31*, 756.

(211) Green, M. A.; Ho-Baillie, A.; Snaith, H. J. *Nature Photonics* **2014**, *8*, 506.

(212) Pena, M.; Fierro, J. *Chemical reviews* **2001**, *101*, 1981.

(213) Hancock, C.; Porras-Vazquez, J.; Keenan, P.; Slater, P. *Dalton Transactions* **2015**, *44*, 10559.

(214) Yan, B.; Jansen, M.; Felser, C. *Nature Physics* **2013**, *9*, 709.

(215) Rao, C. N. R.; Raveau, B. *Colossal magnetoresistance, charge ordering and related properties of manganese oxides*; World Scientific, 1998.

(216) Visser, D.; Ramirez, A.; Subramanian, M. *Physical review letters* **1997**, *78*, 3947.

(217) Pisoni, A.; Jaćimović, J. i.; Barisic, O. S.; Spina, M.; Gaál, R.; Forró, L.; Horváth, E. *The journal of physical chemistry letters* **2014**, *5*, 2488.

(218) Homes, C.; Vogt, T.; Shapiro, S.; Wakimoto, S.; Ramirez, A. *Science* **2001**, *293*, 673.

(219) Tamura, H.; Konoike, T.; Sakabe, Y.; Wakino, K. *Journal of the American Ceramic Society* **1984**, *67*.

(220) De Wolf, S.; Holovsky, J.; Moon, S.-J.; Löper, P.; Niesen, B.; Ledinsky, M.; Haug, F.-J.; Yum, J.-H.; Ballif, C. *The journal of physical chemistry letters* **2014**, *5*, 1035.

(221) Hao, F.; Stoumpos, C. C.; Cao, D. H.; Chang, R. P.; Kanatzidis, M. G. *Nature Photonics* **2014**, *8*, 489.

(222) Im, J.-H.; Lee, C.-R.; Lee, J.-W.; Park, S.-W.; Park, N.-G. *Nanoscale* **2011**, *3*, 4088.

(223) Lin, Q.; Armin, A.; Nagiri, R. C. R.; Burn, P. L.; Meredith, P. *Nature Photonics* **2015**, *9*, 106.

(224) Kikuchi, A.; Zhang, L.; Okinaka, N.; Tosho, T.; Akiyama, T. *Materials transactions* **2009**, *50*, 2675.

(225) Moon, J.-W.; Masuda, Y.; Seo, W.-S.; Koumoto, K. *Materials Science and Engineering: B* **2001**, *85*, 70.

(226) Watanabe, Y. *Applied physics letters* **1995**, *66*, 1770.

(227) Łupina, G.; Seifarth, O.; Kozłowski, G.; Dudek, P.; Dąbrowski, J.; Lippert, G.; Müssig, H.-J. *Microelectronic Engineering* **2009**, *86*, 1842.

(228) Kazarbina, T.; Maksimov, Y. M.; Serebrennikov, V. *Zhurnal Neorganicheskoj Khimii* **1981**, *26*, 1987.

(229) Lelieveld, R.; Ijdo, D. *Acta Crystallographica Section B: Structural Crystallography and Crystal Chemistry* **1980**, *36*, 2223.

(230) Bennett, J. W.; Grinberg, I.; Rappe, A. M. *Physical Review B* **2009**, *79*, 235115.

(231) Wang, Y.; Sato, N.; Fujino, T. *Journal of alloys and compounds* **2001**, *327*, 104.

(232) Sun, Y. Y., Agiorgousis, M. L., Zhang, P., & Zhang, S. *Nano letters* **2015**, *15*, 581.

(233) Meng, W.; Saparov, B.; Hong, F.; Wang, J.; Mitzi, D. B.; Yan, Y. *Chemistry of Materials* **2016**, *28*, 821.

(234) Tranchitella, L. J.; Chen, B.-H.; Fettinger, J. C.; Eichhorn, B. W. *Journal of Solid State Chemistry* **1997**, *130*, 20.

(235) Aslanov, L. A. *Russ. J. Inorg. Chem.* **1964**, *9*, 1090.

(236) Kubelka, P. *Z tech Phys* **1931**, *12*, 593.

(237) Goldschmidt, V. M. *Naturwissenschaften* **1926**, *14*, 477.

(238) Brese, N.; O'keeffe, M. *Acta Crystallographica Section B: Structural Science* **1991**, *47*, 192.

(239) Massalski, T. B.; Okamoto, H.; Subramanian, P.; Kacprzak, L. *ASM International, 1990* **1990**, 1485.

(240) Ali, R.; Yashima, M. *Journal of Solid State Chemistry* **2005**, *178*, 2867.

(241) PAYNE, W. H.; TENNERY, V. J. *Journal of the American Ceramic Society* **1965**, *48*, 413.

(242) Fleet, M. *Acta Crystallographica Section B: Structural Crystallography and Crystal Chemistry* **1981**, *37*, 917.

(243) Tachibana, M.; Kolodiazhnyi, T.; Takayama-Muromachi, E. *Applied Physics Letters* **2008**, *93*, 92902.

(244) Shockley, W.; Queisser, H. J. *Journal of applied physics* **1961**, *32*, 510.

(245) Kulkarni, S. A.; Sawadh, P.; Palei, P. K.; Kokate, K. K. *Ceramics International* **2014**, *40*, 1945.

(246) Vinod, T.; Jin, X.; Kim, J. *Materials Research Bulletin* **2011**, *46*, 340.

(247) Liu, Y.; Qin, D.; Wang, L.; Cao, Y. *Materials chemistry and physics* **2007**, *102*, 201.

(248) Durst, A. C.; Bhatt, R.; Wolff, P. *Physical Review B* **2002**, *65*, 235205.

(249) Prakash, J.; Tarasenko, M. S.; Mesbah, A.; Lebègue, S. b.; Malliakas, C. D.; Ibers, J. A. *Inorganic Chemistry* **2016**, *55*, 7734.